$K^{*0}(892)$ production in proton-nucleus collisions

Dissertation

zur Erlangung des Doktorgrades
des Fachbereichs Physik
der Universität Dortmund

vorgelegt von
Christopher van Eldik
aus Hagen

Hamburg
April 2004

Contents

Preface

In recent days, experiments at heavy-ion colliders have revived the interest in data from proton-nucleus (pA) collisions. It is widely believed that in a heavy-ion collision the hadronic environment is dense enough to form a quark-gluon plasma (QGP), a new state of matter, in which quarks and gluons interact as free particles. In order to study the properties of the QGP data from pA collisions are needed as a normalization to disentangle hadronic and nuclear effects from those of the nucleus-nucleus (AA) collision.

It is in the structure of Quantum Chromodynamics (QCD) itself that the attracting color-force between two single quarks becomes large at large distances (so-called confinement). As a consequence, free quarks cannot be observed directly, but only color-neutral hadrons, which are composite states consisting of two or three quarks. This fact considerably complicates the study of strong interactions, and many of the experimental observations are only insufficiently reproduced by phenomenological model calculations.

Since the 1960's many experiments analyzing e^+e^-, hadron-hadron, and hadron-lepton collisions contributed to the field of hadroproduction. Despite of the different initial states all results show a similar behavior. This observation finally led to a theoretical model which describes the collision by single parton-parton or lepton-parton interactions and the subsequent fragmentation of the products into hadrons. While in the limit of large momentum transfers the properties of the fundamental interactions can be calculated with perturbative methods (pQCD), the fragmentation is beyond precise calculations and is usually handled by phenomenological fragmentation models.

In proton-nucleus collisions nuclear effects introduce additional complications. On top of the basic nucleon-nucleon interaction, various initial and final state effects influence the cross sections and kinematic distributions of the observed particles. Therefore, measurements of particle spectra in pA collisions provide a valuable tool for tests of QCD and for the refinement of nuclear fragmentation models.

In a high-energetic nucleus-nucleus (AA) collision, finally, the energy density is expected to be large enough that for a short time the nuclei are not a collection of bound hadrons any more but a phase transition to a plasma of unbound quarks and gluons takes place (so-called deconfinement). One of the signatures of the existence of such a quark-gluon plasma is an enhanced production of particles

with strangeness content. Strange resonances are particularly suited to probe the properties of the plasma, since their yield compared to quasi-stable particles with the same quark content depends on the hadronization process. Due to their short life times these resonances are furthermore useful to study the phase transition from the QGP to a fully hadronized final state. With respect to pA collisions differences are expected in the kinematic distributions, the total cross sections, and in the shape and position of the resonance signals. In this context, data on strange resonance production in pA interactions can serve as a proper normalization of the experimental results on AA collisions.

This analysis covers the production of the strange vector mesons $K^{*0}(892)$ and $\bar{K}^{*0}(892)$ in inelastic pA collisions at $\sqrt{s} = 41.6\,\text{GeV}$ and mid-rapidity. The data have been taken with the HERA-B detector at DESY (Hamburg), which is equipped with a variety of nuclear targets and is therefore suited for measurements of atomic number dependencies.

About $130 \cdot 10^6$ inelastic events recorded end of 2002 on Carbon, Titanium, and Tungsten targets were analyzed. The single-differential cross sections in transverse momentum squared and rapidity, $d\sigma/dp_T^2$ and $d\sigma/dy$, have been measured as well as the total production cross sections. The results are compared to measurements of previous pp and pA collision experiments. Furthermore, the atomic number dependence of the cross sections is studied as a function of the kinematics.

The thesis is subdivided as follows:

- Chapter 1 summarizes the basic properties of vector mesons, gives an overview about the experimental achievements in the field of K^{*0} production, and introduces the kinematic quantities measured.
- Chapter 2 addresses the theoretical framework of particle production in pp, pA, and AA collisions. Special emphasis is given to strange resonances as a probe of the dynamical properties of the QGP.
- The third chapter describes the setup of the HERA-B detector and the data reconstruction chain, followed by a short overview of the current HERA-B physics program.
- The data set is introduced in chapter 4, and the selection cuts to obtain clear $K^{*0}/\bar{K}^{*0}$ signals are documented. The properties of the Monte-Carlo simulation are verified, before the invariant mass fit to extract the signal yields is described.
- Chapter 5 is attributed to the evaluation of the uncorrected differential distributions in p_T^2 and rapidity, followed by the calculation of the corresponding acceptances.
- The differential and total production cross sections and their atomic number dependencies are given in chapter 6, including comparisons of the results with previous measurements.
- Finally, chapter 7 summarizes the findings of the analysis.

Chapter 1

Overview of K^* production

This introductory overview first reviews the basic properties of vector meson resonances before it motivates the goals of this analysis in the context of previous measurements of K^* production. The experimental achievements in this field are summarized focusing on measurements of total cross sections and of differential distributions as a function of the kinematics. Finally, common parameterizations to describe the differential cross section measurements are discussed.

1.1 Properties of light vector mesons

In 1964 Gell-Mann and Zweig realized [gel64, zwe64] that the up-to-then known hadrons can be described and structured based on SU(3) flavor symmetry. In this interpretation hadrons are color-less composites of quarks, either quark-antiquark states (mesons, $q\bar{q}'$), or three-quark states (baryons, $qq'q''$ or $\bar{q}\bar{q}'\bar{q}''$)[1]. Four years later deep inelastic lepton-proton scattering found first experimental evidence that indeed protons reveal a substructure [pan68]. The so-called partons, point-like constituents of the proton (in general, of hadrons), were later identified with quarks and gluons.

Mesons can be classified by their quark content $q\bar{q}'$ and their total angular momentum $J = L + S$, $L \in \{0, 1, 2 \dots\}$ being the orbital angular momentum of the $q\bar{q}'$ state, and $S \in \{0, 1\}$ its spin. Another important property is the parity $P = (-1)^{L+1}$ of the wave function of the $q\bar{q}'$ state. The $L = 0$ mesons are subdivided into pseudo-scalar mesons ($J^P = 0^-$) and vector mesons ($J^P = 1^-$). The K^* resonances belong to the class of vector mesons and can be interpreted as being excited states of their corresponding pseudo-scalar mesons.

For both the light pseudo-scalar and vector mesons the nine possible $q\bar{q}'$ combinations of the light u, d, and s quarks group themselves into a nonett, as shown in fig. 1.1. The states are classified by their strangeness content S and the third component of their isospin, I_3. Since the strong force is flavor-blind, all states

[1] today we know from QCD that in principle even more complicated color-neutral combinations of quarks are allowed. Indeed, first evidence of five-quark states ($qqq\bar{q}q$, so-called pentaquarks) have been reported recently (see [knö04] and references therein).

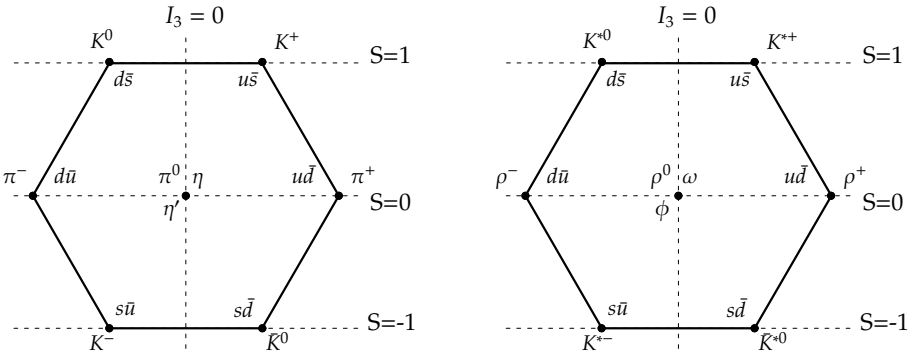

Figure 1.1: $SU(3)_{\text{flavor}}$ multiplets of the light pseudoscalar mesons (left) and the light vector mesons (right). The various states are classified by their strangeness content S and the third component I_3 of their isospin.

are degenerated in case of perfect SU(3) symmetry. However, mass differences between the quarks and the different electric charges break the symmetry, which then results in nine observable particles with different properties and masses. The three mass-eigenstates in the center of the nonett are mixtures of $u\bar{u}$, $d\bar{d}$, and $s\bar{s}$. In case of the vector mesons the mixing is such that the ϕ is an almost pure $s\bar{s}$ state with only a very small admixture of $u\bar{u}$ and $d\bar{d}$, while the ρ^0 and η are mixtures of the $u\bar{u}$ and $d\bar{d}$ states (see table 1.1).

The family of the K^* mesons is characterized by the non-vanishing strangeness

resonance	mass [MeV]	width [MeV]	quark content
$K^{*0}(892)$	896.10 ± 0.28	50.5 ± 0.6	$\|d\bar{s}\rangle$
$K^{*+}(892)$	891.66 ± 0.26	50.8 ± 0.9	$\|u\bar{s}\rangle$
$\rho^-(770)$	768.3 ± 0.5	151.5 ± 1.2	$\|d\bar{u}\rangle$
$\rho^0(770)$	768.7 ± 0.7	152.4 ± 1.5	$1/\sqrt{2} \cdot (\|u\bar{u}\rangle - \left\|d\bar{d}\right\rangle)$
$\rho^+(770)$	768.3 ± 0.5	151.5 ± 1.2	$\left\|u\bar{d}\right\rangle$
$K^{*-}(892)$	891.66 ± 0.26	50.8 ± 0.9	$\|s\bar{u}\rangle$
$\bar{K}^{*0}(892)$	896.10 ± 0.28	50.5 ± 0.6	$\left\|s\bar{d}\right\rangle$
$\omega(783)$	781.94 ± 0.12	8.41 ± 0.09	$1/\sqrt{2} \cdot (\|u\bar{u}\rangle + \left\|d\bar{d}\right\rangle)$
$\phi(1020)$	1019.413 ± 0.008	4.43 ± 0.05	$\|s\bar{s}\rangle$

Table 1.1: Masses, full resonance widths, and quark content of the light vector mesons [hag02].

content of their members ($S = \pm 1$). The resonance masses of the K^{*0} and $K^{*\pm}$ have been measured as being 896.10 ± 0.28 MeV and 891.66 ± 0.26 MeV, respectively[2] [hag02]. All K^* decay dominantly into $K\pi$, $BR(K^* \to K\pi) \approx 100\,\%$. Taking isospin conservation into account, the branching ratio for the decay channels used in this analysis, $K^{*0} \to K^+\pi^-$ and $\bar{K}^{*0} \to K^-\pi^+$, is $2/3$ in both cases. From measurements

[2] note, that throughout this thesis, we set $c = 1$ for simplicity.

[hag02] one obtains $BR(K^{*0} \rightarrow K^+\pi^-) = 0.6660 \pm 0.0006$.

Like all other light vector mesons the K^* has a very short life time due to its dominantly strong decay. With the resonance width being about 50 MeV the mean life time is $\tau \approx 1.3 \cdot 10^{-23}$ s or, correspondingly, $c\tau \approx 3.9$ fm. This makes it an interesting probe for the existence of the quark-gluon plasma (cf. section 2.3.2).

1.2 Historical overview and motivation

Until the early 1970's hadroproduction experiments in high-energy physics concentrated mainly on the measurement of "stable" hadrons, i.e. pions, kaons, and protons. Virtually nothing was known about the inclusive production of vector (or tensor) mesons and excited baryon states. When it was realized [win75] that a substantial amount of the observed stable particles is not directly produced in the primary collision but comes from higher resonance decays, the interest in resonance production grew considerably.

Studies of K^* production have been done mainly in bubble-chamber experiments with kaon [gra78, göt82] or proton beams [blo74, kic79, agu91] of beam momenta between 12 and 400 GeV (i.e. center-of-mass energies of $\sqrt{s} = 4.9 - 27.4$ GeV). Collision energies of up to $\sqrt{s} = 62$ GeV were reached in pp interactions at the ISR [jan77, bre89]. Only two measurements of K^{*0} production on light nuclear targets [faw90, bel93] exist, where 200 GeV K^-/π^- and 300 GeV π^- beams have been brought to collision with silicon and beryllium, respectively. No measurements have been found in the literature on proton-nucleus collisions.

All experiments on K^* production have focused on measurements of the total production cross section or on longitudinal and transverse single-differential cross sections. To estimate the amount of quasi-stable particles coming from decays of resonances, the production ratio of vector mesons to pseudoscalar mesons has been investigated, too.

Among many others these measurements significantly increased our knowledge on the underlying mechanisms of hadroproduction. However, there is still no model which describes all data consistently. This is especially true for pA collisions, where in-medium effects further complicate the picture. Therefore, data on pA collisions are still needed, not only in view of the physics programs at heavy-ion colliders.

This analysis contributes to the field of resonance production in pA interactions at $\sqrt{s} = 41.6$ GeV, using C, Ti, and W targets. The focus is on the strange vector mesons K^{*0} and $\bar{K}^{*0}$which are expected to be a good probe of deconfinement in AA collisions. We will measure total and differential cross sections as a function of p_T^2 and rapidity and study their dependence on the atomic number of the target material.

1.3 Present experimental achievements

Within this section we give a brief summary of the experimental results obtained so far on K^* production in proton-proton and hadron-nucleus collisions. First, we define the basic kinematic quantities used. Afterwards, we present previous measurements of total cross sections and of differential distributions and introduce commonly used parameterizations to describe them. Although this analysis concentrates on the production of neutral K^*, we have also included data of K^{*+} and K^{*-} production providing measurements at small collision energies. Since the strong force is flavor-blind, we expect the results on charged and neutral K^* production to be comparable.

1.3.1 Kinematic variables

Many of the experiments quoted here have measured differential production cross sections to study the phase-space dependence of the production mechanism. There are a number of kinematic variables that are commonly used to parameterize the phase space. As we will make frequent use of them, we introduce them briefly by deriving the common formula for the invariant cross section $E\,d^3\sigma/dp^3$.

In collision and fixed target experiments the direction of the incoming beam does always define a preferred axis. Especially Lorentz transformations between the lab frame and the center-of-mass system are done with respect to this axis, leaving transverse components of physical quantities invariant under the transformation. To calculate cross sections it is therefore advantageous to split the Lorentz invariant phase space element, $d^3p/2E$, into transverse and longitudinal components:

$$\frac{d^3p}{2E} = \frac{dp_x\,dp_y\,dp_z}{2E} = \frac{d\phi\;p_T\,dp_T\,dp_z}{2E}, \tag{1.1}$$

E and p being the energy and three-momentum vector of the produced particle (in the center-of-mass frame), p_z its component along the beam axis, ϕ the azimuthal angle, and $p_T = \sqrt{p_x^2 + p_y^2}$ the transverse momentum. While p_T is a transverse quantity and therefore is Lorentz invariant with respect to a boost along the beam direction, p_z is not. If we express p_z by the so-called rapidity y,

$$y = \frac{1}{2}\ln\frac{E + p_z}{E - p_z}, \tag{1.2}$$

a transformation between two Lorentz frames along z is reduced to a constant shift in y. In case of HERA-B, $y_{lab} = y^* + 3.79$, where y^* denotes the rapidity in the proton-nucleon center of mass system.

By using $dy/dp_z = 1/E$, (1.1) becomes

$$\frac{d^3p}{2E} = \frac{1}{4}\,d\phi\,dp_T^2\,dy, \tag{1.3}$$

where we have further used $dp_T^2 = 2\,p_T\,dp_T$.

The invariant cross section $E\frac{d^3\sigma}{dp^3}$ can now be expressed in terms of transverse momentum and rapidity by using (1.3):

$$E\frac{d^3\sigma}{dp^3} = \frac{2\,d^3\sigma}{d\phi\,dp_T^2\,dy} = \frac{1}{\pi}\cdot\frac{d^2\sigma}{dy\,dp_T^2}. \tag{1.4}$$

In the last step we have integrated over the azimuthal angle ϕ.

Differential cross sections are usually measured in bins of p_T^2 or y as

$$\frac{d\sigma}{dp_T^2} \text{ and } \frac{d\sigma}{dy}, \tag{1.5}$$

respectively, implicitly assuming a factorization of (1.4) in p_T^2 and y (see e.g. [dri81]). In our analysis we will follow this approach, too. In this context it is common use to call the parts of the phase space described by y and p_T^2 the longitudinal and transverse phase space, respectively.

Some experiments replace y by Feynman-x,

$$x_F = \frac{p_z^{cms}}{p_{z,max}^{cms}} \approx \frac{2\,p_z^{cms}}{\sqrt{s}}, \tag{1.6}$$

where p_z^{cms} is the longitudinal momentum of the particle in the center-of-mass system, and $p_{z,max}^{cms}$ is the kinematic limit of p_z^{cms}. Quoting x_F is especially useful and theoretically justified for measurements in the very forward ($x_F \to 1$) or backward ($x_F \to -1$) part of the phase space. Since our data are produced in the central part of the phase space we have decided to use rapidity throughout this analysis.

We will now present some results of previous measurements of total and differential cross sections. For the transverse differential distributions we will discuss commonly used parameterizations, which we will later apply to our own results.

1.3.2 Total cross sections

Fig. 1.2 shows a compilation of cross sections for inclusive K^* production in pp collisions as a function of the center-of-mass energy $\sqrt{s}$ [blo74, boc79, kic79, bri82, azi86, bog88, agu91]. Data exist in an energy range of $7.5\,\text{GeV} \le \sqrt{s} \le 53\,\text{GeV}$. The measurements up to $\sqrt{s} = 26\,\text{GeV}$ focus on the charged K^* only, while total cross sections of neutral K^* production are available for $\sqrt{s} = 27.5\,\text{GeV}$ and $\sqrt{s} = 52.5\,\text{GeV}$. All cross sections are summarized in table 1.2.

A general observation is that all cross sections rise with $\sqrt{s}$ and seem to saturate at higher energies. Comparing the different numbers one notices that particles with strangeness $S = 1$ (K^{*+}, K^{*0}) are more frequently produced than those with strangeness $S = -1$ (K^{*-}, $\bar{K}^{*0}$). Towards higher $\sqrt{s}$, this difference tends to decrease.

This analysis will provide measurements of the total K^{*0} and $\bar{K}^{*0}$ production cross

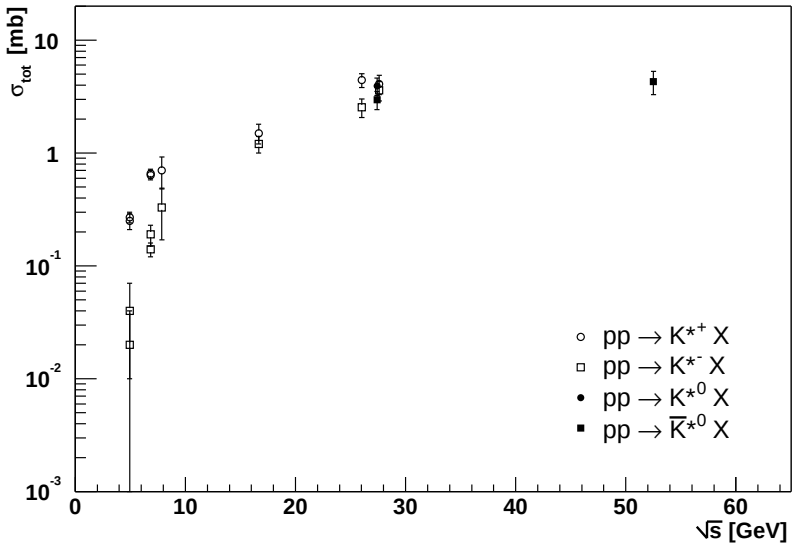

Figure 1.2: Measurements of the total K^* production cross sections in pp-collisions as a function of the center-of-mass energy $\sqrt{s}$ [blo74, boc79, kic79, dri81, bri82, azi86, bog88, agu91]. The numbers are summarized in table 1.2.

particle	$\sqrt{s}$ [GeV]	σ_{tot} [mb]	reference
K^{*+}	4.9	0.25 ± 0.04	[blo74]
	4.9	0.27 ± 0.03	[boc79]
	6.9	0.64 ± 0.06	[blo74]
	6.9	0.66 ± 0.06	[boc79]
	7.9	0.70 ± 0.22	[bog88]
	16.7	1.5 ± 0.3	[bri82]
	26.0	4.42 ± 0.62	[azi86]
	27.6	4.1 ± 0.8	[kic79]
K^{*-}	4.9	0.02 ± 0.02	[blo74]
	4.9	0.04 ± 0.03	[boc79]
	6.9	0.14 ± 0.02	[blo74]
	6.9	0.19 ± 0.04	[boc79]
	7.9	0.33 ± 0.16	[bog88]
	16.7	1.2 ± 0.2	[bri82]
	26.0	2.54 ± 0.47	[azi86]
	27.6	3.6 ± 0.7	[kic79]
K^{*0}	27.4	3.92 ± 0.68	[agu91]
$\bar{K}^{*0}$	27.4	2.96 ± 0.54	[agu91]
	52.5	4.3 ± 1.0	[dri81]

Table 1.2: Previous measurements of the K^* production cross sections in pp collisions. For fixed target experiments $\sqrt{s}$ has been calculated from the beam energy.

sections in pp collisions. The cross sections are determined by extrapolating the values obtained in pC, pTi, and pW collisions to $A = 1$. Since the measurement is performed at $\sqrt{s} = 41.6\,\text{GeV}$ it will fill the large gap in energy between the measurements at $\sqrt{s} = 27.4\,\text{GeV}$ and $\sqrt{s} = 52.5\,\text{GeV}$ (see fig. 1.2).

1.3.3 Differential distributions

Transverse distributions. p_T^2 distributions of K^{*0} production have been measured using kaon, pion, and proton beams [blo74, kic79, göt82, faw90, agu91, bel93]. While most of the measurements are limited to a low p_T range ($p_T \leq 1\,\text{GeV}$) [faw90] and [bel93] cover transverse momenta up to 2.2 GeV and 3.6 GeV, respectively. Both experiments used light nuclear targets, [faw90] scattering 200 GeV π^- and K^- beams on silicon, and [bel93] colliding 300 GeV pions on a beryllium target. The results of the measurements are shown in fig. 1.3.

There are two commonly used parameterizations for $d\sigma/dp_T^2$. In the lower p_T range

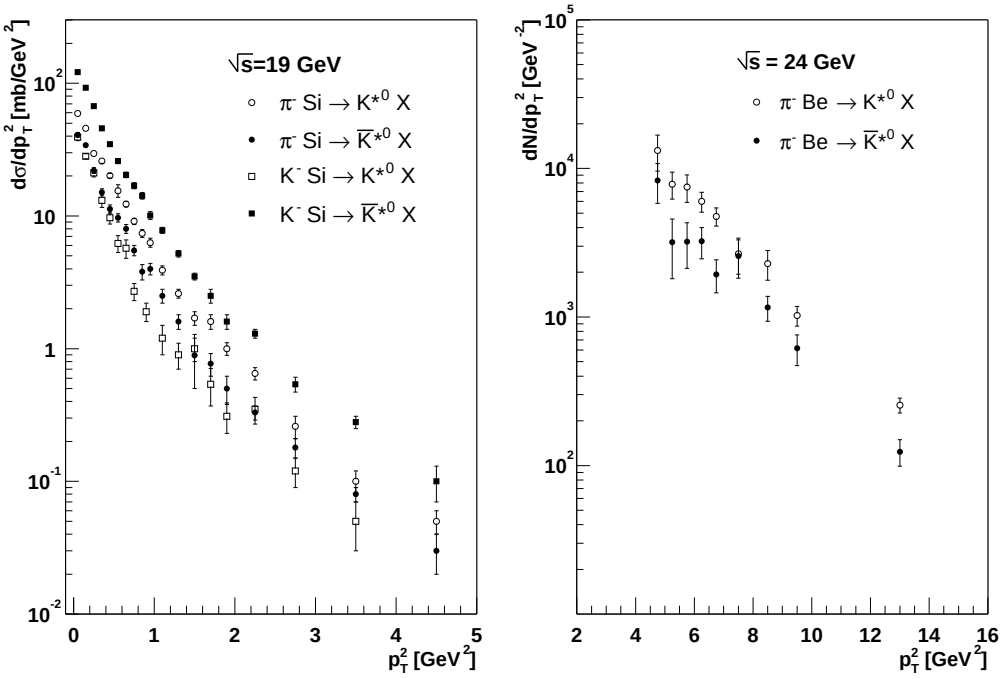

Figure 1.3: Transverse differential distributions for K^{*0} and $\bar{K}^{*0}$ production on light nuclear targets. *Left:* Results of [faw90] for 200 GeV π^- and K^- beams interacting with a fixed silicon target. The acceptance of the measurement covers the full longitudinal phase space. *Right:* Measurements from [bel93] for a 300 GeV π^- beam incident on a beryllium target. The measurement was done at mid-rapidity. Note that this latter result does not include an absolute normalization.

(up to about 1 GeV) the distributions follow an exponential form:

$$\frac{d\sigma}{dp_T^2} = B\, e^{-bp_T^2}, \tag{1.7}$$

where B is a normalization parameter and $-b$ the slope of the distribution. At higher p_T^2, however, the distributions get significantly harder, which is described phenomenologically by a polynomial ansatz:

$$\frac{d\sigma}{dp_T^2} = C\left[1 + \left(\frac{p_T^2}{p_0^2}\right)^{-\beta}\right]. \tag{1.8}$$

Here C is a normalization constant, and p_0 and β describe the shape of the distribution. In chapter 2 we will argue that this behavior is due to hard scattering of single partons, and that a power-law behavior is indeed expected.

Different measurements can be compared by fitting the distributions to (1.7) or (1.8). Instead of comparing the shape parameters directly it is common practice to calculate the mean p_T of the parameterizations. For (1.7) and (1.8) one gets

$$\langle p_T \rangle = \sqrt{\pi/4b} \text{ and } \langle p_T \rangle = \sqrt{\pi p_0^2}\,\frac{\beta - 1}{2}\,\frac{\Gamma(\beta - \frac{3}{2})}{\Gamma(\beta)}, \tag{1.9}$$

respectively.

In chapter 6 we will compare the results of our measurement to the results of [faw90] using the parameterizations described here.

Differential distributions in rapidity. Most of the bubble chamber experiments studied K^* production in forward direction ($y^* > 0$). The longitudinal phase space distribution of the produced resonances has been found to depend strongly on whether the resonance has a valence quark in common with the projectile particle [faw90]. If this is the case, the cross section is enhanced in the forward direction. For the central region ($y^* \approx 0$) an approximate plateau in rapidity is predicted [krz78], which follows from arguments of Lorentz invariance (see section 2.1.4):

$$\frac{d\sigma}{dy}(y^* \approx 0) \approx \text{const.} \tag{1.10}$$

This has indeed been observed for the production of various particles, including K^{*0} production in pp collisions [blo74, agu91].

This analysis will provide differential cross section measurements of K^{*0} production at mid-rapidity, $-1.2 \leq y^* \leq 0.7$. Therefore, we will be able to test this simple prediction also for pA collisions, where up to now no data existed.

Chapter 2

Particle production in pA and AA collisions

To explain the atomic mass number dependence of the production cross section in pA interactions a closer look onto the mechanisms of the scattering process is needed. Therefore, we present the most important phenomenological and theoretical concepts behind pA and AA interactions. The underlying proton-nucleon scattering is considered first, followed by a discussion of the necessary modifications in the presence of nuclear matter. At the end we will introduce the physics of nucleus-nucleus collisions and the formation of quark-gluon plasma.

2.1 Proton-proton interactions

To apprehend the properties of pA collisions a theoretical understanding of pp interactions is a prerequisite. In this section we will therefore explain the important theoretical ingredients of proton-proton collisions[1]. Many models describing the bulk of soft hadronic interactions exist. They are mostly based on thermodynamical ansatzes (see e.g. [hag65]). In this chapter we will restrict ourselves mostly on hard interactions. In doing so we will basically follow the arguments given in [gei90].

Although the quark model shed light upon the complicated findings in hadron spectroscopy, it was not applied to hadron dynamics until Bjorken and Paschos [bjo69] identified quarks with the point-like partons observed in deep-inelastic electron-proton scattering [pan68, bjo69$^+$]. First calculations [ber71] of inclusive hadroproduction within an extended parton model predicted particle jets of high transverse momenta, arising from single hard parton-parton scatterings. The cross section for $p_T \gg 1\,\mathrm{GeV}$ was predicted to follow a power-law in transverse

[1] we will restrict ourselves to pp collisions in the following, since our main focus is in pA interactions. However, most of the arguments made here are valid for other types of hadronic collisions, too.

momentum,

$$E\frac{d^3\sigma}{dp^3} \propto \frac{1}{p_T^4}, \tag{2.1}$$

i.e. a significant excess of hadrons with high-p_T was expected with respect to the exponential fall-off measured at low p_T. This was indeed observed in pp collisions at the ISR in 1973 [alp73, ban73, büs73]. However, it became clear that the picture of pp interactions was by far not complete, since the measured cross sections follow roughly a p_T^{-8} behavior.

Among others these measurements led to many theoretical speculations in this field, resulting in the so-called quark-parton model, which proved to describe the experimental observations on pp collisions quite consistently. It identifies the charged point-like constituents of the hadron with quarks. In this framework, an inelastic collision between two protons can be subdivided into four consecutive steps, which are well separated in time:

1. Initial state radiation before the scattering.
2. Hard scattering between at least two partons.
3. Parton evolution after the hard scattering.
4. Fragmentation of the free partons into hadrons and the decay of hadron resonances into stable particles.

Each process has a different impact on the kinematics of the final state particles, as will be discussed within the next sections. Only if all contributions are correctly taken into account a reasonable prediction of the measured kinematic distributions is possible. In the following we will briefly explain the physical meaning of each process.

2.1.1 Proton structure and initial state effects

Within the last decades deep-inelastic lepton-nucleon scattering provided deep insight into the structure of the nucleon. Not only the point-like structure of the partons has been tested but also the distributions of their momentum fractions x with respect to the nucleon's momentum have been measured. The probability to scatter a parton q of momentum fraction x inside the nucleon is given by the parton density distributions $q(x, Q^2)$, where Q^2 is the momentum transfer squared between the projectile and the scattered parton. Surprisingly, the measurements show that only about 50 % of the nucleon's momentum is carried by valence and sea quarks, while the remaining momentum is made up by gluons.

The parton distributions are an important input to the cross-section calculation of pp collisions, since the momentum fractions x_1 and x_2 of both colliding partons are not a priori known and cannot be determined from the final state of the interaction. They do, however, only reflect the momentum fractions of partons with respect to the proton's direction (i.e. only longitudinal momenta). To describe the p_T^2 distributions of final state hadrons correctly, the parton distributions have

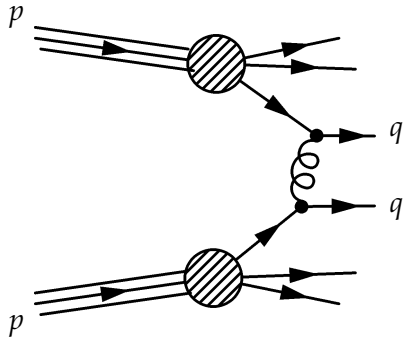

Figure 2.1: Example of a proton-proton collision on parton level. In the center two valence quarks undergo hard scattering. The other quarks are spectators only.

to be extended for transverse parton momenta k_T. These arise from two different effects:

- Internal transverse motion of the partons inside the proton. Considering the radius of the proton a mean transverse momentum of about 250-300 MeV is expected from the uncertainty principle. This part of the transverse momentum is independent of the kinematics.
- Gluon radiation directly before the hard scattering. This effect is a characteristics of QCD and depends on Q^2, as with larger Q^2 more gluons are radiated.

In model calculations both effects are usually parameterized by a common function exponentially decreasing with k_T or k_T^2, where $\langle k_T \rangle \approx 0.6 - 0.8\,\mathrm{GeV}$. The magnitude of this so-called k_T-broadening has been shown to have a strong impact on the p_T distributions of final state hadrons for $p_T \leq 4\,\mathrm{GeV}$ [gei90].

2.1.2 Hard parton scattering

The actual hard scattering takes place between two partons of the colliding proton-proton system (see fig. 2.1). Both partons acquire high transverse momenta, while the proton remnants (so-called spectators) leave the interaction region

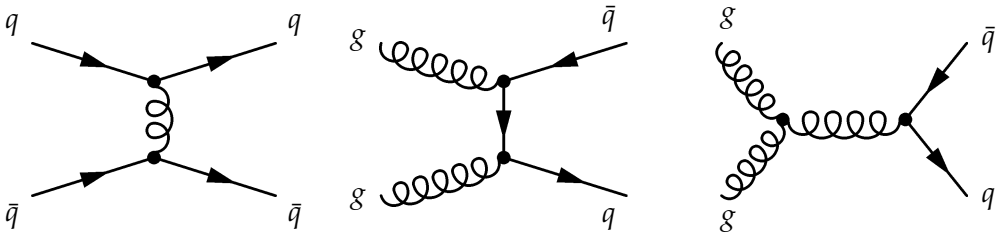

Figure 2.2: Examples of leading order Feynman diagrams for parton-parton scattering. *Left side:* quark-quark scattering. *Middle and right side:* two different contributions to gluon-gluon fusion.

basically collinear to the direction of the incoming beam.

Fig. 2.2 shows examples of leading order Feynman diagrams for quark-quark scattering and gluon-gluon fusion. If Q^2 is large enough, $Q^2 \gg 1\,\mathrm{GeV}^2$, the scattering process can be calculated within the framework of perturbative QCD. Much like in the early calculations within the framework of the parton model

a power-law behavior p_T^{-n} is expected for the transverse particle distributions. However, the prediction is not $n = 4$ any more, but the Q^2-dependence of both the strong coupling constant α_s and the parton density distributions $q(x, Q^2)$ induce larger values for n. The largest effect on the final state p_T distributions is, however, expected from parton evolution after the scattering took place. This is addressed in the following.

2.1.3 Parton evolution

After the hard interaction the scattered partons (and the spectators) cool down by emitting gluons or producing quark-antiquark pairs. These branching processes are shown in fig. 2.3. As long as α_s is small enough they can be described using the so-called splitting functions [alt77] calculable in pQCD. Hard processes of this kind are particularly important, because they influence the kinematics of the scattered partons quite drastically and thus give large corrections to the overall topology of the event.

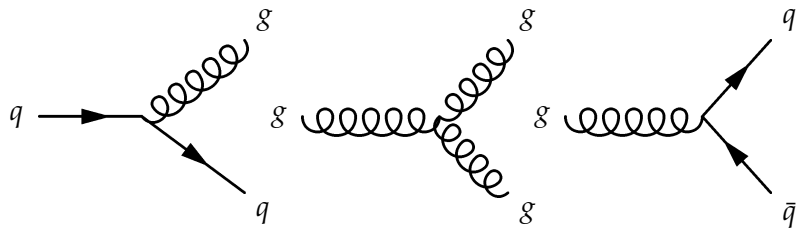

Figure 2.3: Different processes in parton evolution. From left to right: $q \to qg$, $g \to gg$, $g \to q\bar{q}$.

2.1.4 Hadronization

In the preceding section the evolution of the outgoing partons from a scale characteristic of the hard scattering to a soft scale was considered. As the system cools down α_s becomes large, and phenomenological models have to be applied to describe the transition of free partons into (quasi-)stable hadrons and hadron resonances. They provide the necessary link between the present level of perturbative QCD calculations and experimental data. One of the most successful ones is the string fragmentation model [art74], which is used in many modern event simulation tools. Implemented in the package JETSET [sjö94] it is also part of the HERA-B event simulation FRITIOF [pi92]. In our analysis we use this package to simulate the formation of K^{*0} resonances in pA collisions.

The string model describes the QCD color field between two quarks q and $\bar{q}$ as a relativistic elastic rubber without transverse dimensions, its energy density being about 1 GeV/fm [cel78]. When the quarks move away from each other the potential energy stored in the string increases constantly until it is large enough to create a $q'\bar{q}'$ pair from the vacuum. In the model calculations the $qq'\bar{q}\bar{q}'$ system is split into two colorless states, $q\bar{q}'$ and $q'\bar{q}$, and usually one of them is in turn

allowed to create a new $q\bar{q}$ pair as soon as the energy stored in its color field exceeds the production threshold. The other one is kept as a bound meson[2]. In this way a parton cascade is generated in which hadrons are built until all energy is consumed. Topologically, the cascade is aligned with the original partons and spectators from the hard scattering, so that narrow jets of hadrons are seen in the final state. The special properties of these jets explain some well-known observations in the final state, in particular the development of a plateau at mid-rapidity [krz78].

The $q\bar{q}$ creation out of the vacuum is not equally probable for the different quarks but depends on the quark mass. For the three light quarks,

$$u : d : s = 1 : 1 : \lambda, \tag{2.2}$$

with $\lambda = 0.3$ being the so-called strangeness suppression factor, which is in most models an empirical constant, but can be extracted from calculations explicitely considering the differences in the quark masses. The probability to create a $c\bar{c}$ pair is suppressed by about 10^{-11}, hence heavy quarks do not take part in the fragmentation process.

From spin statistics the fraction of directly produced vector mesons V among all fragmented mesons is expected to be

$$\frac{V}{V+P} = 0.75, \tag{2.3}$$

where P is the number of directly produced pseudo-scalar mesons. So only about 25 % of the observed stable particles are directly produced in the fragmentation process, while a large fraction originates from decays of vector (or tensor) mesons.

2.1.5 Experimental observables

The model described above is able to predict most experimental observations in pp collisions reasonably. With respect to the final state the model explains

- the properties of particle production in the longitudinal phase space, which has been shown to depend on the parton's momentum fraction x with respect to the colliding protons. Furthermore, fragmentation models predict an approximate plateau in $d\sigma/dy$ at mid-rapidity.
- In the transverse phase space the hard parton scattering leads to a power-law dependence of $d\sigma/dp_T^2$. The shape of the spectrum is strongly influenced by the primordial transverse momentum of the partons in the colliding protons and on parton evolution in the initial and final state of the scattering process.
- Details on the production ratio between resonances and stable particles follow from spin statistics arguments. Furthermore, the relative abundances

[2] the creation of baryons in the hadronization needs a slightly different mechanism, which we will not explain here.

of hadrons with different quark content can be understood when the quark masses are taken into account in calculating the scattering and fragmentation process.

In the following section we will address pA collisions and explain in which way nuclear effects additionally influence the particle production in the transverse and longitudinal phase space.

2.2 Nuclear modifications in pA collisions

pp interactions have been extensively studied in the past, and the theoretical and phenomenological models presented in the last section have been tuned in order to describe the data consistently. When it comes to proton-nucleus collisions the experimental observations are even more complicated to understand. In this section we will introduce the most important aspects of the phenomenology of pA collisions, concentrating on the so-called Glauber model.

2.2.1 The Glauber model

One of the basic predictions of pA collision models is the dependence of the production cross section σ_X^{pA} of a certain particle X on the atomic number of the target material. Phenomenologically, a common parameterization is used to relate σ_X^{pA} to the underlying proton-nucleon cross sections σ_X^{pN}:

$$\sigma_X^{pA} = \sigma_X^{pN} \cdot A^{\alpha_X}, \tag{2.4}$$

where A is the atomic mass number.

Most approaches [cap91] to understand particle production in pA collisions are formulated in the framework of the Glauber model. The main ingredients are the following:

- The target nucleus geometry is introduced by a simple profile function:

$$T_A(b) = \int dz\, \rho(b, z). \tag{2.5}$$

  Here, $\rho(b, z)$ is the nuclear density, b the impact parameter, and z the coordinate along the projectile's direction (see fig. 2.4). The nuclear density is for heavy nuclei ($A > 16$) well described by a Wood-Saxon potential. For smaller atomic mass numbers shell corrections have to be applied [pi92].

- A proton-nucleus interaction is considered as a series of binary sub-collisions between the proton and the individual target nucleons. The proton is assumed to traverse the nucleus in a straight line, and only the nucleons along the proton's path can possibly take part in the interaction (see fig. 2.4). All sub-collisions are assumed to be incoherent. Thus, the production cross section does only depend on the underlying proton-nucleon cross section and the path length of the proton in the nuclear medium.

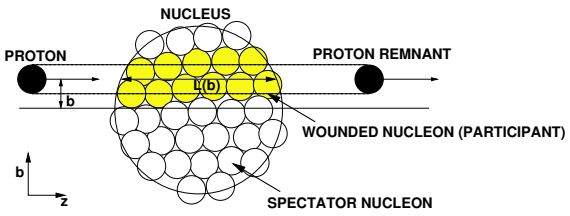

Figure 2.4: Schematic view of a proton-nucleus collision in the Glauber model. The projectile hits the nucleus with a certain impact parameter b. Only the nucleons along the projectile take part in the collision. Picture taken from [bru02].

Some general predictions for α_X can be obtained from this rather simple geometrical approach. If the target nucleus is approximated by a black disc (the probability of an inelastic interaction is unity for all impact parameters b smaller than the radius of the nucleus), then $\alpha_X = 2/3$, i.e. the cross section does scale with the surface of the disc (and is therefore shadowed by the nuclear medium). This behavior is approximately true for the total inelastic cross section, for which $\alpha_{inel} = 0.71$ has been found [car03]. If, however, the considered production cross section is very small (like it is the case for heavy quark production), $\alpha_X = 1$, since due to the small cross section the projectile "sees" all nucleons. Thus, from the point of view of the Glauber model $2/3 \leq \alpha_X \leq 1$ can be considered the valid region for the A-dependence of particle production cross sections. Note, however, that these considerations are valid for central production ($Y^* \approx 0$) only.

The Glauber model is able to describe most of the atomic number dependencies observed in inelastic cross section data. Refined models [bia82] allow also predictions for α_X in different regions of the phase space, as we will address below separately for the longitudinal and the transverse phase space.

2.2.2 Longitudinal phase space

The atomic number dependence of proton-nucleus cross sections is different for different regions of the longitudinal phase space [bia82], but its qualitative behavior described below is universal for all produced particles [cap91]. However, differences in the absolute values of α are found, depending on the size of the considered production cross sections. In explaining the effects that lead to a rapidity dependence of α we restrict ourselves to the inelastic cross section for simplicity.

Fig. 2.5 shows schematically the A-dependence of the inelastic cross section as a function of rapidity in the lab frame. The predictions for α_{inel} can be divided into three different regions following the ideas presented in [bia82]:

- In the backward hemisphere ($y < y_1$), $\alpha_{inel} = 1$. Partons from the inelastic interaction are relatively slow in this rapidity region, therefore they hadronize well inside the nucleus. These hadrons then undergo secondary interactions with the target nucleons (so-called intra-nuclear cascade).

- In the central rapidity plateau ($y_1 < y < y_2$) secondary interactions are not present any more, because the partons are fast enough to escape from the

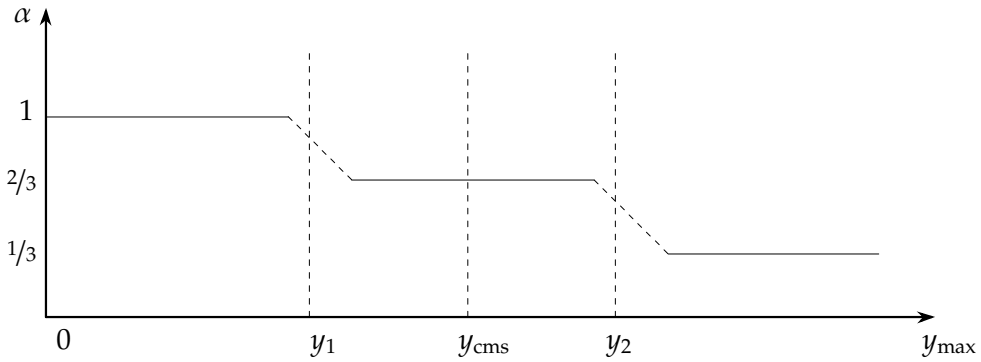

Figure 2.5: Simplified sketch of the A-dependence of the inelastic cross section as a function of rapidity. See text for further explanation.

nucleus before fragmentation takes place. With the argument that for large cross sections the nucleus can be approximated by a black disc, $\alpha_{inel} = 2/3$.

- The forward region ($y \to y_{\max}$) can only be reached if a single inelastic collision takes place. In this case the model expects $\alpha_{inel} = 1/3$.

Since for particle production cross sections the same qualitative behavior is predicted, we expect α_{K^*} for K^{*0} production at mid-rapidity to be approximately constant as a function of rapidity. We will test this prediction in section 6.3.2.

2.2.3 Transverse phase space

Within the Glauber model the atomic number dependence is expected to rise with increasing p_T [cap91], because large transverse momenta are identified with hard parton-parton scattering, for which the cross section is small. In the limit of high-p_T $\alpha = 1$ is naively expected.

However, the analysis of inclusive proton-nucleus data revealed that α can exceed one [cro75, cro77]. This was first interpreted as a cooperative behavior of the target nucleons and became known as the Cronin effect. In collisions of 400GeV protons on beryllium, titanium, and tungsten targets the maximum α was found at about $p_T = 5\,\mathrm{GeV}$, $\alpha_{max} \approx 1.1$ for $\pi^{\pm}$ and K^+ production and $\alpha_{max} \approx 1.3$ for p, $\bar{p}$, and K^- production (see fig. 2.6).

From the theoretical side a successful quantitative explanation of the Cronin effect is still missing [kop02]. Most of the models which explain the data at least qualitatively focus on the initial state, describing the effect as multiple scattering of the projectile's partons inside the target nucleus. In this way the mean p_T^2 of the proton-nucleus collision, $\left\langle p_T^2 \right\rangle_{pA}$, is enlarged with respect to ordinary proton-proton collisions. A rough estimate of the A-dependence of the effect is

$$\left\langle p_T^2 \right\rangle_{pA} - \left\langle p_T^2 \right\rangle_{pp} \propto A^{1/3}, \tag{2.6}$$

because the amount of multiple scattering is proportional to the path length of the projectile in the nuclear matter. Recently, in the context of nucleon-nucleon

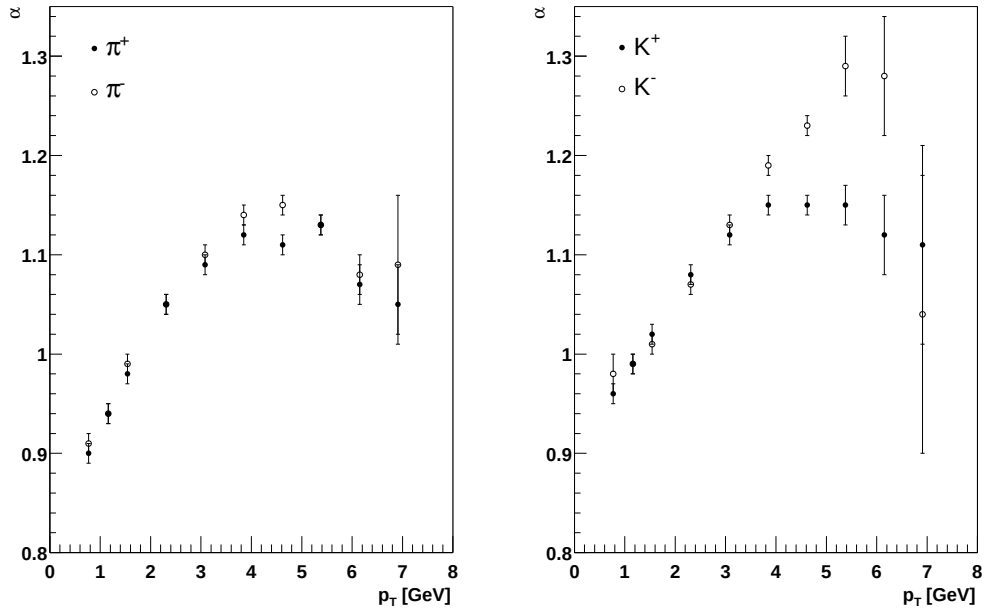

Figure 2.6: Atomic number dependence for the production of $\pi^{\pm}$ (left) and $K^{\pm}$ (right) as a function of p_T. For $p_T > 1.5\,\text{GeV}$ α exceeds one. Figures based on data from [cro77].

collisions, models came up explaining the Cronin effect as a final state effect, where soft partons undergo recombination rather than fragmentation (see e.g. [hwa04]).

When colliding relativistic nuclei, we expect to enter a completely different regime of physics, since deconfinement is predicted to take place. In the next section we will give a short introduction to the physics of the quark-gluon plasma and to the role that strange resonances play in discovering its properties.

2.3 AA collisions and the formation of QGP

Within the last years experiments at heavy-ion colliders have extensively studied relativistic nucleus-nucleus collisions. In such interactions a new state of matter is believed to be created, which is called the quark gluon plasma (QGP). In a QGP deconfinement takes place, i.e. within a short period of time quarks and gluons interact with each other as free particles.

Like in *pp* or *pA* collisions the properties of the QGP have to extracted from the analysis of the final state, so that signatures have to be found which can serve as probes for the existence of the QGP. Strangeness production and in particular strange resonances are supposed to be good probes of QGP. After a brief summary of the properties of the QGP we will explain why this is the case. In this we follow mainly the arguments in [sat00].

2.3.1 Properties of the QGP

Confinement is a long-range feature, which prevents the isolation of a single quark. On a short distance scale, shorter than typical distances in hadronic matter, the potential between two quarks becomes screened (color screening), much like the electric potential is screened in a dense medium (Debye screening).

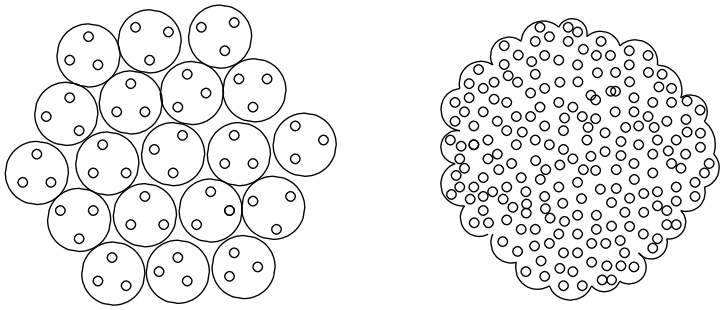

Figure 2.7: Schematic structure of two different states of hadronic matter [sat00]. *Left:* Nuclear matter is a compound of color-less hadrons. *Right:* In a QGP the density becomes so large that color screening 'melts' the hadrons, so that the quarks become unbound.

If the density of the medium exceeds a certain value, the medium does not behave as a collection of color-less hadrons any more but a phase transition to a plasma of unbound quarks and gluons takes place, where color can be exchanged freely (see fig. 2.7).

In AA collisions the energy density is expected to be high enough to produce this new state of matter. In lattice QCD calculations the critical temperature T_c to form a QGP is predicted to be about $0.1 - 0.2\,\mathrm{GeV}$. This is equivalent to a critical energy density ϵ_c of about $1 - 2\,\mathrm{GeV/fm^3}$. Comparing this value to the energy density of normal nuclear matter, which is in the range of about $0.15\,\mathrm{GeV/fm^3}$, it becomes clear that QGP cannot be created in normal inelastic pA collisions, at least not with the energy available at present colliders [sat00].

Given that a QGP can be created in an AA collision, questions about its life-time and cool-down mechanism arise. Fig. 2.8 shows a simplified sketch of the space-time propagation of an AA collision [mar02]. First, the actual quark gluon plasma is created. Driven by its own internal pressure the plasma expands and therefore cools down. At a certain time the density is small enough that confinement takes over, i.e. the plasma hadronizes into an intermediate state, which is called a hadron gas. The phase transition between the deconfined state and the hadronic state is called chemical freeze-out, because from that time on the hadronic abundances are fixed. Yet elastic interactions among the hadrons are possible.

Some time later the density has decreased so much that these elastic interactions stop, too. This is known as the thermal or kinetic freeze-out, since at this time also the kinematics of the hadrons are fixed, i.e. the final state observed by the experiment is formed.

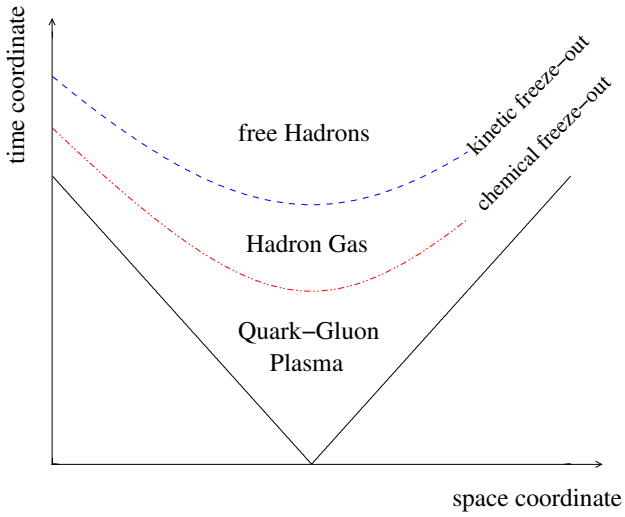

Figure 2.8: Simplified sketch of a space-time evolution of an AA collision [mar02]. Between the QGP and the hadronic final state, an intermediate state of elastically scattering hadrons is predicted.

Many probes of deconfinement are most sensitive when the chemical freeze-out is sudden, and the hadronic gas phase is short or non-existing. To study the properties of the QGP it is therefore important to know the temperature and mechanism of the chemical freeze-out and the life time of the hadron gas. Strange resonances are in particular suited for this, as will be explained in the next section.

2.3.2 Strange resonances as a probe of QGP

Strangeness enhancement. Already in 1982 the production of strange particles in a QGP was predicted to be enhanced with respect to ordinary pA and pp collisions [raf82]. The main reason is that the QGP is particularly rich of gluons, so that gluon-gluon fusion becomes the dominant channel in $s\bar{s}$ production [koc86]. Additionally, due to the high temperature of the QGP a thermal production of $s\bar{s}$ pairs is possible.

Strangeness enhancement is one of the important probes for the existence of the QGP. However, quantitative predicitons of this effect are difficult, since the magnitude of the enhancement does depend on the (unknown) life time of the plasma. In this context strange resonances can make an important contribution to the understanding of the temperature and the duration of the QGP phase.

Chemical freeze-out temperature. To estimate the temperature of the chemical freeze-out production ratios between resonances and quasi-stable particles are an important quantity. By comparing measurements of cross section ratios of K^*/K or $\Lambda(1520)/\Lambda$ with model calculations the critical temperature of the QGP can in principle be estimated [mar02], as is shown in fig. 2.9. Here, the cross section ratios measured in heavy-ion collisions are indicated by horizontal error bands. The theoretical predictions are shown as functions of the critical temperature, both for particle production at mid-rapidity ($\Delta y^* = \pm 0.5$, dashed lines) and for the full phase space (solid lines). The experimentally observed K^*/K ratio is compatible with a wide range of chemical freeze-out temperatures, while the $\Lambda(1520)/\Lambda$ ratio

prefers $T_c \approx 100\,\mathrm{MeV}$. However, a comparison of the experimental findings with theoretic predictions makes sense only if the observed resonance yields are not falsified by re-scatterings of the daughter particles in the hadronic gas phase. This complication we will address now.

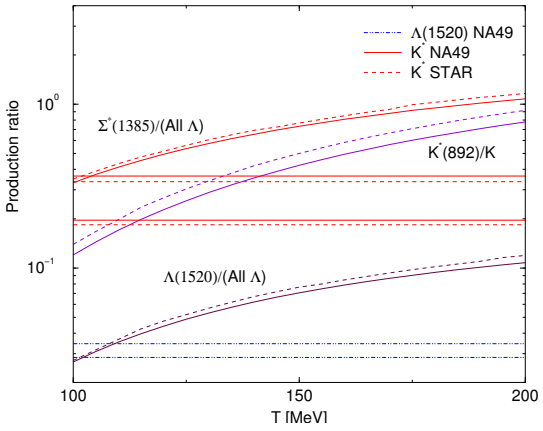

Figure 2.9: Experimental values (horizontal, 1σ error bands) and theoretical predictions of production ratios between resonances and stable particles as a function of the chemical freeze-out temperature [mar02]. See text for further explanation.

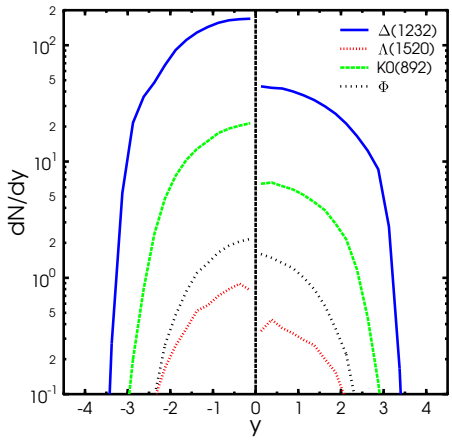

Figure 2.10: Comparison of rapidity distributions of produced resonances (left) and observed resonances after thermal freeze-out (right) [ble02]. Calculations are done for SPS energies.

Re-scattering and recombination. If the final state particles are subject to re-scattering in the hadronic gas phase, they might 'remember' relatively little about their primordial source. Resonance production is well suited to measure to what extend re-scattering takes place.

Since hadronic resonances have only short life times, most of them decay at the onset of the hadronic gas phase after having been created during the chemical freeze-out. Their daughter particles are then subject to re-scattering in the hadron gas. Since the production yield of the resonances is estimated from the reconstruction of invariant mass distributions, re-scattering may lead to distortions of the resonance signal, i.e. shifts of the resonance signals to lower masses, as observed recently in [fac04], broadening of the resonance width, or even losses in signal yield.

Fig. 2.10 shows model calculations [ble02] of yield loss for various resonances as a function of rapidity. The distributions of the resonances as they are produced in the QGP are shown on the left side of the figure. Due to rescattering of the decay particles in the hadron gas only a fraction of them can be experimentally observed in the final state. This is indicated on the right side of the figure. The predicted yield loss is 66 % for the $K^{*0}(892)$ and about 50 % for the $\Lambda(1520)$ at SPS energies. The size of the effect depends on the life time of the resonance, since the shorter the life time, the longer the path length of the daughter particles in the

hadronic gas phase. Therefore, the effect is smallest for the ϕ resonance, since it lives an order of magnitude longer than the K^{*0} ($c\tau$ = 46.2 fm compared to 3.9 fm). By comparing the yields of different resonances it is possible to gain a (hopefully consistent) picture of the duration of the hadronic gas phase.

2.4 Contribution of this analysis

In this chapter we have shown that the understanding of pA and AA collisions requires a detailed analysis of various subprocesses. On the theoretical side, many contributions to the scattering process cannot be reliably calculated, because low-energetic processes forbid the application of perturbative QCD. In this case, phenomenological approaches are used, which rely on experimental data for the tuning of their parameters.

It has been motivated that the analysis of K^{*0} production in proton-nucleus collisions does not only make a valuable contribution to the understanding of pA interactions, but can also serve as a normalization for the analysis of AA collision data, where the K^{*0} is due to its short life time particularly suited as a probe of quark-gluon plasma.

In this thesis we analyze K^{*0} and $\bar{K}^{*0}$ production in pA collisions at $\sqrt{s}$ = 41.6 GeV and mid-rapidity. We will present total and differential cross section measurements and their dependence on the atomic number of the target material. For the transverse distributions we will, for the first time, validate the Cronin effect for K^{*0} resonance production.

Chapter 3

The HERA-B experiment

The data for this analysis has been collected with the HERA-B detector operated at the HERA storage ring at DESY, Hamburg. After a brief overview of the primary physics goal and its implications on the detector design the experimental setup will be presented in more detail. Special focus is given to those detector components which were used in this analysis. The chapter closes with a brief description of the current physics program of HERA-B.

3.1 Overview

The HERA-B detector is a fixed-target forward spectrometer designed to measure CP violation in the system of neutral B mesons [loh94]. HERA-B operates up to eight different wire-targets in the halo of the 920 GeV proton beam of HERA, producing up to $4 \cdot 10^7$ proton-nucleus interactions per second. The dense hadronic environment imposes strong requirements on the data acquisition and trigger system as well as on the detector design. The setup of the HERA-B detector is briefly sketched below. More details on the individual subsystems are presented in section 3.3.

Because of the Lorentz-boost the products of the inelastic interaction move forward in a narrow cone in the laboratory system. The detector covers an angular range of 10-160 mrad in the non-bending plane and 10-250 mrad in the bending plane of the spectrometer magnet. This is equivalent to about 90 % of the solid angle in the center-of-mass system (CMS).

The target region is located in the center of the HERA-B coordinate system. As shown in the detector overview (fig. 3.1) it is directly followed by the Vertex Detector System (VDS), its main purpose being the separation of the decay vertex of B mesons from the main interaction point. Further downstream behind the spectrometer magnet a tracking system, subdivided into an inner and an outer part, provides a measurement of tracks from charged particles. The Inner Tracker (ITR) covers the inner part of the acceptance (10-30 mrad). It consists of micro strip gaseous chambers (MSGCs). The outer part of the acceptance is covered by the Outer Tracker (OTR) which is made out of honeycomb drift chambers. In

combination with the dipole magnet the tracking system provides a measurement of the charge and momenta of charged particles. Particle identification is done by three different devices: a Ring Imaging Čerenkov detector (RICH) is used for the separation of protons and charged kaons from pions, an Electromagnetic Calorimeter (ECAL) provides an electron-hadron separation, and a Muon Detector at the very end of the spectrometer identifies muons.

The HERA-B coordinate system is right-handed, with the z-coordinate pointing along the proton beam. The y-coordinate points to the top, and the x-coordinate to the center of the storage ring (which is, looking downstream the detector, to the left side). The center of the coordinate system is located in the target region, 4500 mm upstream with respect to the center of the magnet.

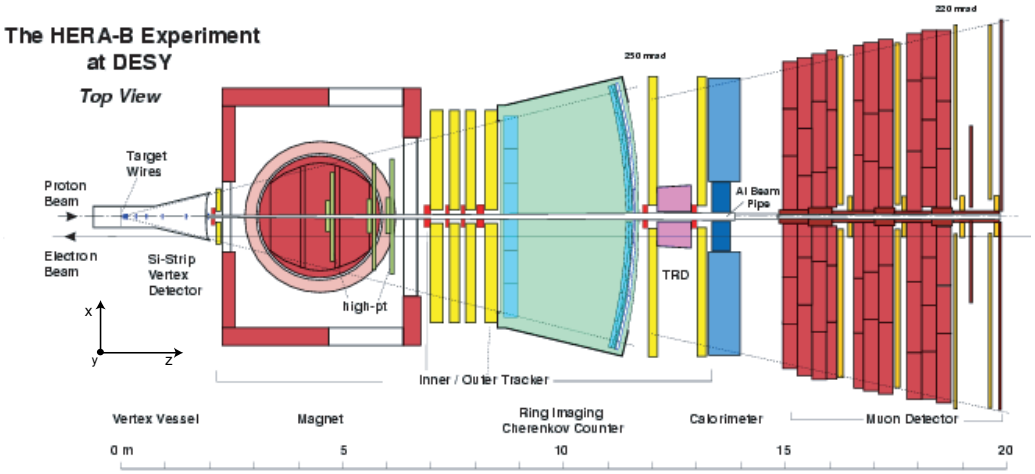

Figure 3.1: Top view of the HERA-B spectrometer in 2002.

3.2 Primary physics goal and detector requirements

The HERA-B detector was optimized to measure CP violation in the system of the neutral B mesons in the so-called golden decay mode:

$$B^0/\bar{B}^0 \rightarrow J/\psi(l^+l^-)\, K^0_S(\pi^+\pi^-). \tag{3.1}$$

The B^0 and $\bar{B}^0$ mesons decay into the same CP eigenstate $J/\psi K^0_s$, which has a clean signature due to two leptons in the final state forming a secondary vertex well separated from the vertex of the primary interaction (see fig. 3.2). The B^0 ($\bar{B}^0$) meson produced in an inelastic interaction of a beam proton with a target nucleus can either decay directly or oscillate into its anti-particle $\bar{B}^0$ (B^0) via a weak charged current process and decay afterwards. CP violation manifests itself in the interference between the amplitudes of the direct decay and the decay after oscillation (see e.g. [wal02]).

Due to the Lorentz boost and the rather long life-time of the B^0 mesons[1] they

[1] the B^0 life-time translates into a distance of 11 mm in the laboratory frame.

can be separated from prompt J/ψ decays coming directly from the target. This is done by looking for decay vertices detached by several millimeters from the primary interaction point.

Since both B^0 and $\bar{B}^0$ decay into the same final state, a method called "tagging" is used to figure out experimentally whether a B^0 or a $\bar{B}^0$ has been produced in the inelastic interaction. It uses the fact that B mesons are usually produced in pairs: if a conclusion about the quark content of the second (tagging) B can be drawn, the quark content of the first (signal) B at the time of its production is determined. As an example fig. 3.2 shows an event where the tagging is done by partially reconstructing a B^- meson ($\bar{u}b$). As the B^- contains a b-quark, the produced neutral B-meson contains a $\bar{b}$-quark and thus must be a B^0 ($d\bar{b}$). The tagging imposes additional requirements on the detector setup, like, as shown in fig. 3.2, capabilities to identify charged kaons.

At $\sqrt{s} = 41.6\,\text{GeV}$, the HERA-B center-of-mass energy, the $b\bar{b}$ production cross section $\sigma_{b\bar{b}}$ is about 30 nb/nucleon [abt03], i.e. it is suppressed by about 10^{-6} compared to the total inelastic cross section of $\sigma_{inel} \approx 43.5\,\text{mb/nucleon}$. Taking into account the branching ratios of the golden decay, $BR(B^0 \to J/\psi\, K_S^0) = 8.7{\cdot}10^{-4}$, $BR(J/\psi \to l^+\, l^-) \approx 6 \cdot 10^{-2}$, and $BR(K_S^0 \to \pi^+\pi^-) = 0.69$ [hag02], only one in 10^{11} inelastic interactions contains a golden decay. Therefore, $O(10^{15})$ inelastic interactions are necessary to collect a statistically significant sample of $O(1000)$ golden decays, if an overall detection efficiency of 10% is assumed. HERA-B's aim to collect this sample within three years of running requires that the target

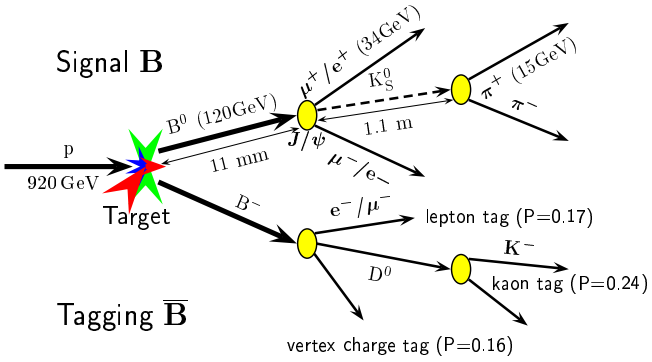

Figure 3.2: The tagging of a golden decay. The golden decay itself is shown in the upper decay branch, while the lower one shows the decay chain of a B^- as a possible tagging particle.

produces about $4 \cdot 10^7$ inelastic interactions per second.

Based on the primary physics goal the main requirement for the detector is an efficient selection of the golden decay in a high-rate environment. In detail, the following criteria have to be met:

- the target must provide an interaction rate of up to 40 MHz, and the detector must be able to handle the large particle flux in terms of radiation hardness

and occupancy,

- a good vertex resolution is needed to separate the decay vertex of the B^0 meson from prompt J/ψ decays coming from the primary interaction point,
- lepton identification (electrons as well as muons) is necessary to track down the decay of the J/ψ. In addition kaon identification is needed to identify the decay products of charged B-mesons for the tagging method,
- good momentum resolution is required to determine the J/ψ and K_s^0 masses,
- a fast and efficient trigger system is necessary to select events of interest and reject the large amount of background,
- a high-performance data acquisition is needed to cope with the large data flux.

The following section gives a more in-depth description of the different detector components, showing in which way the above requirements are realized. Section 3.4 deals with the trigger system and the data acquisition, and section 3.5 describes the reconstruction of the data.

3.3 Detector design

Before the detector subcomponents are described in detail, we shortly introduce the main properties of the HERA proton beam, as they are important for the understanding of the target design and the determination of luminosity.

3.3.1 Beam and target

The Hadron-Elektron-Ring-Anlage HERA [vos94] at DESY is a storage ring to collide electrons or positrons[2] with protons. The main goal of HERA is the investigation of the internal structure of the proton by means of deep inelastic scattering (DIS). The experiments H1 [abt97] and ZEUS [zeu93], located at the northern and southern interaction points (cf. fig. 3.3), respectively, mainly concentrate on the investigation of the parton dynamics, especially on the measurement of the proton structure functions. HERMES [dür95] is a fixed-target experiment using the polarized 27.5 GeV electron beam and polarized ^{1}H, ^{2}H or ^{3}He gas targets to measure the polarized structure functions of the neutron and the proton.

The HERA-B target is operated at the 920 GeV HERA proton beam. The beam is subdivided into 220 buckets with a temporal distance of 96 ns. 180 of the 220 buckets are filled with proton bunches. Before being filled into HERA the protons undergo a four-step pre-accelerator chain, consisting of the linear accelerator LINAC III, the synchrotron DESY III and the storage ring PETRA (see fig. 3.3). The chain of pre-accelerators leads to the characteristic filling scheme shown in fig. 3.4, comprising three so-called PETRA trains, which consist of 6 DESY III

[2] throughout this section, for simplicity, both electrons and positrons are denoted as "electrons".

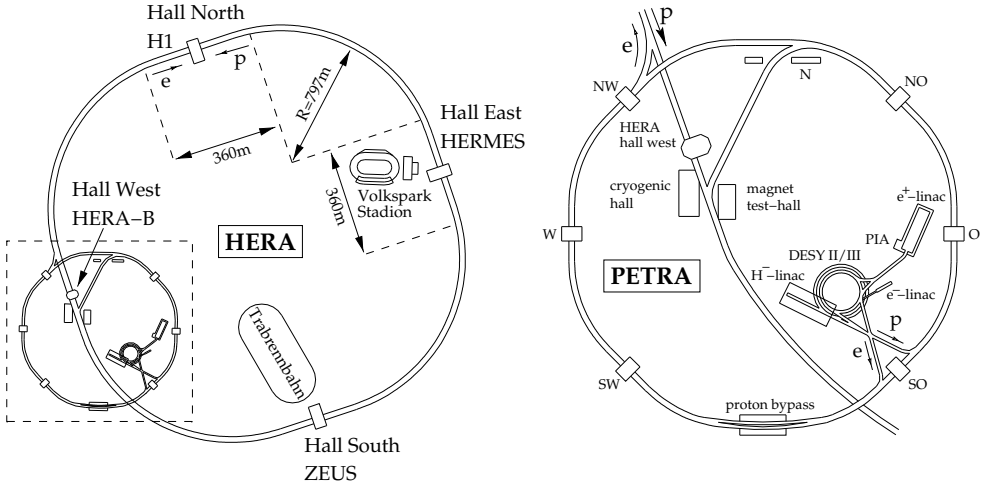

Figure 3.3: Schematic view of the HERA accelerator facility (left) and its pre-accelerator chain (right). The HERA-B experiment is located at Hall West on the DESY site.

trains of 10 bunches each.

The mean bunch crossing rate R_{bx} at the HERA-B target, calculated from the

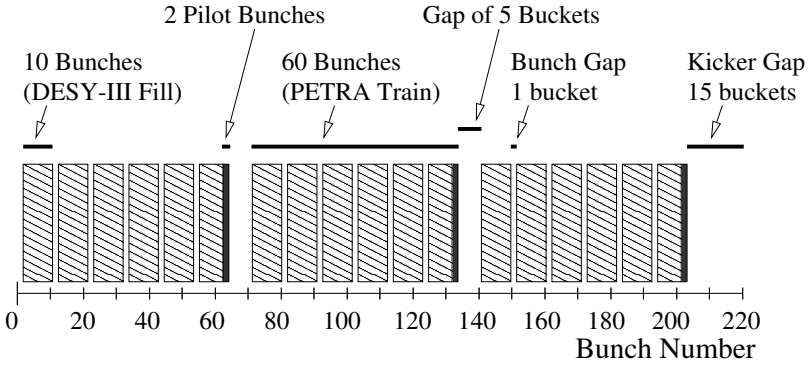

Figure 3.4: Filling scheme of the HERA proton beam, subdivided into three PETRA trains consisting of 6 DESY III trains of 10 bunches each. The pilot bunches at the end of each PETRA train do not have a colliding electron partner.

temporal distance of the buckets and the fraction of filled bunches, becomes

$$R_{bx} = \frac{180}{220}\frac{1}{96\,\mathrm{ns}} \approx 8.52\,\mathrm{MHz}. \tag{3.2}$$

The rate R_{ia} of inelastic interactions produced by the target can be expressed in units of R_{bx},

$$R_{ia} = \lambda \cdot R_{bx}, \tag{3.3}$$

where λ is the mean number of interactions per proton bunch. For the HERA-B design interaction rate ($R_{ia} = 40\,\mathrm{MHz}$), eq. (3.3) states that $\lambda = 4.7$ inelastic interactions per bunch crossing must be produced on average. The distribution

of the number of interactions per bunch crossing follows in good approximation a Poisson shape with expectation value λ [kni00].

To guarantee a clean vertex separation for simultaneous interactions the HERA-B target consists of eight thin wires grouped into two stations which surround the proton beam (cf. fig. 3.5). The inelastic interactions are shared between the wires, such that a proper vertex separation becomes possible. Each wire can be moved

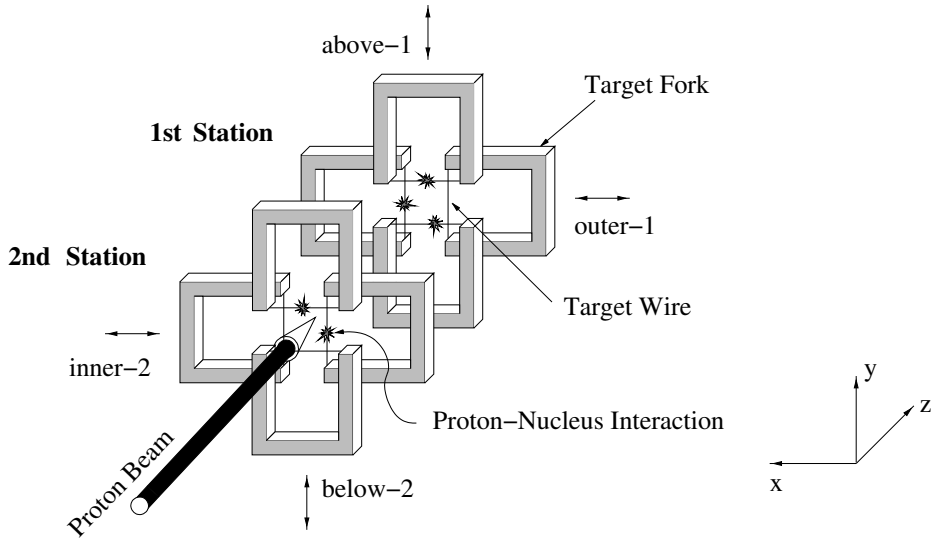

Figure 3.5: Sketch of the HERA-B target setup. Eight wires grouped into two stations surround the proton beam. The nomenclature of the wires is due to their position with respect to the proton beam. Based on [fun03].

independently into the beam by means of a precision mechanics [fun03] which is driven by stepping motors. An automatic steering system [iss01] is used to insert the targets into the beam, to keep the interaction rate constant, and to distribute the interactions equally among the operated wires. To keep the rate constant the target wires have to be moved constantly into the beam, scraping at the beam core. A typical velocity is about 50 μm/h for a single target at design rate.

The interaction rate is measured by a set of scintillating counters [bön02] installed at the exit window of the RICH. The equalization of the rate among the operated wires is realized by a system of charge integrators [vas99] connected to the target wires. They measure electric charges produced by δ-electrons which are knocked out of the target material. The amount of charge produced on a wire is directly proportional to the number of interactions on this wire.

HERA-B operates targets of different materials, which are either thin foils of dimensions 500 μm along the beam and 50 μm transverse to the beam, or round wires with a diameter of typically 50 μm. Details of the wire configuration used in the 2002/2003 run can be found in table 3.1.

In order to guarantee an efficient data taking and a stable operation together with the other HERA experiments the target system must meet several requirements,

target	material	geometry
above-1	$^{13}_{27}$Al	$50 \cdot 500\,\mu\text{m}^2$ ribbon
below-1	$^{6}_{12}$C	$100 \cdot 500\,\mu\text{m}^2$ ribbon
inner-1	$^{74}_{184}$W	50 μm round
outer-1	$^{22}_{48}$Ti	50 μm round
above-2	$^{46}_{106}$Pd	50 μm round
below-2	$^{22}_{48}$Ti	50 μm round
inner-2	$^{6}_{12}$C	$100 \cdot 500\,\mu\text{m}^2$ ribbon
outer-2	$^{6}_{12}$C	$100 \cdot 500\,\mu\text{m}^2$ ribbon

Table 3.1: Target materials used in the 2002 running. Those targets printed in bold have been used to produce the data used in this analysis.

which concern the stability and the safety facilities of the setup. Special care is needed in the implementation of the steering system. Its redesign is the topic of the technical part of this thesis which is covered in appendix A.

3.3.2 Vertex Detector System

The HERA-B vertex detector system (VDS) [knö03] is designed to provide a good spatial separation between the point of the primary interaction on the target wire and the secondary vertex of the decaying $B^0/\bar{B}^0$. It offers stand-alone tracking capabilities, which make a matching of the main tracker segments behind the magnet with those of the VDS possible.

Located directly behind the target system the vertex detector consists of eight stations (superlayers) covering an angular range of $10 - 250\,\text{mrad}$ (cf. fig. 3.6). Each superlayer consists of four modules of two double-sided, 300 μm thick micro-strip detectors with an active area of $50 \cdot 70\,\text{mm}^2$. The strips at the front and the backside of each layer are orthogonal to each other, which allows the precise reconstruction of hits in space. To reduce the number of space-point ambiguities, the strips of the two layers are tilted by $\pm 2.5^\circ$ with respect to the vertical and horizontal axis.

To obtain good acceptance for small angle tracks the vertex detector is designed to operate at a radial distance of about 10 mm from the proton beam center. Since the spatial resolution is dominated by multiple scattering inside the material between the vertex and the first point of the track measurement (e.g. inside the beam pipe), superlayers 1-7 are operated inside the vertex vessel which is part of the beam pipe. The setup is shielded against RF-fields of the beam by thin aluminum caps and placed in a secondary vacuum. Superlayer 8 is operated under normal pressure behind the exit window of the vertex vessel, just in front of the magnet.

The single hit resolution of the vertex detector is about 12 μm, the primary vertex resolution is about 50 μm in transverse direction, and about 500 μm along the

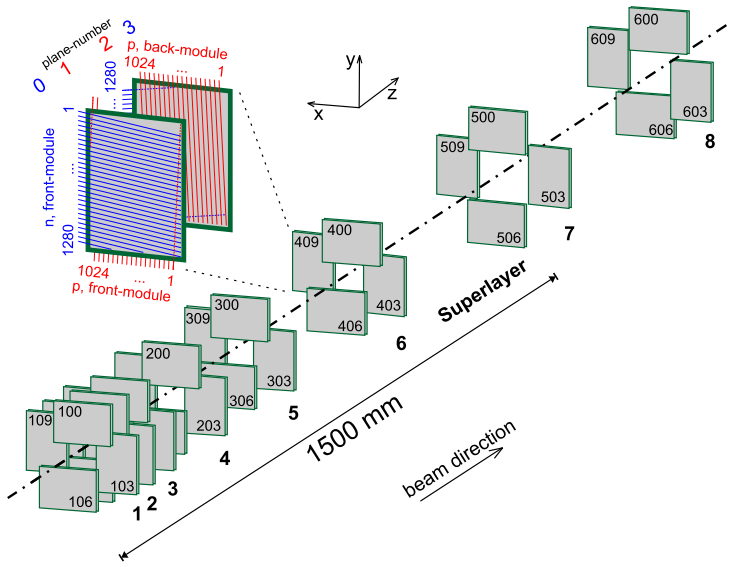

Figure 3.6: Schematic view of the vertex detector system [brä01].

beam [knö03].

3.3.3 Magnet and tracking system

The tracking of charged particles is provided by two tracking systems. The Inner Tracker covers the region close to the beam pipe, while the Outer Tracker starts at about 20 cm radial distance from the beam pipe. Each system comprises seven superlayers, the first one positioned between the VDS and the magnet. The next four superlayers are placed behind the magnet, the last two between the RICH and the calorimeter. Both tracking systems consist of vertically oriented wires or strips. To make the reconstruction of full 3-dimensional tracks possible some layers of each superlayer are tilted by ±5° with respect to the vertical axis.

Magnet. The HERA-B dipole magnet produces a field integral of 2.2 Tm. The magnetic field points along the y-axis, i.e. particle trajectories are bent in the horizontal plane. Their curvature is determined by the tracking system, which provides a measurement of momentum and charge.

Inner tracker. The Inner Tracker (ITR) [bag02] covers an acceptance of approximately 10 to 30 mrad. About half of the tracks of a typical inelastic event pass the Inner Tracker, therefore it was designed to cope with high radiation doses of about 1 Mrad/year.

The Inner Tracker is composed of micro strip gas chambers (MSGCs), as shown in fig. 3.7. It is operated with a gas mixture of Ar and CO_2. Charged particles crossing the drift volume ionize the gas atoms, and the free electrons drift towards readout strips, guided by an electric field. Near the anode strips the electrons

are strongly accelerated and in turn ionize additional gas atoms, so that an amplification of the signal takes place (so-called gas gain). In order to minimize the probability of sparks a gas electron multiplier (GEM) foil was placed in between the readout anode and the drift cathode. The GEM foil provides an additional amplification of the electron signal, which allows an operation at lower cathode voltage.

Each superlayer of the Inner Tracker is composed of up to eight single layers. The

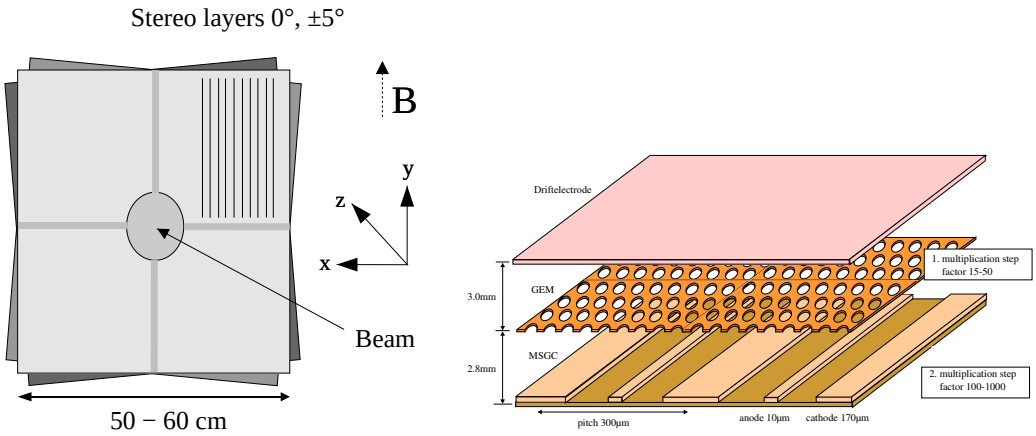

Figure 3.7: Front view of an ITR superlayer (left) and schematic view of an ITR chamber (right). The readout layer on the bottom is covered by the GEM foil. The drift cathode layer is shown on top [zie98].

pitch of the readout strips is 300 μm, which results in a hit resolution of about 90 μm.

In the data taking period 2002/03 the operation of the ITR showed several instabilities and inefficiencies, which led to the decision not to use it in the presented analysis. This reduces the acceptance in the forward region significantly and limits the solid angle coverage from 90 % to about 70 % in the center-of-mass frame.

Outer tracker. In the outer part of the HERA-B acceptance the track density is significantly lower than in the inner part of the detector. A lower granularity is therefore sufficient, and a different technology was chosen for the Outer Tracker (OTR) [hoh01], which covers an angular acceptance of about 25-250 mrad. It is built of honeycomb drift chambers, operated with a mixture of Ar and CO_2. This time the electrons of the ionized gas drift to an anode wire. For a precise determination of the radial distance of the particle track to the wire the drift time of the electrons to the wire is measured. The distance can then be computed by means of the so-called space-drift-time relation, which is a function of the gas mixture, its pressure, the voltage, and the geometry of the drift cell. The drift cells in the inner part of the Outer Tracker have a diameter of 5 mm, the outer part is made of 10 mm cells. A superlayer consists of six single layers of drift tubes.

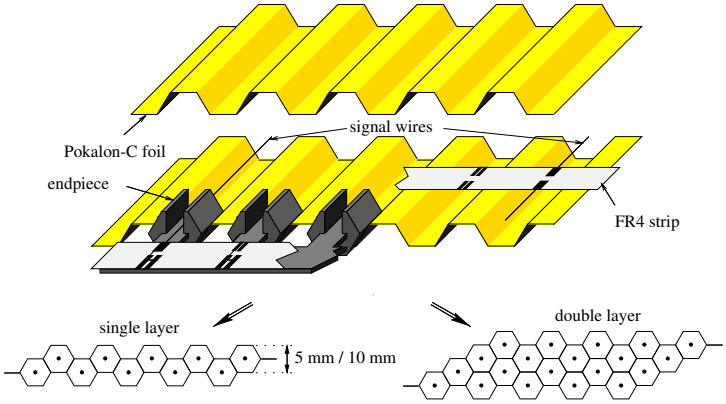

Figure 3.8: Honeycomb structure of the Outer Tracker modules. On the bottom of the figure the staggering of the drift cells to single and double layers is shown.

3.3.4 Particle Identification

Particle identification is performed using a combination of

- a momentum measurement from the curvature of the particle track in the magnetic field and
- a measurement of the particle's energy or velocity.

With this information the mass of the particle can be deduced, hence the particle be identified.

The particle identification devices of HERA-B are subject to the following paragraphs. Special emphasis is given to the Čerenkov counter, which has been used in the analysis presented in this thesis.

Ring Imaging Čerenkov Counter. The HERA-B RICH [ari04] is designed to separate electrons from pions in the momentum range from 3.4 to 15 GeV, pions from kaons within 10 to 54 GeV, and kaons from protons within 23 to 85 GeV.

The RICH makes use of the Čerenkov effect, which is a non-isotropic polarization of a dielectric medium (called radiator) by a charged particle with velocity v larger than the speed of light, c/n, in the medium. $n(E)$ is the (in general energy dependent) refractive index of the medium. When the excited atoms of the medium return to ground state, constructive interference makes the medium emit light. The light forms a cone centered around the particle's path, the opening angle θ_c of the cone being defined by the particle's velocity $\beta = v/c$:

$$\cos\theta_c = \frac{1}{n(E)\beta}. \tag{3.4}$$

From (3.4) it follows that the minimal velocity which a particle must have to generate Čerenkov light is $\beta_t = 1/n(E)$. At this threshold Čerenkov light is radiated in forward direction, since $\cos\theta_c = 1$. The maximum Čerenkov angle θ_c^{max}

depends on the refractive index of the radiator and is reached in the limit of the particle approaching $\beta = 1$. In combination with a momentum measurement both the threshold behavior and the measurement of the Čerenkov angle can be used to identify the particle.

The radiator of the HERA-B RICH is gaseous C_4F_{10} stored in a vessel of 108 m^3

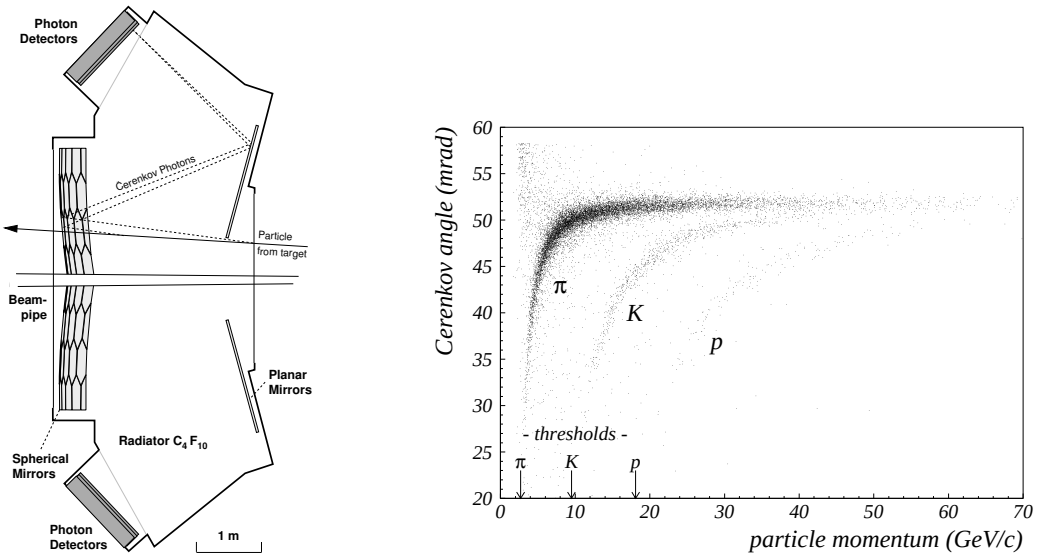

Figure 3.9: *Left:* Schematic side-view of the RICH detector. *Right:* Measurement of the Čerenkov angle as a function of momentum for different particles. The Čerenkov thresholds for pions, kaons, and protons are indicated by the arrows. Both from [ari04].

volume (cf. fig. 3.9). The RICH vessel is operated with atmospheric pressure. The pressure inside the vessel is monitored, which allows for corrections of the refractive index when the data is reconstructed.

On its 2.82 m long path across the vessel a $\beta = 1$ particle radiates 32 photons on average. The refractive index of the radiator is $n = 1.00137$, so that the Čerenkov angle of a $\beta = 1$ particle is $\theta_c^{max} = 51.5$ mrad. The radiator was chosen on the one hand to guarantee a sufficiently large difference for the Čerenkov angle of pions and kaons even at high momenta (around 0.9 mrad at 50 GeV/c). On the other hand the low Čerenkov threshold for these particles allows a separation of pions and kaons down to momenta of 9.6 GeV, as shows the right side of fig. 3.9.

To measure the Čerenkov angle a system of planar and spherical mirrors projects the light cone onto two detector planes outside the spectrometer's acceptance, where the radiated light forms a ring. Its radius is proportional to the Čerenkov angle. The detector planes are equipped with 27000 readout channels on 2240 multi-anode photo multipliers. The granularity of the system is chosen such that the occupancy of each readout channel does not exceed 10% at 40 MHz interaction rate.

The analysis presented in this thesis makes extensive use of the kaon identification properties of the RICH. The efficiency to identify a kaon track within the large

pion background[3] is between 60-95 % for track momenta between 10-60 GeV. Even more important is the pion rejection efficiency, which is about 95 % for tracks above the kaon threshold. More on particle identification with the RICH can be found in section 4.2.3.

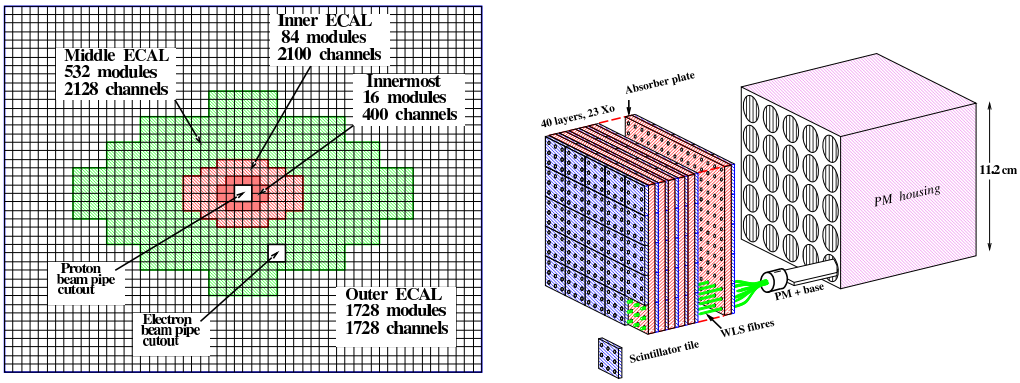

Figure 3.10: *Left:* Schematic view of the ECAL cell structure. *Right:* Survey of the sandwich structure of a module of the inner part of the ECAL.

Electromagnetic calorimeter. The electromagnetic calorimeter [zoc00] is used to separate electrons and photons from hadrons. In total, the calorimeter is composed of 2344 modules (so-called towers), which consist of layers of absorber material sandwiched with scintillator plates. The scintillator light is guided by fibers of wavelength shifters to photomultiplier tubes at the backplane of each tower (so-called shashlik-readout). The ECAL is subdivided into three regions of different granularity (cf. fig 3.10). The absorber material for the inner part is 13.6 cm of tungsten (22 radiation lengths), while for the middle and outer ECAL 33 cm (20 radiation lengths) of lead is used.

Photons are identified as stand-alone showers in the calorimeter. Electrons show an additional track pointing towards the shower. Since they are fully stopped in the calorimeter, the momentum of the track is approximately equal to the energy deposited in the shower, $E/p \approx 1$. In contrast to this hadrons deposit only a fraction of their energy in the ECAL, $E/p \ll 1$. This criterion is used for the electron/hadron separation.

The ECAL is already used at pre-trigger level to identify e^+e^- pairs as candidates of the J/ψ decay.

Muon detector. The muon system [are01] is located at the very end of the detector. It provides a separation of muons from hadrons. The muon detector consists of four superlayers (see fig. 3.11), the first three of them shielded by heavy absorbers of concrete and steel, which stop all particles but muons above a momentum of 4.5 GeV. The muon tracks are measured by a set of proportional

[3] about 80% of the reconstructed tracks are pions.

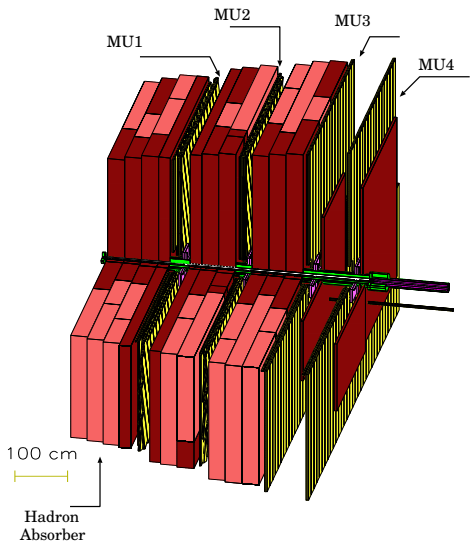

Figure 3.11: Schematic view of the muon detector. The proton beam comes from the left.

chambers in the outer region and gas pixel chambers in the inner part to cope with the higher track density.

Hits in the muon detectors are used by the pre-trigger system to search for muon pairs originating from the J/ψ decay.

3.4 Trigger system and data acquisition

HERA-B operates two different types of triggers. The lepton pair (or di-lepton) trigger is used for physics with two leptons in the final state, while the minimum bias trigger does not enhance a special signature. During the data taking period 2002/03 about $150 \cdot 10^6$ di-lepton triggers and $210 \cdot 10^6$ minimum bias triggers were accumulated.

3.4.1 Lepton pair trigger chain

The lepton pair trigger system was designed to select the clean signature of the golden decay with two high-p_T leptons in the final state, which stem from the decay of the J/ψ. The 520.000 channels of the HERA-B detector are read out with each bunch crossing, i.e. with a rate of 10.4 MHz. The trigger system reduces this event rate in three steps. Those events surviving the selection are written to tape for later analysis. The trigger system is divided into three active components, which are briefly introduced below in the order in which the triggering process takes place.

- The first step is performed by the so-called **Pretrigger System** [sch01], which forms candidates of lepton track pairs (so-called seeds). The muon pretrigger looks for coincidences in the last two chambers of the muon detector, while the electron pretrigger searches for pairs of high energetic clusters in the ECAL. The track candidates are sent to the First Level Trigger.

- The **First Level Trigger** (FLT) [nör03] traces back the track candidates towards the magnet. This is done by using the hit information of dedicated trigger chambers of the Outer Tracker[4]. Starting with the pretrigger information a network of track finding units (TFUs) extrapolates the track candidate back to the magnet, requiring detector hits in each trigger chamber within so-called regions of interest (ROIs), which are search windows defined basically by the slopes of the track (see fig. 3.12). With this method a large amount of hit combinations can be checked within a short period of time. The event is rejected if no lepton pair candidate was found. The rejection factor is about 200, reducing the input rate to the next trigger level to 50 kHz.
  At the end of the track finding process, the trigger decision unit (TDU) estimates the momenta of the tracks and the invariant mass of the lepton pair. If this is found to be in the range of the J/ψ mass, the TDU passes all track information to the Second Level Trigger.

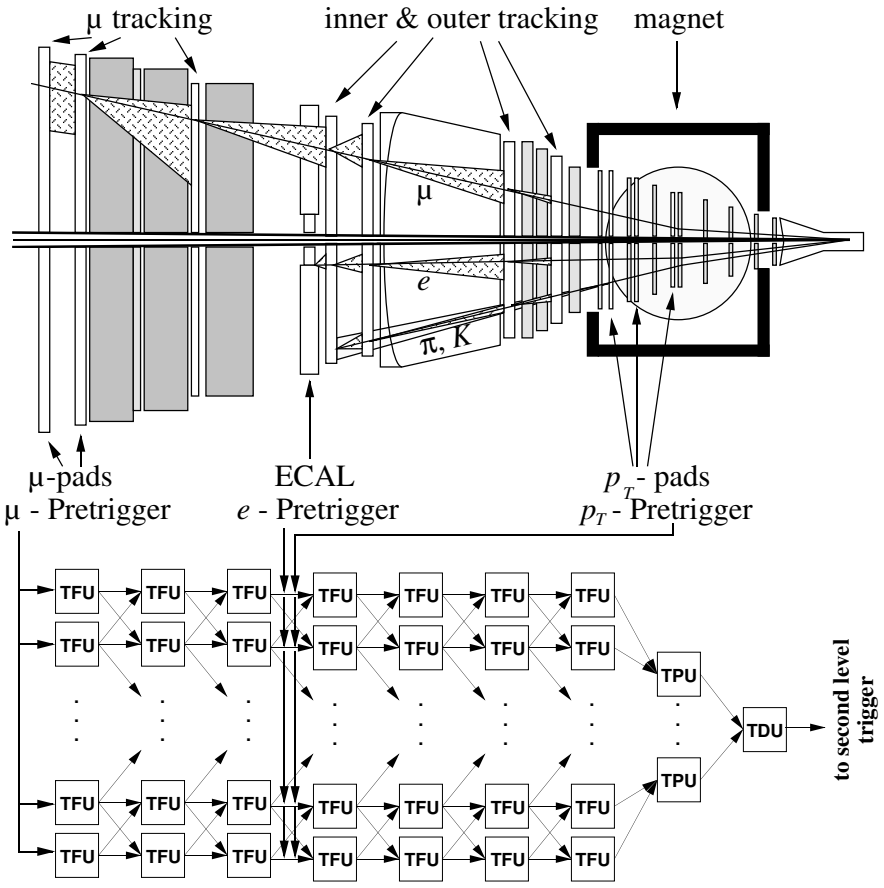

Figure 3.12: Schematic view of the HERA-B first level trigger system (based on [con02]).

- The **Second Level Trigger** (SLT) [dam03] is implemented as a software trigger running on a farm of 240 personal computers. To refine the track

[4] in 2002/03, the Inner Tracker was not included in the trigger chain.

parameters the hit information of all detector layers is used. Furthermore, the drift time information of the Outer Tracker chambers is taken into account to get a better spacial resolution. The Second Level Trigger propagates the tracks through the magnet using the vertex detector information. If the tracks can be combined into a common vertex the event is accepted. The SLT reduces the event rate by about a factor of 100.

The events having survived the SLT are passed to another farm of personal computers, called the **Fourth Level Trigger** (4LT) [her01] for historical reasons. However, no further event rejection takes place on the 4LT but the full reconstruction of a part of the events for online data quality, using the full calibration and alignment information.

The **Data Acquisition** (DAQ) integrates all trigger levels and the logging of the data into a common framework. It controls the data flow between the different trigger steps and keeps the event data in pipelines and buffers while waiting for the FLT and SLT decisions. Additionally, it schedules the distribution of events on the SLT and FLT farms and writes all accepted and reconstructed events to tape storage.

3.4.2 Minimum bias triggers

In contrast to the lepton pair trigger the minimum bias triggers do not enhance a special decay signature. Therefore, they allow for a wide range of physics studies, but are not able to select rare processes.

Interaction trigger. During the data taking in 2002/03 the target was operated at rather moderate interaction rates of about 1.5 MHz. Considering the HERA bunch crossing rate (eq. (3.2)), the fraction of events which do not contain an inelastic interaction (so-called empty events) is about 83 % (assuming that the number of inelastic events per bunch follows a Poisson distribution).

The interaction trigger, being implemented as a pure software trigger running on the SLT farm, is used to reject those empty events. Therefore, only a very low trigger threshold is needed. An event is accepted if one of the following conditions is fulfilled:

- the number of hits in the RICH is greater than 20 or
- a cluster with an energy of more than 1 GeV is found in the inner part of the ECAL.

Since the event rate is too large to trigger all interactions a pre-scaling is provided which reduces the logging rate to about 1000 Hz.

The efficiency ϵ_{trig} of the interaction trigger is an important ingredient of the cross section measurements, because it enters the calculation of the luminosity (see section 3.6). It has been evaluated using the Monte-Carlo simulation [som03]. Due to the soft trigger threshold the efficiency $\epsilon^{(1)}_{trig}$ to trigger a single interaction

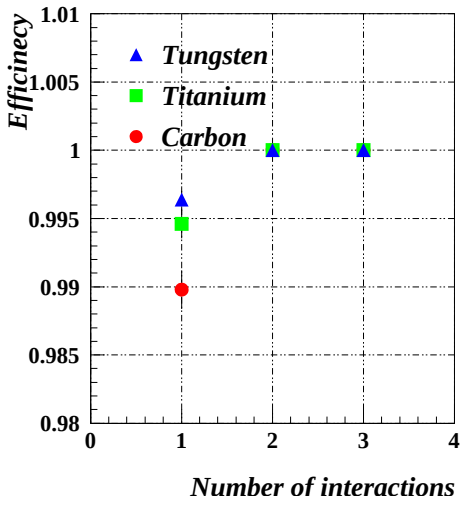

Figure 3.13: Interaction trigger efficiencies [som03] for the different target materials as a function of the number of inelastic interactions per event.

Target	$\epsilon^{(1)}_{\text{trig}}$
carbon	99.0%
titanium	99.4%
tungsten	99.6%

Figure 3.14: Summary on interaction trigger efficiencies for the different target materials. The efficiency is given for exactly one inelastic interaction in the event [som03].

per event is about 99 % (cf. table 3.14). It depends slightly on the multiplicity and therefore on the target material, as is illustrated in fig. 3.13. For two or more simultaneous interactions the efficiency is 100 % for each target material.

Random trigger. To study possible biases of the physics triggers and to make a luminosity determination for lepton pair triggered data possible about 5% of the events were taken with the so-called random trigger, which was operated simultaneously to the physics trigger. Regardless of the physics content the random trigger accepts events in a random manner, i.e. the probability to accept an event is flat among all HERA buckets. Therefore, for most of the randomly triggered events the detector is empty, either because the protons of a filled bunch did not interact with the target material or because one of the unfilled HERA buckets passed the target region.

3.5 Data reconstruction

The reconstruction of the data can be subdivided into six different steps, which are briefly sketched below.

- The **hit preparation** is the first step of the reconstruction. Here the signals from the subdetectors are translated into space points. For the ECAL the deposited energy in the cells is combined into clusters.
- In a second step the **segment reconstruction** takes place. That means that the hits within the individual tracking systems are combined into track segments, using pattern recognition algorithms. Each tracking system uses a stand-alone tracking, i.e. the track segments stays within the respective tracking system.

- Afterwards the segments found by the segment reconstruction undergo the **track matching** procedure. Each segment found in the vertex detector is combined with each segment from the main trackers (ITR and OTR) by propagating the track segments through the magnet.
  Note that at this stage segments from the VDS might have been matched to more than one segment in the main trackers. Given the large track multiplicity at HERA-B those "clone tracks" appear frequently and have to be removed afterwards in a so-called clone removal procedure.

- After the track reconstruction **particle identification** (PID) algorithms apply certain particle hypotheses to the tracks. First of all each track is propagated to the muon system. Based on the hit pattern in the muon chambers the likelihood that this track represents a muon is calculated.
  Afterwards, RITER [pes01], the track based PID algorithm of the RICH, searches for rings and calculates the opening angle of the Čerenkov cone. Using the momentum information from the track RITER calculates likelihoods for charged kaon, proton, light particle (e, μ, π), and background hypotheses.

- To prevent track segments from being used more than once to build tracks a **clone removal** routine [ple02] is applied. For a pool of segment combinations the best-matching track candidate is calculated, favoring long tracks (with many hits) and a good χ^2/n.d.f. In case two or more tracks use the same track segment only the best-matching track is considered.

- The last step in the event reconstruction is the **primary vertex reconstruction**. The algorithm searches for clusters of tracks which point towards the position of the target. The final vertex position is derived in an iterative procedure using Kalman filter techniques.

3.6 Luminosity determination

The luminosity $\mathcal{L}$ of the data set is a crucial ingredient to every cross section measurement. It is the connection between the number N of produced particles of a certain type and the production cross section σ:

$$\sigma = \frac{N}{\mathcal{L}}. \tag{3.5}$$

Thus, it is a process-independent measure of the amount of data taken. At HERA-Bthe luminosity is determined by counting the number of inelastic interactions produced, N_{ia}, and dividing by the inelastic production cross section σ_{inel}. This chapter summarizes the ingredients and the basic recipe to arrive at a robust luminosity determination.

Inelastic cross section. The inelastic cross section σ_{inel}^{pA} at the HERA-B center-of-mass energy can be extrapolated from previous experiments colliding protons

on nuclear targets (see [car03] and references therein). From the measurements also the atomic mass dependence of the cross section is derived:

$$\sigma_{inel}^{pA} = (43.55 \pm 0.40) \cdot A^{(0.71111 \pm 0.0011)} \text{ mb}. \tag{3.6}$$

The inelastic cross section can be subdivided into a non-diffractive (called minimum bias) and a diffractive part:

$$\sigma_{inel}^{pA} = \sigma_{MB} + \sigma_{TSD} + \sigma_{BSD} + \sigma_{DD}. \tag{3.7}$$

Here, σ_{MB} is the non-diffractive part of the inelastic cross section, while σ_{TSD}, σ_{BSD}, and σ_{DD} are the target single diffractive, the beam single diffractive, and the double diffractive cross sections, respectively.

The single diffractive cross sections are of the type $pA \to pX$ (TSD) or $pA \to XA$ (BSD), i.e. either the beam proton or the target nucleus remains in its ground state, while the other one is excited. TSD and BSD events are mostly outside the HERA-B acceptance, because they consist mainly of high or low rapidity tracks. Their contribution to the inelastic cross section is of the order of 4-7% [car03]. The double diffractive cross section is about an order of magnitude smaller than the single diffractive cross sections and can be safely neglected. The same is true for contributions due to double pomeron exchange.

The inelastic cross sections are summarized target-wise in table 3.2.

Recorded luminosity. Generally one has to distinguish between the delivered luminosity, $\mathcal{L}_{deliv}$, corresponding to the produced number of beam-target interactions, and the luminosity $\mathcal{L}_{rec}$ of the recorded data sample. At HERA-B a pre-scaling factor of about 10^{-3} is applied because the logging speed is limited to 1000 events/s, while the interaction rate is of the order of 1 MHz. Hence, $\mathcal{L}_{rec} \approx 10^{-3} \cdot \mathcal{L}_{deliv}$.

The recorded luminosity $\mathcal{L}_{rec} =: \mathcal{L}$ can be expressed as

$$\mathcal{L} = \frac{\lambda \, N_{BX}}{\sigma_{inel}}, \tag{3.8}$$

with N_{BX} being the number of filled bunches which have been offered to the interaction trigger during the time of the run (after pre-scaling). λ is the mean number of inelastic beam-target interactions per filled bunch, as defined in (3.3). N_{BX} and λ can be determined separately, as will be sketched in the following.

Mean number of interactions. The probability that n inelastic interactions take place within the same bunch crossing follows in good approximation a Poisson distribution with expectation value λ [kni00]:

$$\mathcal{P}(n, \lambda) = \frac{\lambda^n}{n!} e^{-\lambda}. \tag{3.9}$$

λ can be derived from the interaction rate R_{ia}^{hodo} measured by the target hodoscope system:

$$\lambda = \frac{K(A)\, R_{ia}^{hodo}}{R_{BX}} = \frac{K(A)\, R_{ia}^{hodo}}{8.523\,\mathrm{MHz}}. \tag{3.10}$$

Here, R_{BX} is the mean bunch crossing rate (from (3.2)), and $K(A)$ is a correction factor that accounts for different multiplicity distributions of the various target materials, which affect the acceptance of the hodoscope system [aus04]. $K(A)$ is defined relative to the geometrical acceptance of the hodoscope system which is about 1 % [5]. What regards the luminosity used in this analysis, $K(A)$ has been derived from the analysis of ECAL energy spectra. Its values are listed in table 3.2. More independent methods to derive $K(A)$ exist. They are extensively discussed in [abt04].

target	σ_{inel}^{pA} [mb]	$K(A)$
C	237.4 ± 3.4	1.748 ± 0.030
Ti	645.1 ± 7.5	1.412 ± 0.034
W	1710.0 ± 17.0	1.172 ± 0.044

Table 3.2: List of inelastic cross sections [car03] and hodoscope correction factors $K(A)$ [aus04] to derive the luminosity used in this analysis.

Number of filled bunches. The number of filled bunches N_{BX} offered to the interaction trigger after pre-scaling is derived from the number of recorded events N_{rec}. Since the trigger has only a finite efficiency $\epsilon_{trig}^{(n)}$ to trigger events with n simultaneous inelastic interactions, N_{rec} can be expressed by summing the trigger efficiencies folded with the probability to have n inelastic interactions in the event

$$N_{rec} = N_{BX} \sum_{n=0}^{\infty} \mathcal{P}(n,\ \lambda)\, \epsilon_{trig}^{(n)}. \tag{3.11}$$

If we parameterize $\epsilon_{trig}^{(n)}$ by a factorization ansatz,

$$\epsilon_{trig}^{(n)} = 1 - \left(1 - \epsilon_{trig}^{(1)}\right)^n, \tag{3.12}$$

where $\epsilon_{trig}^{(1)}$ is the efficiency for exactly one inelastic interaction, (3.11) becomes

$$N_{rec} = N_{BX}\left(1 - e^{-\lambda\ \epsilon_{trig}^{(1)}}\right). \tag{3.13}$$

The interaction trigger efficiencies have already been introduced in section 3.4.2 and are summarized target-wise in table 3.14 on page 44.

[5] large systematic uncertainties prevent, however, a precise determination of the hodoscope acceptance.

Complete formula. Knowing the trigger efficiency and the number of recorded events all information is provided to calculate the luminosity of the recorded data sample:

$$\mathcal{L} = \frac{\lambda\, N_{BX}}{\sigma_{inel}^{pA}} = \frac{\lambda\, N_{rec}}{\sigma_{inel}^{pA}\left(1 - e^{-\lambda\epsilon_{trig}^{(1)}}\right)}. \tag{3.14}$$

Corrections to this formula arise from different kinds of background events like detector noise that is triggered unintentionally or interactions due to the coasting beam [spr00]. At the time of this analysis no correction for background events was applied, but the systematic error on the luminosity (about 3.5% depending on the target material) does include the so far best knowledge on these contributions. The luminosities are listed run-wise in appendix C.

3.7 Physics program of HERA-B

The primary physics goal of HERA-B has been the measurement of CP violation in the system of the neutral B-mesons. The idea was that HERA-B could establish a precise measurement of CP violation before the B-factories and their detectors BaBar [bab98] at SLAC and Belle [bel94] at KEK went into operation. However, due to several technical problems the start-up of the experiment was delayed, making it impossible to compete against the by-then already operating B-factories.

After the HERA-II upgrade[6] in 2001 the HERA-B collaboration came up with a modified physics program [her00] for the running period 2002/2003, which is briefly described below. It is mainly devoted to a measurement of the $b\bar{b}$ cross section, to charmonium and open-charm physics, and to strangeness production. Starting the core of the data taking in November 2002 HERA-B collected about $150 \cdot 10^6$ events with the di-lepton trigger and $210 \cdot 10^6$ events with the interaction trigger until beginning of march 2003. The data were taken in single-wire and double-wire configurations using carbon, titanium, and tungsten targets.

3.7.1 $b\bar{b}$ production cross section

HERA-B measured the $b\bar{b}$ cross section already on the basis of the statistically limited year 2000 data set [abt03]. Until then only two, yet contradicting, measurements of the production cross section in this energy range existed[7] [jan95, ale99].

The analysis was independently performed on the decay channels $b\bar{b} \to J/\psi X \to (e^+e^-/\mu^+\mu^-)X$, and the final cross section was averaged over both results. In order to minimize systematic errors due to detector and trigger efficiencies and not to depend on the absolute luminosity the measurement was done relative to the known prompt J/ψ production cross section. The resulting $b\bar{b}$ cross section is $\sigma_{b\bar{b}} = 32^{+14}_{-12}(\text{stat})^{+6}_{-7}(\text{sys})$ nb/nucleon. Fig. 3.15 shows the HERA-B result

[6] The HERA-II upgrade aims at increasing the luminosity of the collider experiments by a factor of 4.

[7] the fixed target experiments E771 and E789 at a beam energy of 800 GeV.

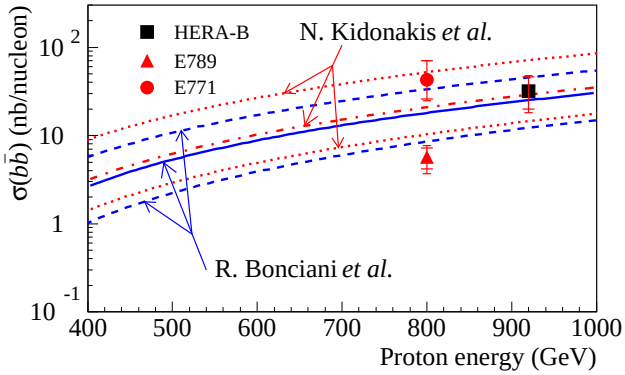

Figure 3.15: Overview of $b\bar{b}$ cross section measurements [abt03] including the result of HERA-B on the year 2000 data set and two theoretical predictions.

together with the other two measurements and two different theoretical predictions [bon98, kid01].

With the accumulated statistics of the 2002/2003 running the collaboration will be able to reduce the statistical error of the 2000 measurement considerably.

3.7.2 Charmonium physics

The HERA-B detector is optimized to trigger on lepton pairs of large invariant mass in the final state. Therefore, it is an ideal device to search for $c\bar{c}$ resonances, since most of them decay into a lepton pair, either directly or by decaying into J/ψ X first. The part of the 2002/2003 data set taken with the di-lepton trigger yields about 300.000 reconstructed J/ψ's, 5.000 $\psi(2S)$, and 15.000 χ_c's [8].

The analyses focus on the following items:

- measurement of J/ψ differential spectra $d\sigma/dx_F$ and $d\sigma/dp_T^2$. Here, HERA-B is the first experiment which provides data in the backward hemisphere ($x_F < 0$).
- measurement of the atomic mass number dependence of the J/ψ production cross section, including a possible dependence on x_F, to study J/ψ suppression in nuclear matter.
- measurement of the $\psi(2S)$ production cross section.
- measurement of the χ_c production cross section.

Concerning the last item a result has already been published based on the year 2000 data set [abt02].

[8] the notation χ_c summarizes the two states χ_{c1} and χ_{c2}, which cannot be distinguished due to the limited detector resolution. As the branching ratio of $\chi_{c0} \to J/\psi\gamma$ is small it does not contribute to the measurement.

3.7.3 Open-charm and strangeness production

Analyses of open-charm or strangeness production concentrate on the interaction trigger sample. An exception is the search for $D^0 \to \mu^+\mu^-$ [ego04], which is performed on the di-lepton trigger data.

The following items are currently under study:

- Measurement of the D^0, $D^{\pm}$, and D^{*+} production cross sections.
- Production cross sections and differential spectra of the strange vector mesons ϕ and K^{*0} including the atomic mass number dependence of the cross sections as a function of p_T^2 and rapidity. While the K^{*0} production is the topic of this thesis, ϕ production is covered in [sym04].
- V^0 production cross sections and differential spectra. A result based on the 2000 data set has been published recently [abt03$^+$].
- Hyperon production including the production of Ξ^-, Ξ^0, and Ω^-.
- Searches for pentaquarks [knö04], and
- the study of Bose-Einstein correlations.

The K^{*0} production, which is in the focus of this analysis, is studied on a subsample of the interaction trigger data. The next chapter deals with the description of the data set, the data selection, and the quality cuts specific to the analysis of the K^{*0} resonance. Afterwards, the extraction of the K^{*0} signal is documented.

Chapter 4

Data selection and signal extraction

An introduction to the data set and data quality checks is given, followed by a description of the Monte-Carlo simulation used. Afterwards we present the selection cuts needed to separate the K^{*0} signal from background. Before the chapter ends with a detailed description of the signal fit a cross check of data and Monte-Carlo simulation is done by means of single track distributions.

4.1 December 2002 data set

After the upgrade of the HERA accelerator in 2001 the re-commissioning of the HERA-B detector was essentially finished in October 2002. In the following period from November 2002 to March 2003 HERA-B took physics data. The data used in this analysis have been recorded in the period of Dec. 7 – Dec. 21, 2002. In nine consecutive proton fills about 130 million inelastic events have been triggered with the interaction trigger. This corresponds to an integrated luminosity of $320\,\mu\mathrm{b}^{-1}$. The data set yields in total about 900.000 reconstructed $K^{*0} \to K^+\pi^-$ and $\bar{K}^{*0} \to K^-\pi^+$, covering a phase space of $2.6 - 4.5$ in rapidity (in the lab frame) and between 0 and $12\,\mathrm{GeV}^2$ in transverse momentum squared.

Most of the data has been taken in single-wire runs using targets of three different materials (C, Ti, W). Additionally, 6 million events have been collected in a two-wire configuration (C+W). However, the systematic uncertainties which are expected from two-wire running led to the decision to exclude these runs from the analysis.

The largest fraction of data is equally shared between the lightest (C) and the heaviest (W) target material available (about 55 million events each), while 20 million events were recorded with the titanium wire, closing the gap in atomic mass number between C and W, which makes this combination of target materials an optimal sample for the study of atomic mass number dependencies. The data statistics of the December 2002 run are summarized target-wise in table 4.1 including the luminosity of each sample, for which a systematic error of 3.5 %

target (material)	no. of runs	no. of events	$\mathcal{L}_{ia}$ [μb^{-1}]	$\mathcal{L}_{rnd}$ [μb^{-1}]
b1 (C)	21	$57.6 \cdot 10^6$	252.2 ± 8.8	1.50 ± 0.05
b2 (Ti)	6	$20.8 \cdot 10^6$	33.7 ± 1.2	0.19 ± 0.01
i1 (W)	14	$52.7 \cdot 10^6$	32.1 ± 1.1	0.16 ± 0.01
Sum	41	$131.1 \cdot 10^6$	318.0 ± 11.1	1.85 ± 0.06

Table 4.1: Summary of the data statistics of the December 2002 running. The integrated luminosities [aus04] accumulated with the interaction trigger and the random trigger are denoted as $\mathcal{L}_{ia}$ and $\mathcal{L}_{rnd}$, respectively. For a detailed list of all runs see appendix C.

has been calculated [aus04]. A comprehensive list of all runs can be found in appendix C.

All runs have been taken at moderate interaction rates of about 1.5 MHz to avoid additional complications due to large track multiplicities and multiple interactions per event. In that way the number of events with two or more simultaneous interactions is limited to about 9 % of the recorded sample.

Apart from the triggered events about 5% of the total statistics has been taken with the random trigger for cross-checks of the interaction trigger performance. Due to the large number of empty events in the random trigger samples the integrated luminosities $\mathcal{L}_{rnd}$ are small. Therefore, this analysis concentrates on the interaction trigger data.

4.1.1 Data quality

Already during data taking the quality of the data has been monitored by looking at the stability of the subdetectors and the quality of the online-reconstructed physics signals (like, e.g., the K^0_S or the J/ψ). In the off-line analysis the data quality criteria are refined to ensure that only runs of reasonable data quality enter the final analyses (see e.g. [con03, zav03]). Within the scope of this thesis special attention was paid on the stability of the K^{*0} signal in all data runs.

Data reprocessing. Based on the various data quality checks performed a refined understanding of the detector performance has been derived, which led to another offline reconstruction of the detector raw data (so-called reprocessing). This analysis is based on reprocessing 4 (repro4) of the data sample. It became available in October 2003. The improvements with respect to the previous reprocessing (repro3) are substantial. The most important ones for this analysis are listed below:

- the ITR is excluded from the reconstruction because it showed unstable performance over a large period of the data taking. As a result detector efficiencies were not properly described by the detector simulation, making efficiency corrections almost impossible.
- the track quality was improved by removing all hits from the track fit which show an unreasonably high residuum (so-called outlier removal).

- Čerenkov angle corrections are introduced for the RICH, which take into account variations of the atmospheric pressure.
- masks and efficiencies for all subdetectors were improved.

Detailed information about all changes can be found in [med03].

Signal stability and mass resolution. To check the stability of the K^{*0} production the signal yield the fitted resonance mass position and the mass resolution have been studied as a function of the data run. All values are derived from fits of the invariant mass distribution of the signal (see section 4.4.2).

Figs. 4.1-4.3 show these three quantities as a function of the run number. The fitted mass is stable among the runs, but shifted by about 5 MeV compared to its nominal value of 896.10 ± 0.27 MeV [hag02]. Whether this effect has a physical origin or is due to alignment problems could not be verified within the scope of this thesis. In the Monte-Carlo, however, both the K^{*0} and the $\bar{K}^{*0}$ appear at the proper mass position.

The fitted mass resolution on data is about 5 MeV, independent of the target material. This is in agreement with what is expected from the Monte-Carlo simulation (see section 4.4.1).

The K^{*0} yield shown in fig. 4.3 is normalized run-wise to the luminosity of each run. Because of the atomic number dependence of the cross section the runs appear separated into bands of the different target materials used. Within the bands the signal yield per run is quite stable. The same stable behavior has been seen for the $\bar{K}^{*0}$ signals. From the point of view of the signal stability all investigated runs are accepted for further analysis.

4.1.2 Monte-Carlo simulation

To correct the data taken with a detector of finite size and performance Monte-Carlo simulations are used. They give a reasonable description of the detector response with respect to inefficiencies, dead channels, and the limited geometrical acceptance. Additionally, they include the best knowledge on the physics of the event, which allows detailed comparisons of the measured data with theoretical and phenomenological expectations. In what follows, the HERA-B Monte-Carlo simulation is briefly introduced and the Monte-Carlo samples used for this analysis are described.

Monte-Carlo generator. The HERA-B event generator consists of two different packages to produce the full physics event and a third one to describe particle decays and the detector response. For generation of the physics event the packages PYTHIA 5.710 [sjö94] and FRITIOF 7.02 [pi92] are used. PYTHIA is optimized for the production of hard processes in proton-proton collisions. In HERA-B it is used to generate heavy-flavor quark pairs. FRITIOF produces only normal inelastic and single-diffractive interactions but takes the nuclear effects in the

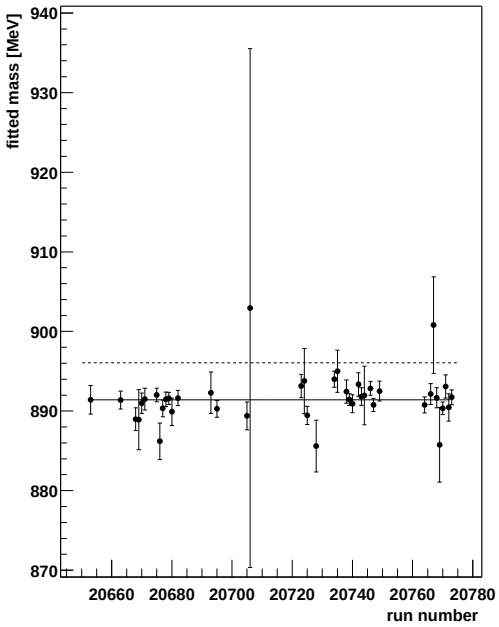

Figure 4.1: Fitted K^{*0} mass for each run. With respect to the nominal value (indicated by the dashed line) the mass is systematically shifted by about 5 MeV to lower values.

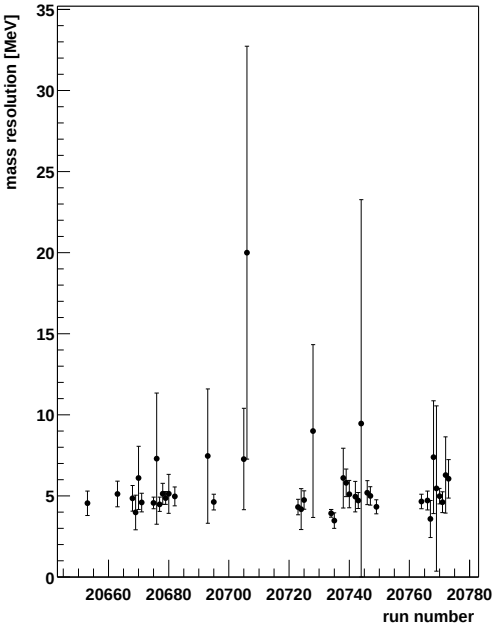

Figure 4.2: Mass resolution for each run as obtained from the signal fits. The resolution is independent of the target material.

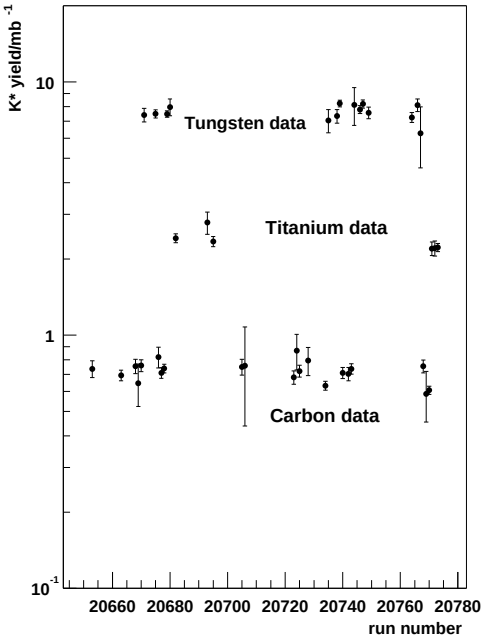

Figure 4.3: K^{*0} signal yield per data run normalized to luminosity. Since the cross section depends on the target material, bands are seen which belong to runs with the same target material.

collision of the proton with the target nucleus into account. A combination of the two generators allows a good description of the real event, simulating first the hard process with PYTHIA and giving the remaining energy to FRITIOF, which produces the underlying event. For the analysis of K^{*0} production a normal inelastic Monte-Carlo based on FRITIOF is sufficient, because no heavy quark production is needed.

The simulation of particle decays and the detector response is done by the package GEANT [gea94]. It propagates the decay products of the inelastic event through the detector and generates so-called impact points on the active detector elements. All electromagnetic and hadronic interactions of the particles with detector matter are handled properly. These include multiple scattering, energy loss through ionization, bremsstrahlung, pair production, and nuclear cascades. The response of the readout electronics is simulated, too, even taking into account electronics noise to a certain extend.

In a Monte-Carlo event the full information on the generated particles and their passage through the detector is stored for later analysis. This information we will call the Monte-Carlo truth, since it is decoupled from the reconstruction. In combination with the reconstructed Monte-Carlo events it is mainly used to estimate the geometrical acceptance of the detector and its reconstruction efficiencies.

Monte-Carlo reconstruction. After having been generated the Monte-Carlo samples are reconstructed by exactly the same reconstruction chain as the real data (outlined in section 3.5). In the hit preparation the Monte-Carlo impact points are translated into hits in the respective subdetectors. The best knowledge on the efficiencies and dead regions of the subdetectors during the data taking period is taken into account. In order to simulate correctly the number of inelastic interactions per event, i.e. the "interaction rate" used to produce the sample, a so-called mixing is applied to the Monte-Carlo:

- From the mean interaction rate of the real data sample the mean number of interactions per bunch crossing $\lambda \equiv \lambda_{mix}$ is calculated using eq. (3.3).
- The generated Monte-Carlo events contain exactly one interaction per event. They are combined such that the number of interactions per event follows a Poisson distribution with expectation value λ_{mix}. In that way also events with two (or more, in very rare cases) interactions are produced.

target	no. of events	mixing parameter λ_{mix}
C	$4.6 \cdot 10^6$	0.1675
Ti	$1.9 \cdot 10^6$	0.1711
W	$3.8 \cdot 10^6$	0.1250
Sum	$14.5 \cdot 10^6$	

Table 4.2: Summary of the Monte-Carlo statistics used for this analysis and the mixing parameters λ_{mix} used to simulate the proper interaction rate (see text).

For each target material a separate Monte-Carlo sample has been generated and reconstructed. The Monte-Carlo statistics is summarized in table 4.2 together with the mixing parameters λ_{mix}.

Monte-Carlo track matching. For many studies performed in this analysis the Monte-Carlo is treated like being real data, i.e. the Monte-Carlo truth information is not used. For some studies like track-based comparisons a direct relation between a generated particle and its reconstructed track is needed. This is provided by a mechanism called Monte-Carlo track matching. The method [hul02] tries to match the detector hits used for the track reconstruction to the Monte-Carlo impact points of the generated particle. If more than 70 % of the track hits match on those impact points, track and particle are identified with each other. In this way all properties of the generated particle become available on track level.
Studies of the Monte-Carlo track matching have shown that its efficiency is only about 80 %, slightly depending on the investigated kinematic region. Hence, it cannot be used in any kind of efficiency study but is a valuable tool e.g. in track-based comparisons of generated and reconstructed Monte-Carlo.

In the next section we will use the Monte-Carlo simulation to estimate the efficiencies of the data selection cuts. Whenever possible we will compare those numbers to efficiencies directly obtained from data and will find both numbers to be well in agreement.

4.2 Data selection

The following sections document the selection cuts that are applied to the data sample to get a clean and significant K^{*0} signal[1]. First, all events undergo a soft event selection and vertex reconstruction, before kaon identification and track quality cuts are applied, which provide a powerful rejection of combinatorial background. The values of the kaon identification and VDS track quality cuts are based on the special properties of the particle identification algorithm and the vertex detector geometry. The Outer Tracker quality cuts, however, can in principle be chosen freely within a wide range of reasonable values. These cuts are optimized by looking at the signal peak and the background contribution in the $K^+\pi^-$ invariant mass distribution. The goal is to arrive at a most prominent K^{*0} signal above background. Quantitatively this is described by the significance of the signal, defined as

$$\Sigma := \frac{S}{\sqrt{S+B}}, \tag{4.1}$$

where S is the signal yield taken from the Monte-Carlo simulation and B the integrated background under the invariant mass peak of the signal derived from real data. In this way we are sure that the signal on real data is not artificially grown and that a realistic background is taken into account. Signal yield and

[1] note, that although all optimizations are based on the K^{*0} signal they are also valid for the $\bar{K}^{*0}$. Hence, the analysis cuts applied to the K^{*0} and the $\bar{K}^{*0}$ are the same.

background are evaluated from fits to the respective invariant mass distributions on data and Monte-Carlo (details on the signal fit are presented in section 4.4).

Before we explain the various cuts in detail we want to demonstrate the impact

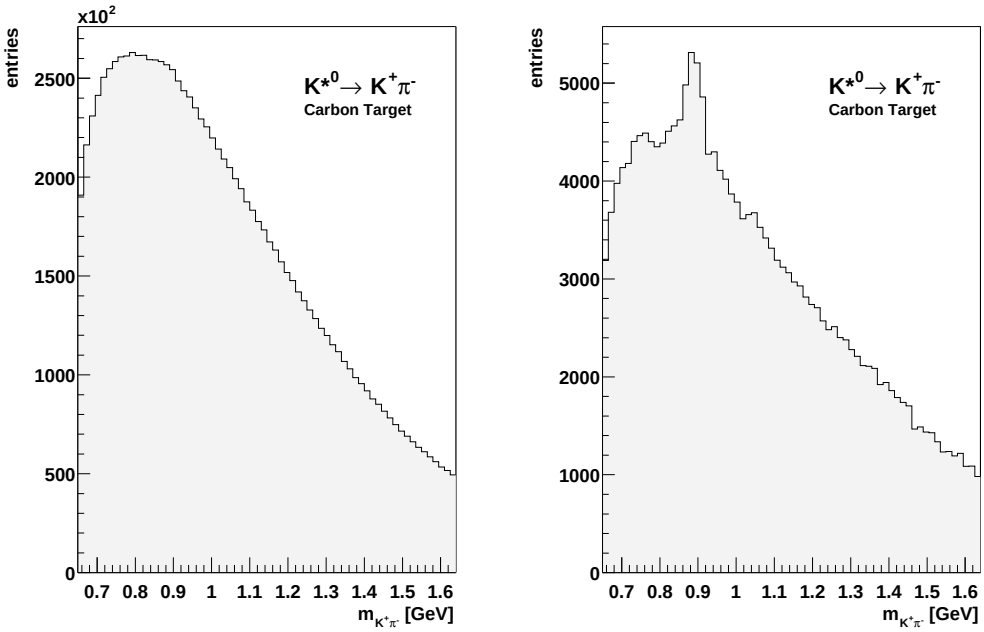

Figure 4.4: Invariant $K^+\pi^-$ mass distributions in the region of the nominal K^{*0} mass. *Left:* Only event selection and vertex reconstruction applied. The K^{*0} signal is hidden by large combinatorial background. *Right:* After application of all selection cuts the background is reduced by a factor of about 60 and the K^{*0} signal is clearly visible.

of the final cuts on the invariant mass distribution. This is seen in fig. 4.4 showing a $K^+\pi^-$ invariant mass distributions derived from about 1.5 million events produced on the carbon target. On the left side only the soft event selection and vertex reconstruction are applied to the data. No signal is seen but only a large amount of combinatorial background. The right side of the figure shows the same data after all selection cuts are applied. A prominent K^{*0} peak shows up and the combinatorial background is reduced by a factor of about 60.

In the following, we will describe the various selection cuts in the order in which they are applied to the data. In evaluating cut efficiencies we will basically restrict ourselves on the carbon data sample, since in comparing different target materials we have found no evidence of an influence of the target material on the efficiency of the cuts. A summary table of all selection cuts can be found on page 64.

4.2.1 Event selection

As a pre-selection step only events triggered by the interaction trigger are accepted for analysis. Additionally, at least two tracks of opposite charge are required

in each event. Each track consists of at least 5 hits in the VDS and 10 hits in the Outer Tracker to ensure that only long tracks are selected. No special demand for a primary vertex is made.

From the $131.1 \cdot 10^6$ events considered for the analysis $97.2 \cdot 10^6$ survive the event

	C	Ti	W
all events	57.589.095	20.832.361	52.722.458
IA trigger	55.010.390 (95.5%)	19.953.151 (95.8%)	50.595.393 (96.0%)
≥ 1 track	45.563.677 (82.8%)	16.494.531 (82.7%)	42.742.572 (84.5%)
≥ 2 tracks	41.264.982 (90.6%)	15.310.412 (92.8%)	40.662.031 (95.1%)
total eff.	(71.7%)	(73.5%)	(77.1%)

Table 4.3: Event numbers before and after the event selection for the different target materials. The efficiencies with respect to the previous selection step are given in brackets, and the total efficiency is summed up in the last row.

selection. The numbers and the corresponding selection efficiencies are given in table 4.3 separately for each target material. About 4 % of the events are rejected because they were taken with the random trigger. The reconstruction of at least 2 tracks contributes with an additional inefficiency of about 20-25 %, which decreases with the atomic mass number A of the target material. This effect is probably due to the track multiplicity, which increases with the atomic mass number A like $A^{0.20\pm0.02}$ [bas02].

4.2.2 Vertex reconstruction

For each selected event all possible combinations of oppositely charged track pairs are subject to a stand-alone vertex reconstruction. The vertex fit is done by the package vt++ [loh95, gle00] using the track parameters (offsets, slopes, and momenta) and the covariance matrices of the track fits as an input. If the fit succeeds the invariant mass $m_{K\pi}$ of the track pair is calculated separately for the combinations $K^+\pi^-$ and $K^-\pi^+$. In the first case the positive (negative) track is assigned the kaon (pion) mass to look for the decay $K^{*0} \rightarrow K^+\pi^-$. In the second case the mass assignment is flipped as to look for $\bar{K}^{*0} \rightarrow K^-\pi^+$. A track combination is accepted for analysis, if $0.63\,\mathrm{GeV} \leq m_{K\pi} \leq 1.6\,\mathrm{GeV}$.

Apart from a successful vertex reconstruction and the invariant mass constraint no further vertex quality cuts are applied, since cuts on e.g. the distance between the target wire and the vertex are not successful to further increase the significance of the signal.

4.2.3 Particle Identification

With only event selection and vertex reconstruction applied the invariant mass distribution is dominated by combinatorial background, making an observation of the signal impossible (cf. fig. 4.4). Hence, we apply a kaon identification cut to reduce the number of track-pair combinations. Kaon candidate tracks are

identified by the HERA-B RICH (see section 3.3.4) using a track-based particle identification approach [pes01]. Before we discuss the value and efficiency of the cut used in this analysis we will shortly introduce the algorithm.

Kaon identification algorithm. For each track traversing the RICH the algorithm calculates a set of likelihoods λ_j for five particle hypotheses, with $j \in \{e, \mu, \pi, K, p\}$. A 6th likelihood, λ_{bg}, estimates the probability of a background hypothesis. The sum of all likelihoods is normalized to 1. The likelihood represents a measure of the probability that the track can be identified with a certain particle. It is deduced from the Čerenkov angles of photons associated with the track and from the Čerenkov thresholds of the different particles using the momentum information of the track. The following is a simplified sketch of the likelihood evaluation:

1. The positions of the Čerenkov photons are measured on the RICH photon detector planes. For each track-photon pair the algorithm calculates the Čerenkov angle θ_c of the photon with respect to the track. All unphysical combinations, that is pairs with $\theta_c \geq \theta_c^{max}$, are discarded[2]. In this way a set of i Čerenkov angles $\theta_c^{(i)}$ is derived for each track.

2. Knowing the momentum of the track a hypothetical Čerenkov angle θ_c^{hyp} can be calculated for each of the five particle hypotheses s. With this information six probability density functions $f(\theta_c^{(i)}|s_j)$ can be constructed, which give the probability that the set of measured Čerenkov angles is consistent with the particle hypothesis s_j (or consistent with being background photons). s_j is a function of the particle mass.

3. The probabilities are combined to a common likelihood function L, which is basically the product of all probability density functions. The likelihoods λ_j for the different particle hypotheses s_j are then calculated as $\lambda_j = L(s_j)$. In that way a particle hypothesis associated to a certain track is the more likely the higher its likelihood value is.

4. If no Čerenkov photons could be associated to the track, its momentum is probably below the Čerenkov threshold of the particle. In that case all particle hypotheses which are compatible with this observation get equal likelihood values[3]. A non-radiating track with a momentum below the kaon but above the pion threshold, e.g., can either be a proton, a kaon, or a fake track (and therefore background). Thus, $\lambda_p = \lambda_K = \lambda_{bg} = 1/3$. For $\lambda_K > 1/3$ the kaon is above the Čerenkov threshold and hence can be positively identified.

Cut evaluation. Fig. 4.5 shows a Monte-Carlo distribution of the kaon likelihood λ_K. The shaded histogram corresponds to reconstructed tracks matched on kaons

[2] $\theta_c^{max} = 51.5$ mrad the Čerenkov angle of a $\beta = 1$ particle (see section 3.3.4).

[3] note, that even though the production ratios of the different particles are a priori known from other measurements they do not enter the likelihood calculation.

in Monte-Carlo truth, and the white histogram represents all tracks. Prominent peaks are seen which correspond to tracks with momenta below the Čerenkov thresholds of muons ($\lambda_K = 1/5$), pions ($\lambda_K = 1/4$), and kaons ($\lambda_K = 1/3$).

For $\lambda_K \leq 1/3$ the kaons do not radiate, therefore the distribution is dominated by other particles (mostly pions). Above $\lambda_K = 1/3$ their contribution is reduced significantly, because the kaons are positively identified by the Čerenkov angle measurement. Only a small fraction of mis-identified tracks (mostly pions) is seen between $1/3 < \lambda_K < 0.9$. To reject also these tracks a likelihood cut of $\lambda_K \geq 0.95$ is chosen in this analysis.

For all accepted kaon candidate tracks the likelihood cut introduces an intrinsic

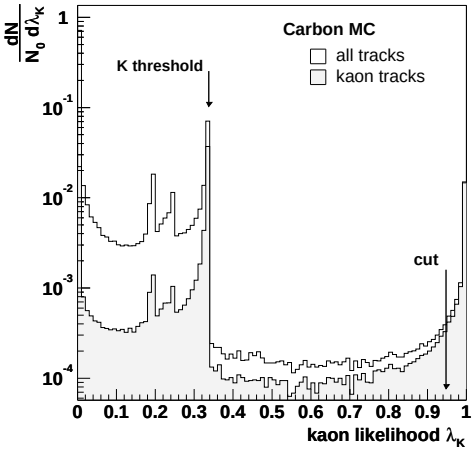

Figure 4.5: Distribution of the kaon likelihood λ_K for reconstructed (and matched) kaons and for all tracks. The Čerenkov threshold for kaons corresponds to $\lambda_K = 1/3$ (see text). The kaon identification cut used in this analysis is $\lambda_K \geq 0.95$.

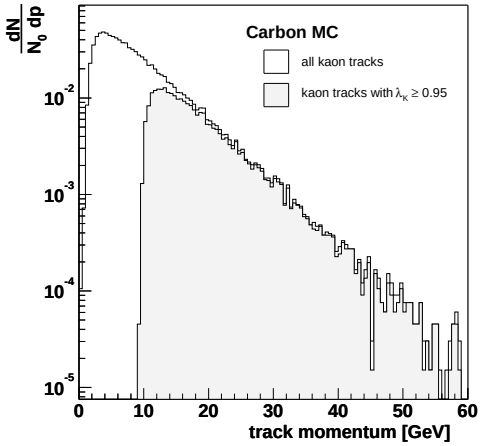

Figure 4.6: Momentum distribution of reconstructed (and matched) kaons. The shaded histogram shows tracks with a kaon likelihood $\lambda_K \geq 0.95$. The intrinsic momentum cut at 9.6 GeV is clearly visible.

momentum cut of about 9.6 GeV, which is the kaon Čerenkov threshold. This effect can be seen in fig. 4.6, showing matched kaon tracks with and without a likelihood cut of $\lambda_K \geq 0.95$. Due to the momentum cut about 74% of all kaons are lost. Above the threshold, however, the kaons are well identified.

Efficiency. The kaon identification efficiency has been determined [ari04, sta04] both on real data and on Monte-Carlo using $\phi \to K^+K^-$ decays. The ϕ signal is already observed with only one of its kaon daughter tracks identified by the RICH. Its yield is determined by a fit to the invariant K^+K^- distribution. In a second step a positive kaon identification is demanded for the second daughter track, too, and once again the ϕ yield is determined. The ratio of the yields is an estimate of the kaon identification efficiency.

The efficiency determined in this way is shown as a function of the kaon momentum in fig. 4.7. Between 10 GeV and 40 GeV the efficiency is about 90% on

Monte-Carlo and about 85% on data. The difference is most probably due to additional background photons in real data, which are not properly taken into account by the simulation. Above 40 GeV the Čerenkov angles of kaons and pions become indistinguishable. Hence, some of the kaons are identified as pions and the efficiency drops. At the same time the pion mis-identification probability, shown in fig. 4.8, goes up. However, due to the exponential fall-off of the kaon momentum distribution (cf. fig. 4.6) most momenta are in the order of 10-20 GeV. In this region the pion mis-identification probability is well below 5%, i.e. a large amount of the pion background is cut away.

Even though the kaon identification efficiency is quite high for track momenta above 10 GeV the implicit momentum cut rejects a large fraction of possible K^{*0} candidates from the low-momentum part of the K^{*0} spectrum. Based on the Monte-Carlo track matching method the total efficiency of the kaon identification cut can be estimated as being about 15 % only.

In this analysis the kaon identification efficiencies were taken from the Monte-Carlo simulation. The main reason is that in this case possible correlations with other cuts are correctly taken into account. The efficiency difference between Monte-Carlo and data will be used as a systematic error on the cross section measurement (see section 6.1.2).

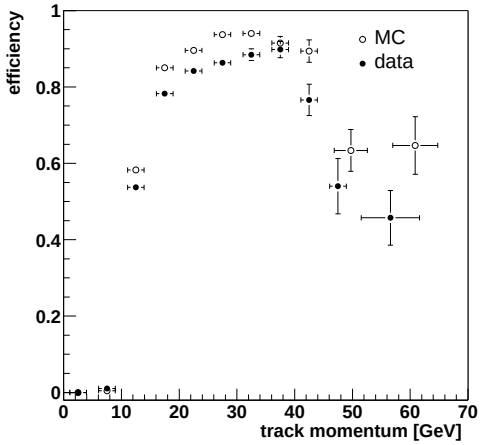

Figure 4.7: Kaon efficiency derived from $\phi \to K^+K^-$ decays for real data and Monte-Carlo. The kaon threshold at 9.6 GeV is clearly visible. Based on [sta04].

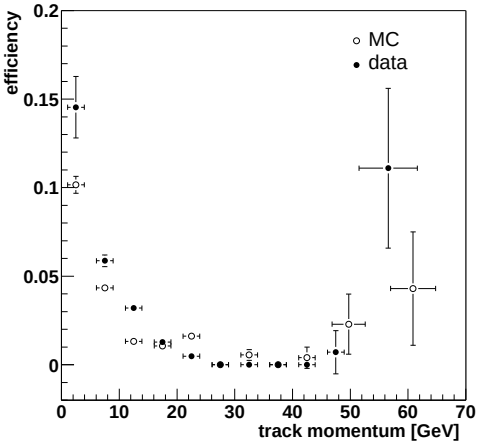

Figure 4.8: Efficiency to mis-identify a true pion as a kaon, derived from $K^0_S \to \pi^+\pi^-$ decays (both for Monte-Carlo and real data). Based on [sta04].

4.2.4 Track selection

By applying cuts on the track quality and on the momentum of the pion candidate track the significance of the K^{*0} signal can be improved further. The cut optimization is done on the carbon data sample in the channel $K^{*0} \to K^+\pi^-$ and is adopted to the other samples.

Track hits. In principle one out of three different quality cuts can be applied to select a sample of well-reconstructed tracks:

- a cut on the χ^2 probability of the track fit,
- a cut on the χ^2 probability of the segment matching fit, which describes how well the track segments in front and behind the magnet could be combined into a common track (see section 3.5),
- a cut on the minimum number of hits the track is built of.

The three quantities are correlated to a large extend. Hence only one of them should be cut on. In this analysis the track selection follows the third method, which is separately applicable in the Vertex Detector and the Outer Tracker, because the hit information is accessible on the subsystem level.

Concerning the VDS we demand at least 6 hits per track in this subsystem. Since a superlayer of the VDS comprises four layers of strips a track segment with four hits can by chance consist of only hits in a single superlayer. The slopes of such segments will be badly resolved. With a cut on 6 hits/track we also reject those segments which contain an additional noise hit in one of the other superlayers.

However, this cut is a very soft one. It does not increase the significance of the K^{*0} signal but only ensures that the Vertex Detector track segment is of reasonable quality. From the Monte-Carlo simulation an efficiency of $\epsilon^{mc}_{hVDS} = 0.99 \pm 0.03$ is obtained, which is in agreement with the value found on data, 1.00 ± 0.01. In the following the cut is applied to the data.

The cut on the number of hits/track in the Outer Tracker has been optimized with respect to the significance of the K^{*0} signal. Figure 4.9 shows the result of the optimization on the carbon target data. The significance Σ increases up to a plateau at 15-22 hits/track and drops down for larger values. The rise with increasing number of hits is due to a cut-down of background from poor quality tracks, while the decrease above 22 hits/track is only statistical. A cut of at least 18 hits/track has been chosen as a compromise between background reduction and keeping the signal.

The efficiency of the cut is shown in fig. 4.9 as a function of the cut value. It is determined separately in Monte-Carlo and data. The efficiency is normalized to the efficiency when requiring 10 hits per track, which is the lower limit given by the event selection. For the chosen cut the efficiency obtained from the Monte-Carlo is $\epsilon^{mc}_{hOTR} = 0.95 \pm 0.03$, which is in perfect agreement with the value determined from real data (0.95 ± 0.01). At the same time the background below the signal peak is reduced by 13 %.

Track momentum. The significance of the K^{*0} signal can be further enhanced by removing low momentum tracks. This concerns only the pion candidate tracks, since the kaon momentum is intrinsically above 9.6 GeV due to the kaon identification cut. Again, the cut has been optimized with respect to the significance of the signal. The result is presented in fig. 4.10 for pion momenta up to 5 GeV,

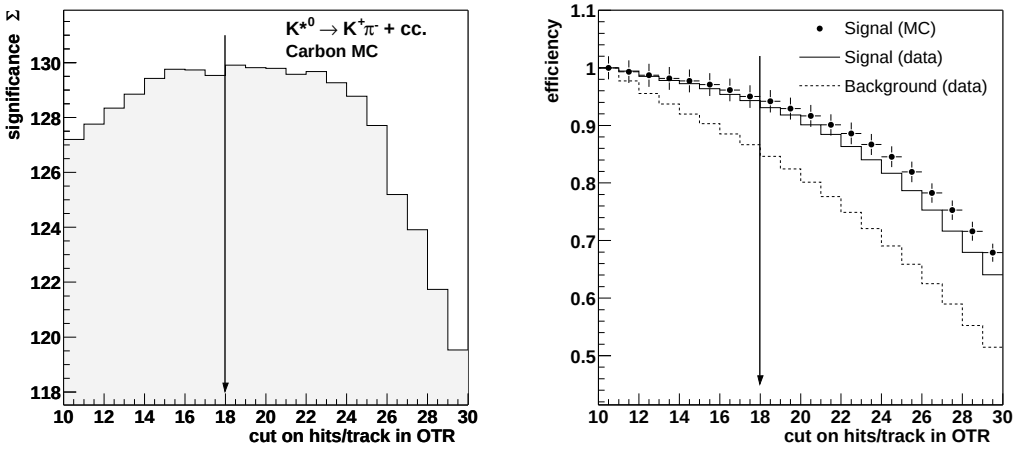

Figure 4.9: *Left:* K^{*0} signal significance as a function of the cut on the number of hits in the outer tracker. The signal yield used to calculate the significance is derived from the Monte-Carlo simulation, the background comes from real data. The cut of at least 18 hits/track chosen for this analysis is indicated by the arrow. *Right:* Efficiencies of signal and background as a function of the cut. The data points represent the signal efficiencies obtained from the Monte-Carlo simulation. Both plots are based on the carbon data sample.

showing that a cut of 1.8 GeV is optimum. For the final analysis the cut has been increased to 2 GeV. This further reduces the combinatorial background on the left side of the K^{*0} signal region, which is in favor of a stable background description in the mass fits.

The efficiency for this cut, as obtained from the Monte-Carlo simulation, is $\epsilon^{mc}_{P_\pi} = 0.97 \pm 0.02$. This is again in perfect agreement with the value determined directly from data (0.97 ± 0.01). The background reduction is 17.4 %.

4.2.5 Summary of the data selection cuts

Within the last sections we have presented the data selection procedure used to obtain a clean K^{*0} signal peak above background. About 70-77 % of all events survive the soft event selection criteria, depending on the target material. The main inefficiency in this context arises from the track reconstruction.

Candidate track pairs reconstructed in the remaining events have undergone a track selection (for a summary of all track selection cuts see table 4.4). The kaon identification cut turns out to be most important with respect to the signal optimization, since it cuts away most of the combinatorial background. On the other hand, as the identification procedure introduces an indirect 9.6 GeV momentum cut on the kaon track, only about 15 % of the K^{*0} decays survive the kaon identification.

Whenever possible we have compared the efficiencies of the various cuts on data

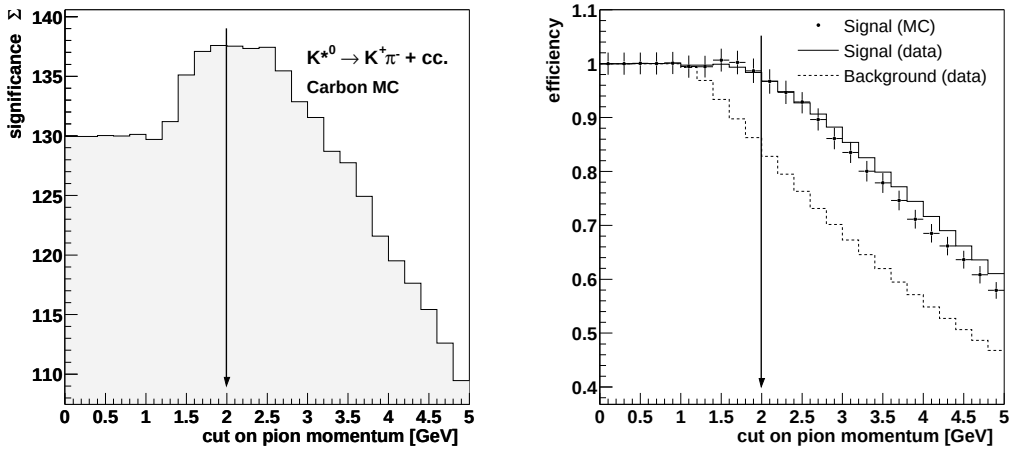

Figure 4.10: *Left:* Signal significance for carbon data as a function of the cut on the momentum of the pion candidate track. *Right:* Efficiencies of signal and background as a function of the cut. The dots with the error bars represent the signal efficiencies obtained from the Monte-Carlo.

description	cut	efficiency
kaon identification	$\lambda_K \geq 0.95$	≈ 0.15
track quality (VDS)	hits/track$\geq$ 6	0.99 ± 0.03
track quality (OTR)	hits/track$\geq$ 18	0.95 ± 0.03
pion track momentum	$p_\pi \geq 2\,\mathrm{GeV}$	0.97 ± 0.02

Table 4.4: Summary of the track selection cuts introduced in this section.

and Monte-Carlo and have found them to agree well. Therefore, we are convinced that the detector response is reasonably described by the Monte-Carlo simulation. Within the next section we will briefly compare single track distributions to further support this conclusion.

4.3 Single track distributions

For a correct simulation of the detector acceptance and the reconstruction efficiency a reasonable agreement between data and Monte-Carlo already at the level of single tracks is important. To cross-check the level of accuracy of the Monte-Carlo predictions we will therefore compare distributions of several track parameters for data and Monte-Carlo.

We are particularly interested in daughter tracks of K^{*0} decays. Those are, however, hardly selectable on data, because the K^{*0} signal is accompanied by a large combinatorial background (see fig. 4.4). Therefore, this study relies completely on background tracks. A similar but more extensive study has been performed on the year 2000 data set [hul02].

The comparison is made on tracks which passed the event selection and track selection cuts described in section 4.2.4. However, no kaon identification was applied in these studies. All distributions are based on the carbon data sample and are normalized to the same number of entries.

In fig. 4.11 momentum distributions of single tracks in data and Monte-Carlo are compared. The plot shows the the ratio Q/p, Q being the charge of the track and p its momentum. The momentum cut of 2 GeV applied in the track selection (section 4.2.4) and the kinematic limit at high momenta ($Q/p \to 0$) are clearly visible. Data and Monte-Carlo are in good agreement.

What concerns the distributions of the scattering angle θ (given in the lab frame) the agreement between real data and Monte-Carlo is reasonable, too, as is shown in fig. 4.12. The edge of the geometrical acceptance in the vertical plane is nicely reflected by a kink at $\theta = 160$ mrad.

Small deviations between Monte-Carlo and data are seen in the azimuthal track distributions, which are shown in fig. 4.13 as a function of the angle ϕ [4]. The bending of the tracks by the HERA-B magnet is nicely seen, as tracks of positive and negative charge are bent towards the positive and negative x-direction, respectively. The Monte-Carlo simulation overshoots the data in the horizontal plane ($\phi \approx 160°$ and $\phi \approx 340°$), which is most probably due to differences in the kinematic distributions in data and in the Monte-Carlo simulation.

Our study of single track distributions shows that in general the agreement between real data and Monte-Carlo can be considered reasonable. To arrive at a better agreement in the azimuthal distributions detailed studies of the kinematic

[4] within the HERA-B coordinate system $\phi = 180°$ coincides with the positive x-axis and $\phi = 270°$ points towards the positive y-axis.

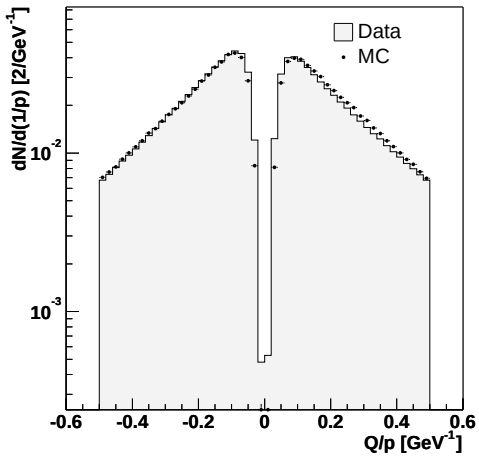

Figure 4.11: Q/p distribution for single tracks normalized to the same number of entries. The momentum cut at 2 GeV is clearly seen.

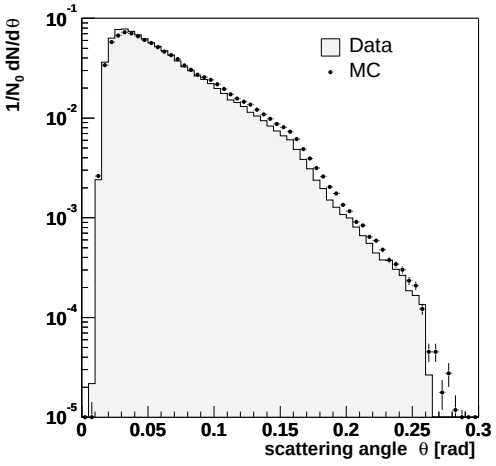

Figure 4.12: Comparison of the scattering angle θ of single tracks measured in the laboratory system. The kink at θ = 160 mrad is a result of the different acceptance limits in the horizontal and vertical plane.

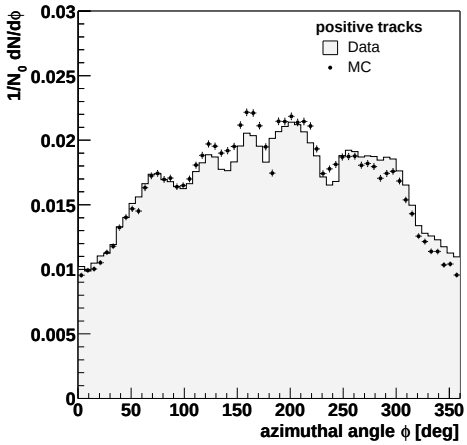

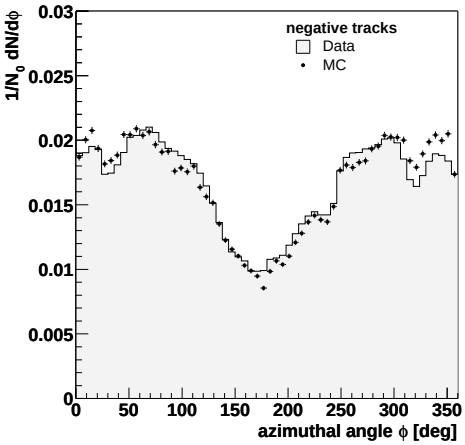

Figure 4.13: Distribution of the azimuthal track angle. The bending of the tracks in the magnetic field is clearly visible. All distributions are normalized to the same number of entries.

properties of Monte-Carlo generated particles would be needed, but these are beyond the scope of this thesis. In comparing the p_T^2 and rapidity distributions of the K^{*0} for data and Monte-Carlo we will however see that the Monte-Carlo needs a careful reweighting of its p_T^2 distributions in order to describe the data properly (cf. section 5.3.1).

4.4 K^{*0} reconstruction

After having applied the quality cuts described in section 4.2 the signal is still governed by large combinatorial background (cf. fig. 4.4). To yield the correct number of K^{*0} a proper fit to the invariant mass distribution plays an important role in the analysis.

Before describing the signal fit in detail we estimate the K^{*0} mass resolution of the spectrometer from the Monte-Carlo simulation, which is a necessary preparation for the further analysis.

4.4.1 Mass resolution

The dominating contribution to the mass resolution comes from uncertainties in the momentum measurement of the K^{*0} daughter tracks (both absolute momentum and opening angle). The momentum resolution itself is a function of momentum and of the quality of the track reconstruction. In that way the mass resolution does not only depend on the physics process investigated, but also on the data selection cuts.

In this analysis knowledge on the mass resolution is of importance for the choice of the binning of the invariant mass distributions and for an adequate signal fit. To avoid migrations among neighbored bins of the invariant mass distribution the bin size should be chosen much larger than the mass resolution σ_m. Furthermore, the shape of the resonance signal does depend on the size of the resolution with respect to the natural width $\Gamma_{K^{*0}}$ of the resonance. In principle three scenarios are possible:

- The mass resolution is negligible compared to the natural width, i.e. $\sigma_m \ll \Gamma_{K^{*0}}$. In this case the signal shape is given by a Breit-Wigner function [jac64].
- The width of the signal is dominated by the mass resolution, $\sigma_m \gg \Gamma_{K^{*0}}$, which usually allows to describe the signal by a Gaussian function of width σ_m.
- Mass resolution and natural width are of comparable size. In this case the Breit-Wigner should be convoluted by a Gaussian resolution function.

We estimate the mass resolution on Monte-Carlo by looking at residuals between the K^{*0} invariant mass obtained from the momentum information of the daughter particles at generator level and from the reconstructed daughter tracks:

$$\Delta M = m_{K\pi}^{reco} - m_{K\pi}^{true}. \tag{4.2}$$

For this track-wise comparison we make use of the Monte-Carlo matching relation between the generated particles and reconstructed tracks (cf. section 4.1.2).

The residual distributions for the three target materials are shown in fig. 4.14, exemplary on the channel $K^{*0} \to K^+\pi^-$. They are fit on an empirical basis by the

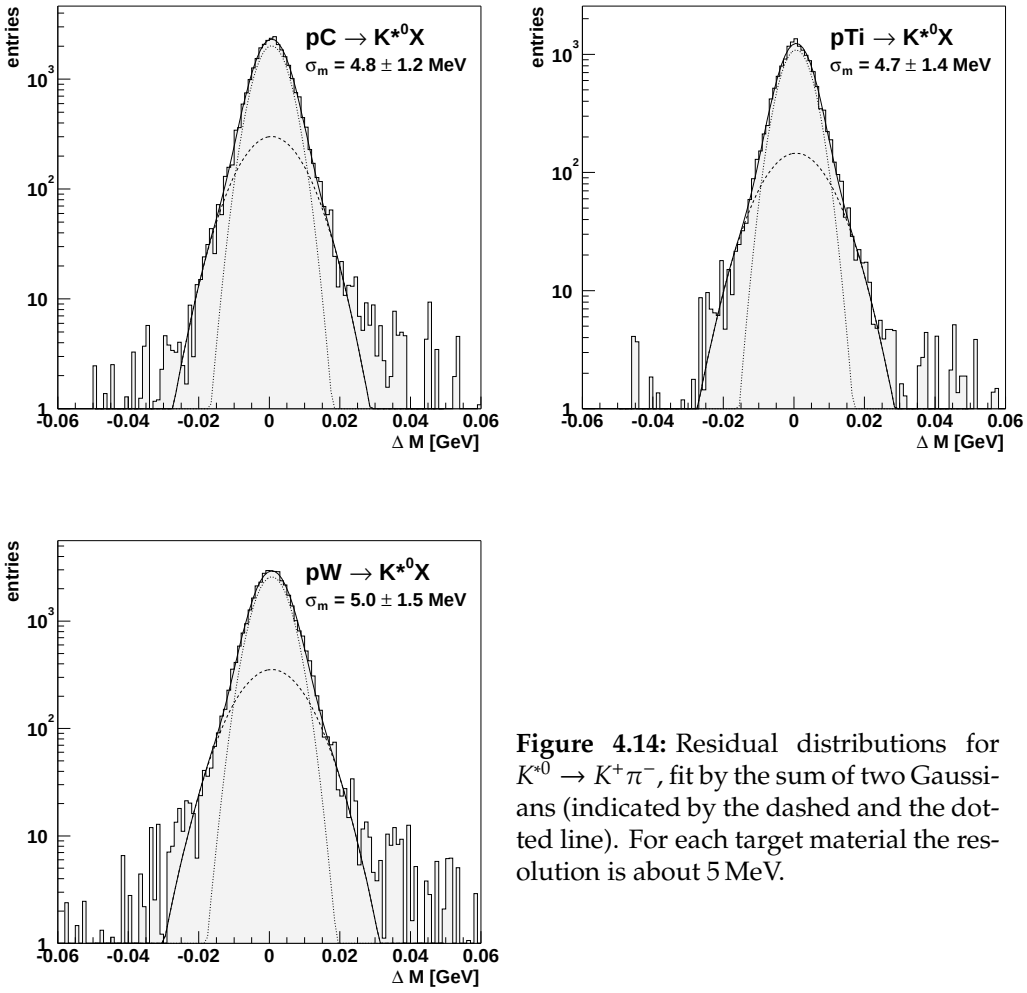

Figure 4.14: Residual distributions for $K^{*0} \to K^+\pi^-$, fit by the sum of two Gaussians (indicated by the dashed and the dotted line). For each target material the resolution is about 5 MeV.

sum of two Gaussians with the same mean. The joint width of this sum,

$$\sigma_{\mathrm{m}} = \sqrt{\frac{I_1\sigma_1^2 + I_2\sigma_2^2}{I_1 + I_2}}, \tag{4.3}$$

is used as an estimate of the mass resolution. Here, σ_1, σ_2 are the widths, and I_1, I_2 the integrals of the two Gaussians. The fit was performed in a ±50 MeV interval.

Table 4.5 summarizes the mass resolutions obtained on the different target materials, separately for the K^{*0} and the $\bar{K}^{*0}$. Within errors they agree perfectly well

$K^{*0} \to K^+\pi^-$	σ_m [MeV]	χ^2/n.d.f.
C	4.8 ± 1.2	3.5
Ti	4.7 ± 1.3	2.5
W	5.0 ± 1.5	5.1
$\bar{K}^{*0} \to K^-\pi^+$		
C	4.7 ± 1.2	2.9
Ti	4.9 ± 2.3	2.2
W	4.8 ± 1.3	4.2

Table 4.5: Mass resolutions and χ^2/n.d.f. obtained from Monte-Carlo. For the different materials the values are in perfect agreement.

with each other, $\langle\sigma_m\rangle \approx 4.8\,\text{MeV}$. Note that the fit does not correctly describe the most outer parts of the residual distribution, which results in a χ^2/n.d.f. of the fit between 2-5. They could have probably been taken into account by adding a third Gaussian. However, the result is not expected to change much since the statistics in the tails is very small and there are no far outliers.

Based on the mass resolution obtained we conclude:

- the bin size of the invariant mass distributions should be chosen well above 5 MeV to avoid migration effects.
- Compared to the natural width of the K^{*0}, $\Gamma_{K^{*0}} = 50.5 \pm 0.6\,\text{MeV}$ (FWHM[5]), the mass resolution is significantly smaller but of the same order, $\sigma_m^{(FWHM)} \approx 0.2\ \Gamma_{K^{*0}}$. This means that the signal can be described by a Breit-Wigner function, but the finite resolution must be taken into account. Therefore, we will convolute the Breit-Wigner with a Gaussian resolution function.

Details on the invariant mass fit are explained in the following section.

4.4.2 Invariant mass fit

In this section we document the invariant mass fit used to obtain the K^{*0} yield. We present the parameterizations used to describe the signal and the underlying background and study the various contributions to the background shape.

All invariant mass distributions cover a mass range of 0.65-1.64 GeV and consist of 66 bins of 15 MeV width. The bin width is chosen well above the mass resolution estimated in the last section. In that way we are sure that no significant bin-to-bin migrations appear.

The invariant mass distributions are fit by the sum of a Breit-Wigner convoluted with a Gaussian, and a background term. The fit is performed in the range $0.66\,\text{GeV} \leq m \leq 1.2\,\text{GeV}$ starting near the kinematic $K\pi$ threshold. To obtain the K^{*0} yield the signal function (without the background) is integrated in a

[5] full width at half maximum. For a Gaussian distribution, 1 FWHM corresponds to 2.354 σ.

$\pm 3\,\Gamma_{K^{*0}}$ range around the fitted resonance mass. The choice of the fit boundaries is arbitrary in a wide range, since once the acceptance corrections are applied they will compensate a possible influence of the boundaries on the signal yield, because the same method of fitting is applied there (see section 5.3).

Fig. 4.15 shows invariant mass distributions for the data statistics used in this analysis, integrated over the full acceptance. All selection cuts described in section 4.2 have been applied. In total about 520.000 $K^{*0} \to K^+\pi^-$ decays and 400.000 $\bar{K}^{*0} \to K^-\pi^+$ decays have been reconstructed. The yields obtained from the different materials can be seen from the plots.

As has already been observed in section 4.1.1, the fitted resonance mass is shifted by about 5 MeV to the left with respect to the nominal value of 896 MeV. The

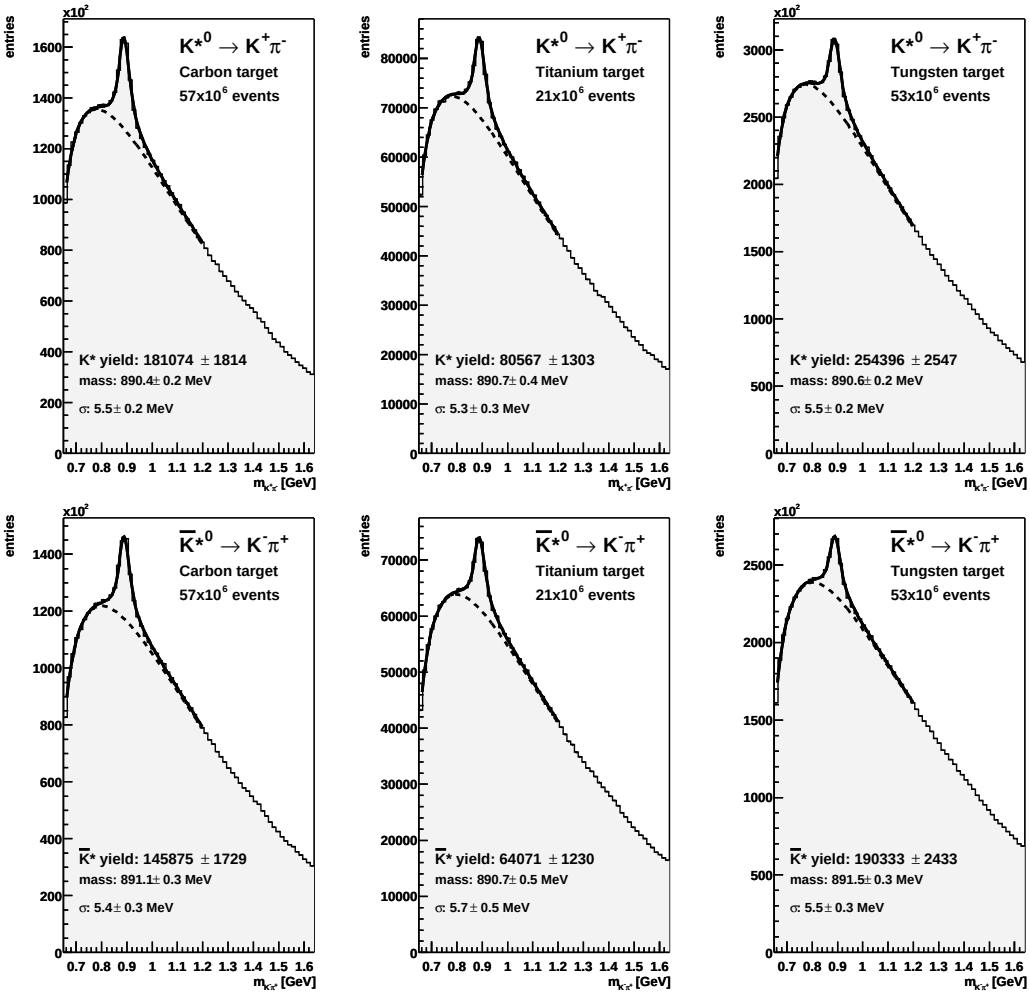

Figure 4.15: Invariant mass spectra for the complete data statistics integrated over the full acceptance. The distributions are fit by the sum of a Breit-Wigner function convoluted with a Gaussian and a background term, which is indicated by the dashed line. In total, about 520.000 $K^{*0} \to K^+\pi^-$ and 400.000 $\bar{K}^{*0} \to K^-\pi^+$ have been reconstructed.

mass resolution for all materials is about 5.5 MeV, roughly 10 % larger than the

resolutions estimated from the Monte-Carlo simulation in section 4.4.1, but within the statistical errors still compatible with them.

Signal description on real data. The Breit-Wigner function describing the signal shape is given by

$$BW(m) = \frac{m \cdot m_0 \cdot \Gamma(m)}{(m_0^2 - m^2)^2 + (m_0 \cdot \Gamma(m))^2}\,, \tag{4.4}$$

following the definition used in [agu91]. m_0 is the resonance mass obtained by the fit and $\Gamma(m)$ is defined as

$$\Gamma(m) = \Gamma_0 \cdot \left(\frac{q}{q_0}\right)^{2l+1} \cdot \frac{m_0}{m}, \tag{4.5}$$

where $\Gamma_0 \equiv \Gamma(m_0)$ is the natural width of the K^{*0}. l is the relative angular momentum of the decay products. Since the K^{*0} is a vector meson decaying into two pseudo-scalar mesons, $l = 1$.

The momentum transfer q to each decay particle in the center-of-mass system is given by

$$q = q(m) = \frac{\sqrt{(m^2 - (m_K + m_\pi)^2)(m^2 - (m_K - m_\pi)^2)}}{2m}\,, \tag{4.6}$$

and q_0 is defined as $q_0 \equiv q(m_0)$.

To account for the finite mass resolution the Breit-Wigner function is numerically convoluted with a Gaussian. In doing so, the natural width Γ_0 of the K^{*0} is fixed to its nominal value, $\Gamma_0 = \Gamma_{K^{*0}} = 50.5\,\mathrm{MeV}$. The mass resolution σ_m and the mass position are free parameters of the fit.

Signal shape in Monte-Carlo. The K^{*0} signal form generated in the Monte-Carlo simulation is not described by eq. (4.4) but by a so-called non-relativistic Breit-Wigner function:

$$BW_{nonrel}(m) = \frac{\Gamma_0/4}{(m_0 - m)^2 + \Gamma_0^2/4}. \tag{4.7}$$

The reason is that (4.7) can be easier derived from uniformly distributed random numbers. The difference in shape compared to eq. (4.4) is sizable. Therefore, fits to invariant mass distribution from Monte-Carlo are performed using function (4.7). Again the function is convoluted with a Gaussian to take the mass resolution into account.

Background parameterization. Due to the large amount of combinatorial background under the signal peak special care must be taken in choosing this part of the fit function. The background function must describe at the same time the $K\pi$ threshold on the left side and the exponential fall-off on the right side of the signal. The parameterization chosen is adopted from [agu91]:

$$BG(m) = a_0 \cdot \left(\frac{q}{m}\right)^{a_1} \cdot e^{-a_2 q - a_3 q^2}. \tag{4.8}$$

Here, $a_0 \ldots a_3$ are free parameters and q is the momentum transfer defined in (4.6). The background function is used both on Monte-Carlo and real data. It does describe the invariant mass distributions in all kinematic bins properly.

In section 5.2 we will evaluate the systematic uncertainty of the individual signal fits with respect to the background description. In this context we will compare (4.8) with another parameterization,

$$BG(m) = a_0 \left[1 - \left(\frac{1}{m + a_1}\right)\right]^{a_2} \cdot (1 + a_4 m)\,, \tag{4.9}$$

where again $a_0 \ldots a_4$ are free parameters. This empirical formula is adopted from [lin92] where it is used to describe the background for K^{*+} production in e^+e^- collisions.

Because of the complexity of the background parameterizations (4.8) and (4.9) look similar, describing the threshold behavior left of the signal by a power-law, and the region on the right side of the signal by an exponential or linear term. Function (4.9) does describe the background only in a limited range between 0.72-1.1 GeV. This is, however, completely sufficient for the systematic studies we want to perform.

Background subtraction based on event mixing techniques has been studied in detail. However, both the K^{*0} candidates mixed from like-sign tracks of the same event and from opposite-sign tracks of different events did not describe the background in all kinematic bins properly. Therefore, we do not use event mixing methods in this analysis.

Background composition. The dominant source of background in the invariant mass distribution is of combinatoric origin, i.e. due to $K\pi$ track pairs which do not belong to a common K^{*0} decay. The number of reconstructed K^{*0} is about one in 200 events (for the $\bar{K}^{*0}$, one in 250 events). On the other hand, after data selection each event comprises on average 13 tracks, 80 % of them pions. Since each identified kaon is combined with all other tracks of the event the number of wrong combinations is large compared to the number of expected K^{*0} decays, which leads to a significant background below the signal.

Another type of background originates from candidate track pairs which do not come from a common K^{*0} but from another resonance decay. One can distinguish two different contributions here, namely resonances which decay into the same final state as the K^{*0} and resonances which decay into another final state, one of its decay particles either mis-identified or not fully reconstructed.

The only known contributions to the first type of resonant background are decays of higher strange resonances like $K_0^*(1430)/K_2^*(1430)/K^*(1680) \to K\pi$. All of them do contribute well outside the K^{*0} signal region and the range of the invariant mass fit. Furthermore, their production cross section is much smaller than the K^{*0} production cross section. Therefore, these contributions do not need a special treatment and can be safely neglected.

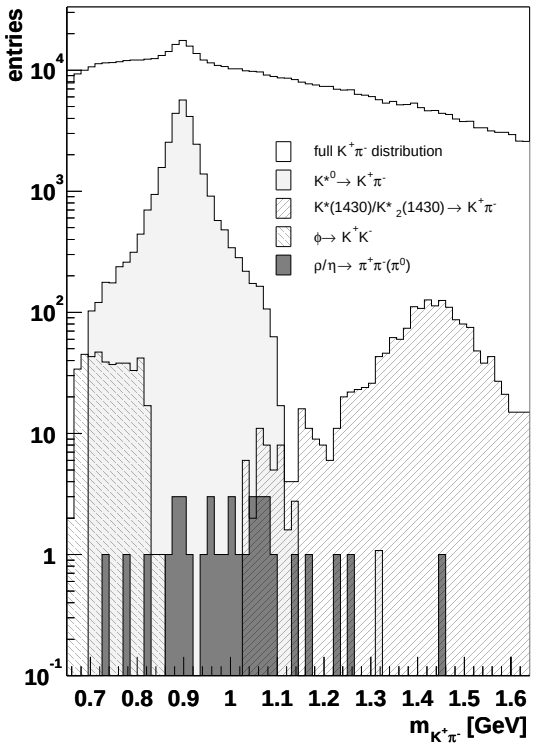

Figure 4.16: Expected contributions from resonances to the $K^+\pi^-$ invariant mass distribution. To select the daughter tracks of the resonances, the Monte-Carlo track matching method is used.

Contributions to the second type of resonant background arise from decays like $\rho \to \pi^+\pi^-$, $\eta \to \pi^+\pi^-\pi^0$, or $\Lambda \to p\pi^-$. These events are strongly suppressed by the kaon identification of the RICH, and can be neglected, too. For the same reason a contribution of $\bar{K}^{*0} \to K^-\pi^+$, which would accumulate directly under the K^{*0} peak, is only marginal. Sizeable contributions are found for the decay $\phi \to K^+K^-$. Since for the pion candidate track no particle identification is done in this analysis, one of the kaons is treated as a pion, and the ϕ mass is reflected to the left side of the K^{*0} signal peak.

Fig. 4.16 summarizes the expected contributions of the resonance decays $\phi \to K^+K^-$, $\rho \to \pi^+\pi^-$, $\eta \to \pi^+\pi^-\pi^0$, and $K^*(1430)/K_2^*(1430) \to K^+\pi^-$ to the K^{*0} invariant mass spectrum as obtained from the Monte-Carlo simulation. Compared to the expected K^{*0} signal yield all contributions are fairly small, and even negligible compared to the combinatorial background. Therefore, resonance contributions are not specially treated in the background parameterization.

4.5 Summary

After having introduced the data set and the Monte-Carlo simulation we have presented the data selection cuts used to obtain a clean K^{*0} signal. The kaon identification turned out to be the most powerful cut in the rejection of combinatorial background. Whenever possible we have compared the efficiencies of the

selection cuts in Monte-Carlo and real data, and both have been found to be in good agreement.

To study further the compatibility of the Monte-Carlo simulation with data we have compared kinematic distributions for single tracks. Although small deviations have been seen in certain distributions, all comparisons show a generally good agreement between data and Monte-Carlo.

The last part of this chapter concerned the signal reconstruction. The K^{*0} yield is extracted by a fit to the invariant mass distribution of $K\pi$ track pairs. The signal shape is described by a Breit-Wigner function convoluted with a Gaussian resolution function, and a background parameterization. Mass resolutions of about 5.5 MeV are obtained in data, which is slightly larger than predicted by the Monte-Carlo simulation (about 4.8 GeV).

In the following chapter we will use the invariant mass fit to extract the uncorrected differential distributions in p_T^2 and y from the data.

Chapter 5

Uncorrected differential distributions and acceptance

This chapter deals with the determination of the uncorrected differential distributions and corresponding acceptances in p_T^2 and y. The choice of binning is motivated and the extraction of the uncorrected distributions is presented. Afterwards, we evaluate the acceptances for all kinematic bins using the Monte-Carlo simulation. To get proper results a careful reweighting of the Monte-Carlo distributions is done which is also addressed in this chapter. As a last step we perform a comparison of azimuthal distributions for K^{*0} production in data and Monte-Carlo.

5.1 Uncorrected differential distributions

As a first step in the measurement of the differential cross sections $d\sigma/dp_T^2$ and $d\sigma/dy$ the reconstructed K^{*0} yield has to be determined in adequate bins of the kinematic variables. Section 5.1.1 documents the acceptance boundaries of the measurement and describes the choice of a proper binning to make a stable measurement possible. The extraction of the signal yield for all bins is described in section 5.1.2. Afterwards, we discuss the systematic uncertainties of the method used.

5.1.1 Acceptance coverage and choice of binning

The acceptance of the HERA-B detector covers the central rapidity region. The exact acceptance boundaries depend on the physics investigated. In forward direction the accessible phase space is limited by the fact that the Inner Tracker is not used. Tracks with a polar angle θ smaller than about 25 mrad cannot be reconstructed. For the K^{*0} decay this translates into an acceptance boundary in rapidity of $y_{max} = 4.5$ (in the lab frame). In the backward direction the geometrical limit for track reconstruction is $\theta \approx 250$ mrad in horizontal and $\theta \approx 160$ mrad in vertical direction, corresponding to a geometrical acceptance boundary of about $y_{min} = 2.2$. Due to the kaon identification cut, which imposes additional kinematic restrictions on the K^{*0}, the acceptance is further limited to $y_{min} = 2.6$. In total,

the measurement covers roughly two units in rapidity with mid-rapidity being at $y = 3.79$ in the lab frame.

Concerning the transverse phase space a good K^{*0} reconstruction is possible for all transverse momenta. Even for very small p_T^2 the acceptance is still large enough to allow a reasonable measurement. The high-p_T limit is given by the data statistics, since the production yields decrease strongly with increasing transverse momentum. A significant K^{*0} signal can be found up to $p_T^2 = 12\,\mathrm{GeV}^2$.

The phase space limits for K^{*0} reconstruction at HERA-B are summarized in table 5.1.

quantity	limits	no. of bins
rapidity	$2.6 \leq y \leq 4.5$	12
p_T^2	$0 \leq p_T^2 \leq 12\,\mathrm{GeV}^2$	11

Table 5.1: Phase space limits for reconstructing the decays $K^{*0} \to K^+\pi^-$ and $\bar{K}^{*0} \to K^-\pi^+$ at HERA-B. The high-p_T^2 limit is given by the statistics of the data sample. The number of bins for both differential distributions is given, too. For the complete binning, see appendix B.

Choice of binning. The final bins chosen for the differential distributions is a compromise between an as fine as possible binning in y and p_T^2 and a still significant amount of K^{*0} in the various bins. Despite the fact that the titanium data sample comprises only about 40 % of the statistics of the carbon and the tungsten samples, the same binning is chosen for all target materials, since this will allow a better comparison of the final results.

The choice of binning is also restricted by the p_T^2 and y resolution in the various bins. The binning should be chosen such that the resolution is much better than the width of the individual bins. Only in this case a bias of the measurement by bin-to-bin leakage can be excluded. In section 5.2.2 we will estimate the resolutions for each bin and show that leakage can be safely neglected.

For the measurement of the transverse distributions the data are divided into 11 bins in p_T^2. The statistical error of the signal yield in each bin does not exceed 5 % (8 % for titanium), apart from the highest p_T^2 bin, where the largest error is 17 % (on the titanium data in the $\bar{K}^{*0}$ channel). Rapidity is subdivided into 12 bins. In this case the statistical error is in all bins below 6 % (8 % on titanium). Only in the most forward and backward bins the error is a bit larger: up to 16 % is seen (again on the titanium sample in the $\bar{K}^{*0}$ channel).

The bins of both the p_T^2 and the y distributions are not of equal width but chosen with respect to the statistics found on data. The bin size in the central part of the rapidity distributions e.g. is 0.1 units in rapidity, while it is 0.4 units in rapidity in the most forward and backward bins. For the p_T^2 distributions the bin width is between $0.2\,\mathrm{GeV}^2$ at low p_T^2 and $5\,\mathrm{GeV}^2$ in the highest p_T^2 bin.

For details on the binning please refer to the cross section tables in appendix B.

5.1.2 Signal extraction in p_T^2 and y

The evaluation of the signal yields in the various bins is carried out using the following approach:

- For each candidate track-pair that is accepted by the data selection procedure described in section 4.2 the invariant mass m, the transverse momentum squared p_T^2, and the rapidity y of the K^{*0} candidate are calculated from the kinematics of the tracks. If the kinematic properties of a candidate are outside the phase space limitations chosen for this analysis (see table 5.1) it is discarded.

- For each p_T^2 bin an invariant mass distribution is filled. The same is done for rapidity. Note that different invariant mass distributions are filled for $K^{*0} \to K^+\pi^-$ and $\bar{K}^{*0} \to K^-\pi^+$, and for the three target materials.

- Each invariant mass distribution is fit as explained in section 4.4. The fit range is $0.66 \leq m \leq 1.2\,\mathrm{GeV}^2$. The mass resolution and the resonance mass are free parameters.

Fig. 5.1 shows the resulting uncorrected p_T^2 distributions, $^{dN}/_{dp_T^2}$, for all target

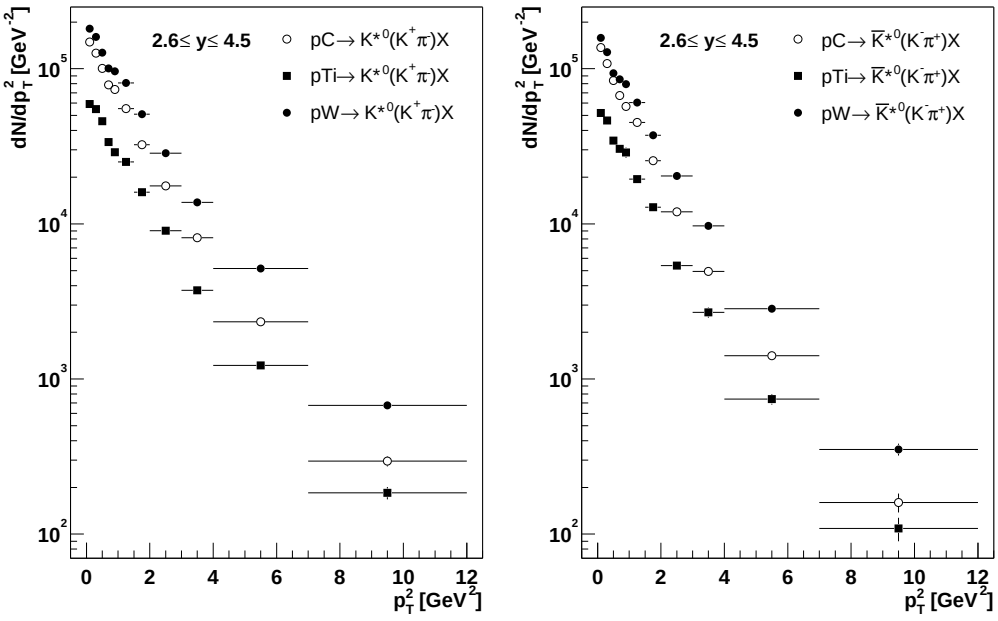

Figure 5.1: The uncorrected differential K^{*0} p_T^2 spectra. The errors are statistical only.

materials separately for K^{*0} and $\bar{K}^{*0}$. The error bars represent the errors of the individual fits. The respective rapidity distributions are shown in fig. 5.2.

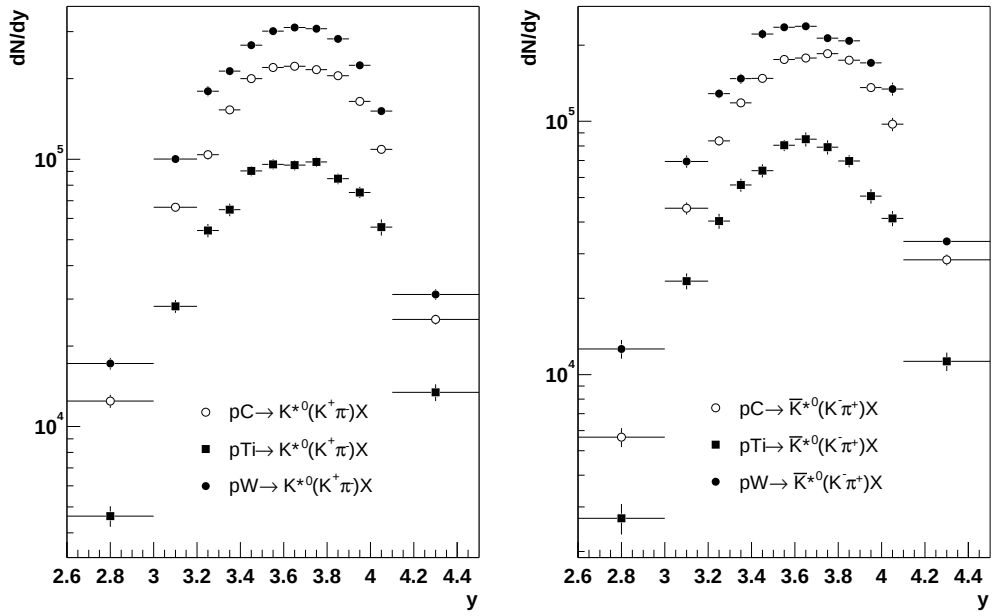

Figure 5.2: The uncorrected differential K^{*0} rapidity distributions. Signal yields are given per unit of rapidity. Errors are statistical only.

The χ^2/n.d.f. of the invariant mass fits for the K^{*0} rapidity distributions is exemplary shown in fig. 5.3, documenting that all fits perform well. Although this is the case several systematic influences can be identified which might in principle bias the fit result in the individual bins. They are investigated in the next section.

5.2 Systematic uncertainties of the distributions

The first possible systematic impact on the extraction of the uncorrected differential distributions concerns the signal fits performed in the individual bins of p_T^2 and y. We will study the impact of the background description on the signal yield and the stability of the fit results with respect to changes of the binning of the individual invariant mass distributions.

In a second step we will discuss a possible bias of the differential distributions by the finite detector resolution. In this context it is shown that with the binning chosen for the differential distributions such a bias can be safely neglected.

5.2.1 Uncertainty of the signal fits

To study possible systematic errors of the fit procedure on the signal yields we first focus on the background description of the signal fits. Afterwards, we address the binning of the invariant mass distributions.

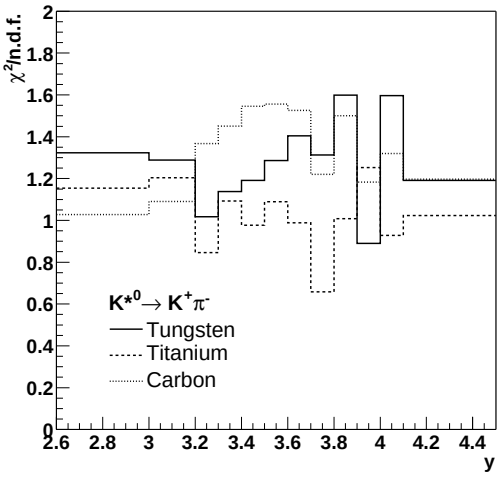

Figure 5.3: χ^2/n.d.f. of the K^{*0} invariant mass fits as a function of the various bins of y.

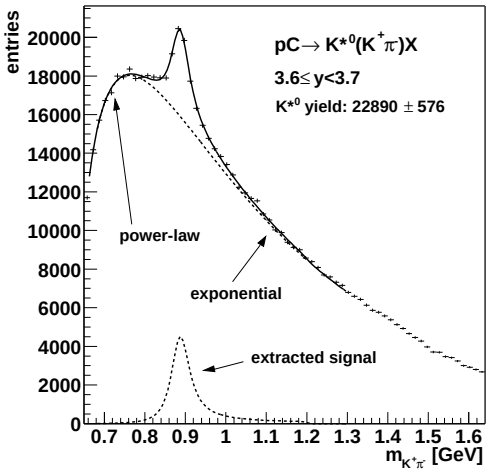

Figure 5.4: Typical invariant mass distribution. The signal fit has been superimposed (full line). The dashed lines show the background parameterization and the extracted signal.

Influence of the background parameterization. The K^{*0} ($\bar{K}^{*0}$) signal is governed by a large combinatorial background. To describe the background in all kinematic bins properly a complicated parameterization must be chosen (see section 4.4.2). It describes the behavior of the background at the $K\pi$ threshold by a power-law and changes to an exponential fall-off for large invariant masses. The signal sits at an invariant mass region where the power-law behavior passes over into the exponential fall-off, where we assume a smooth transition of the background under the peak (see fig. 5.4).

To study the influence of the background parameterization on the signal yields all differential distributions are re-fit bin-wise, replacing the standard background description introduced in (4.8) by the formula given in (4.9). The signal yields obtained in this way are compared to the yields found by using the standard parameterization. It turns out that the deviation between the two yields is for most p_T^2 and y bins in the order of the statistical error of the fit. For some bins the deviation exceeds the statistical uncertainty by more than a factor of 2. This is especially true for those bins in which the maximum of the background is below the resonance peak.

To reflect the impact of different background parameterizations on the error of the signal yields we take a somewhat conservative approach and consider the full deviation as a systematic error σ_{bg} of the signal yield. It is evaluated separately for each invariant mass fit and can be found in the cross section tables in appendix B. σ_{bg} contributes about 2 % to the systematic error of the total cross section measurement.

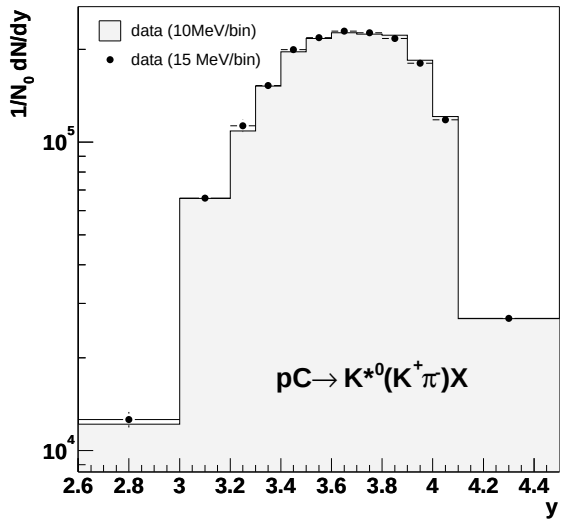

Figure 5.5: Comparison of two uncorrected K^{*0} rapidity distributions for the carbon wire. The filled histogram shows the signal yields obtained from invariant mass distributions with 10 MeV bin width. The data points show the result the standard 15 MeV binning. Errors are statistical only.

Binning of the invariant mass distributions. From the investigation of mass resolutions (see section 4.4.1) a bin size of 15 MeV has been found reasonable for the invariant mass distributions. To study the dependence of the signal yields on the binning, the bin size has been varied between 10-20 MeV. We have found no evidence for a systematic shift of the signal yields. For all distributions the change in yield is well below the statistical errors and can be safely neglected. This is exemplary shown in fig. 5.5 for the y distribution of $pC \rightarrow K^{*0}X$.

5.2.2 Impact of the detector resolution

Since the transverse momentum and rapidity of the K^{*0} are reconstructed with a finite accuracy only, the choice of the binning cannot be solely based on the data statistics but must take into account the detector resolution, too. If the width of each bin is much larger than the detector resolution a proper reconstruction of the K^{*0} kinematics is guaranteed (i.e. most of the K^{*0} candidates are reconstructed in the correct p_T^2 and y bins). If, however, the bin sizes are too small a substantial fraction of candidates is reconstructed in the wrong kinematic bin (migration), which introduces a bias to the shape of the distribution. To be sure that resolution effects do not play a substantial role for the chosen binning we will use two different methods to understand this effect quantitatively.

The first method is a comparison of the estimated resolution to the bin size and the second one deals with the calculation of bin purities. Both methods are based on the Monte-Carlo simulation and therefore rely on the correct simulation of the detector resolution. However, as is shown below, the chosen binning exceeds the resolution by far, such that we can assume that all conclusions stay valid even if the resolution is overestimated in the simulation. In this study we restrict ourselves to the K^{*0} decay, since the results for the $\bar{K}^{*0}$ are expected to be identical.

Comparison of resolution and bin size. The idea of the first method is to calculate the detector resolution separately for each bin of the differential distributions and compare it to the bin width. If the resolution is much better than the bin width no significant migration should occur. The proceeding is much like the way we have determined the mass resolution in section 4.4.1. We will explain the method for a bin in p_T^2, as it is applied in exactly the same way to the rapidity bins.

For all generated and reconstructed K^{*0} we calculate the residual Δp_T^2 between the reconstructed p_T^2 and the generated p_T^2:

$$\Delta p_T^2 = (p_T^2)^{reco} - (p_T^2)^{true}. \tag{5.1}$$

This is done separately for each bin of the reconstructed p_T^2 using the Monte-Carlo track matching method. The width $\sigma_{p_T^2}$ of the residual distribution is an estimate of the p_T^2-resolution, which can be directly compared to the respective bin size. Since the resolution might depend on the operated target, the residual distributions are determined separately for each target material. All distributions are well centered around zero, i.e. there is no systematic shift of the reconstructed p_T^2 towards higher or lower values. Furthermore, no large tails are observed, so that we can use the RMS of the distribution to estimate the resolution.

The results are shown fig. 5.6. The bin widths chosen for the analysis of the transverse differential distributions are superimposed. Typical resolutions are $\sigma_{p_T^2} \approx 10\,\mathrm{MeV}^2$ for $p_T^2 \approx 0$ and $\sigma_{p_T^2} \approx 100\,\mathrm{MeV}^2$ at $p_T^2 = 10\,\mathrm{GeV}^2$, in good approximation independent of the target material. The estimated resolution is much smaller than the width of each bin, which indicates that the bin-to-bin migration should be rather small.

The same study has been performed on the rapidity distributions (see fig. 5.7). As for the p_T^2 bins the resolution is much better than the bin widths, typical values being 0.01 in units of rapidity.

The method presented has the advantage of delivering absolute p_T^2 and y resolutions for each bin in p_T^2 and y, respectively. It has, on the other hand, the drawback that it does not provide the actual fraction of K^{*0} which are reconstructed in the correct kinematic bin. Even though we have shown that the estimated resolutions are better by almost an order of magnitude compared to the bin widths, we will evaluate this number in the following as a kind of cross-check.

Calculation of bin purities. An independent method to verify that the choice of binning is correct is the determination of bin purities. In explaining the method we restrict ourselves again to the p_T^2 binning.

The bin purity Π is defined bin-wise as

$$\Pi(p_T^2) = \frac{n_{K^*}^{gen,reco}}{n_{K^*}^{reco}}, \tag{5.2}$$

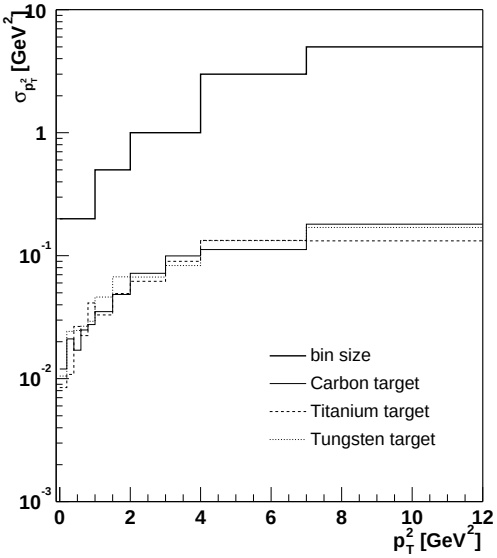

Figure 5.6: Monte-Carlo estimation of the p_T^2 resolution $\sigma_{p_T^2}$ as a function of p_T^2. The bin widths are superimposed, indicating that in each bin the resolution is much better than the corresponding bin width.

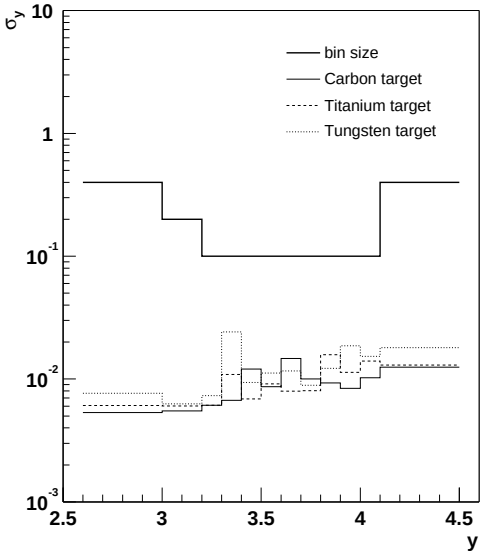

Figure 5.7: Same as in fig. 5.6 but for the rapidity distribution.

$n_{K^*}^{reco}$ being the number of K^{*0} reconstructed in the bin and $n_{K^*}^{gen,reco}$ the number of K^{*0} not only reconstructed, but also generated in this bin. Both numbers are obtained using the Monte-Carlo track matching method.

In this way the bin purity $\Pi(p_T^2)$ reflects the fraction of K^{*0} which have been reconstructed in the correct p_T^2 bin. In case of an ideal detector, i.e. $\sigma_{p_T^2} = 0$, all K^{*0} are reconstructed in the correct p_T^2 bins, hence $\Pi(p_T^2) \equiv 1$ for all bins. For a finite p_T^2 resolution, however, some K^{*0} are reconstructed with slightly different kinematics. As a result some fraction of them contributes to the wrong p_T^2 bin. In this case $\Pi(p_T^2) < 1$.

The bin purity has been determined for all bins of the p_T^2 and y distributions, separately for the three target materials. The results are shown in fig. 5.8 and fig. 5.9. It can be seen that the bin purity is not a smooth function of the kinematic variables. The reason for this is that the purity does not only depend on the resolution but also on the bin width: for a given bin the purity increases when the bin width is increased. This effect is seen in neighbored bins of different bin widths, since the resolution is a smooth function of the kinematic variables (see figs. 5.6 and 5.7).

The bin purity is in all cases better than 90 % with the only exception of the highest p_T^2 bin on the titanium wire where it drops to about 87 %. We consider these numbers large enough to prevent a systematic influence of the binning on

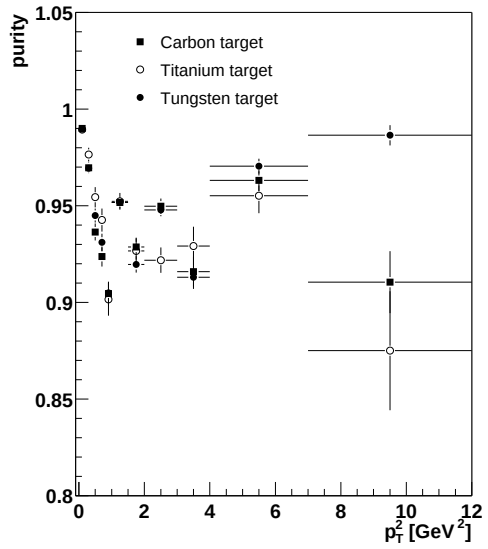

Figure 5.8: Bin purity as a function of the p_T^2 bin for the different data samples. See text for further explanation.

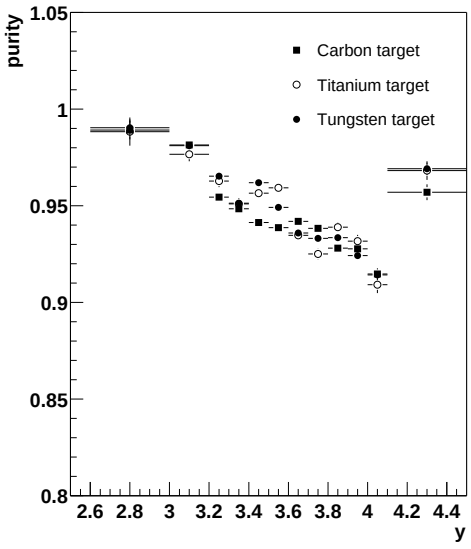

Figure 5.9: Same as in fig. 5.8 but as a function of rapidity.

the analysis.

To summarize, the performed studies of resolutions and bin purities show that no major impact on the analysis is expected from this side.

We will now turn to the determination of the acceptance corrections.

5.3 Acceptance determination

The differential K^{*0} distributions extracted from the data set do not have a physical meaning unless they have been corrected for the detection efficiency of the decay, which is called the acceptance. It is a function of the physics process, the finite detector and trigger capabilities in the various regions of the phase space, and the selection cuts applied in the analysis.

In this section we will derive the bin-wise acceptances for the K^{*0} decay using the Monte-Carlo simulation, assuming that the detector and cut efficiencies and the kinematics of the decay are well reflected by the simulation. As we will discuss in the next section a reweighting of the Monte-Carlo distributions is necessary to ensure this. After having presented the acceptances in all kinematic bins we will discuss possible systematic impacts on the acceptance determination.

5.3.1 Monte-Carlo reweighting

In chapter 4 we have compared some of the selection efficiencies on data and Monte-Carlo and have found them to be in good agreement. Furthermore, we have compared several single-track distributions which are based on our data selection. No unreasonable difference between data and simulation has been observed. This is, however, not true for the kinematic distributions of the K^{*0}, as we will see in an moment. The impact of this observation on the acceptance determination is the topic of this section.

While the invariant cross section is assumed to factorize in p_T^2 and y for a large region of the phase space, this is in general not true for the uncorrected distributions. In this case p_T^2 and rapidity are usually not independent of each other, because the data selection cuts out some parts of the phase space. Fig. 5.10 illustrates this effect. It shows Monte-Carlo distributions of generated and reconstructed K^{*0} in the $p_T^2 - y$ plane. On the generated distribution p_T^2 and rapidity are independent of each other at least within the rapidity range accessible at HERA-B (indicated by horizontal lines). For the distribution of the reconstructed $K^{*0}(892)$ the picture looks completely different as the reconstruction introduces a correlation between p_T^2 and y.

When we measure e.g. single differential distributions in rapidity, we implicitly integrate over the available phase space in p_T^2, i.e. we determine the differential cross section in slices of y. To correctly determine the acceptances in the various y slices we must therefore ensure that the p_T^2 distributions of the K^{*0} are in good agreement in data and Monte-Carlo. The same is true for the evaluation of the p_T^2 acceptances for which the rapidity distributions in MC and data have to be in reasonable agreement.

To estimate the level of agreement between data and Monte-Carlo we compare reconstructed p_T^2 distributions. The data distributions have already been extracted in section 5.1.2. Accordingly, Monte-Carlo p_T^2 distributions of reconstructed K^{*0} and $\bar{K}^{*0}$ are derived for each target material. As an example, fig. 5.11 shows the comparison between data and Monte-Carlo for the carbon target. Obviously, the Monte-Carlo generator assumes a much softer behavior of the transverse kinematics. The reason for this is that the FRITIOF generator used for the HERA-B event simulation is tuned to describe the soft part of the transverse spectrum, whereas the hard tail is simulated only insufficiently by using a variant of the Rutherford scattering algorithm on parton level [pi92].

In order to produce correct acceptances for the rapidity distributions the p_T^2 spectra in the Monte-Carlo have to be reweighted. It is common practice to choose a p_T^2 parameterization according to measurements of other experiments. However, there exist no data on K^{*0} production at the HERA-B center-of-mass energy. Therefore, we perform the reweighting with respect to our own data distributions. We will show that afterwards the rapidity distributions of data and Monte-Carlo are in good agreement.

The weighting function $w(p_T^2)$ is determined separately for each target material. It

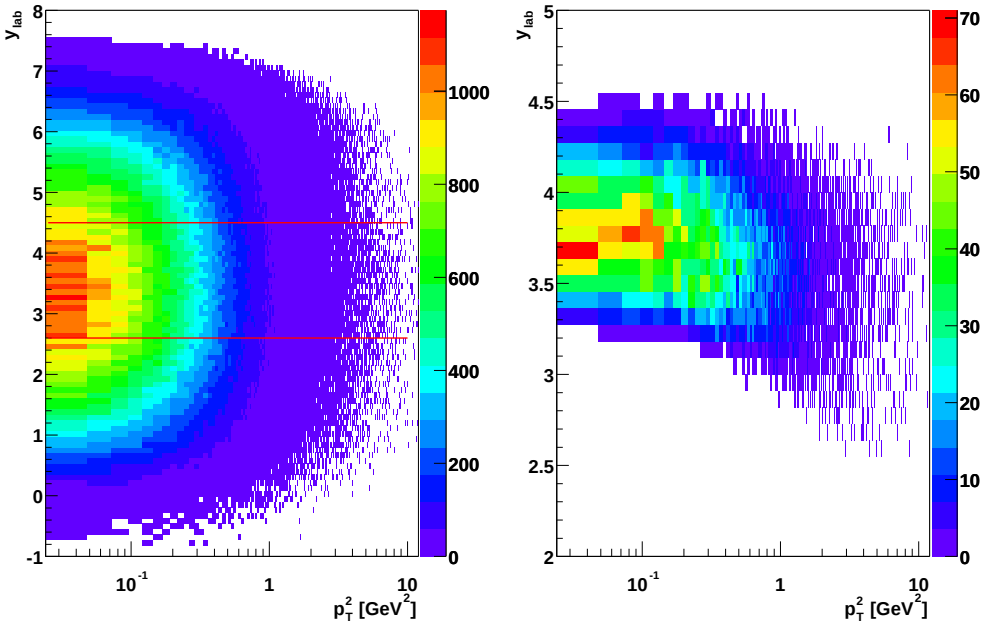

Figure 5.10: Monte-Carlo distributions of K^{*0} production in the $p_T^2 - y$ plane. *Left:* Generator distribution showing the full phase space of the decay. The y-range accessible by HERA-B is indicated by the horizontal lines. *Right:* Distribution of reconstructed K^{*0} after application of all selection cuts. Clearly, rapidity and transverse momentum are not independent of each other any more.

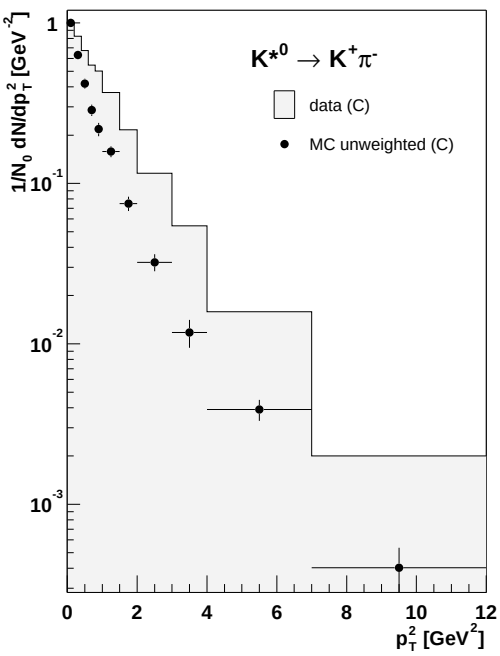

Figure 5.11: Comparison of uncorrected differential distributions in p_T^2 for data and Monte-Carlo before reweighting. The Monte-Carlo simulation underestimates the data significantly. The distributions are normalized to the first bin.

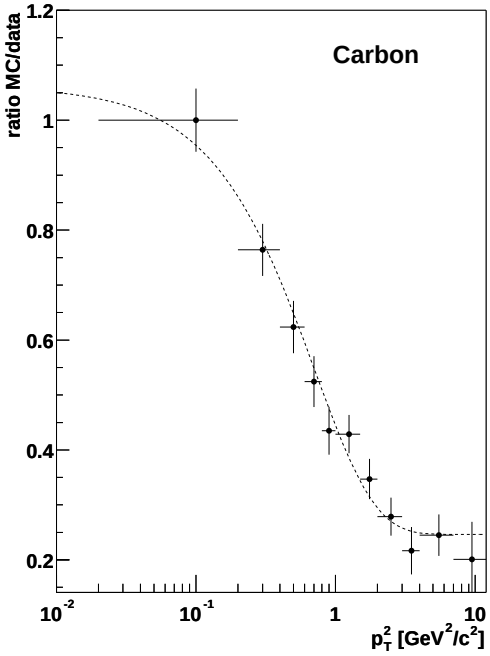

Figure 5.12: Ratio of the Monte-Carlo and data distribution as a function of p_T^2. A simple exponential function is fit to the data and serves as a weighting function.

is found by parameterizing the ratio between the unweighted p_T^2 distribution from Monte-Carlo and the p_T^2 distribution from data. A simple exponential ansatz,

$$w(p_T^2) = a_0 + a_1 e^{-a_2 p_T^2}, \tag{5.3}$$

describes the ratios well, as is shown in fig. 5.12. The fit parameters $a_0 \dots a_2$ obtained for the individual target materials are summarized in table 5.2.

The reweighted Monte-Carlo distributions in p_T^2 and y are derived in much the

reaction	a_0	a_1	a_2 [GeV^{-2}]
$pC \to K^{*0}X$	0.25 ± 0.02	0.82 ± 0.06	1.41 ± 0.22
$pTi \to K^{*0}X$	0.25 ± 0.03	0.86 ± 0.09	1.37 ± 0.27
$pW \to K^{*0}X$	0.18 ± 0.02	0.96 ± 0.06	1.07 ± 0.13
$pC \to \bar{K}^{*0}X$	0.18 ± 0.05	0.96 ± 0.07	0.99 ± 0.17
$pTi \to \bar{K}^{*0}X$	0.22 ± 0.04	0.95 ± 0.10	0.22 ± 0.04
$pW \to \bar{K}^{*0}X$	0.17 ± 0.03	1.01 ± 0.07	0.97 ± 0.14

Table 5.2: Fit parameters of the weighting function (5.3) for the different target materials. See text for further explanation.

same way as the unweighted distributions. As explained in section 5.1.2 an invariant mass distribution is filled for each bin of p_T^2 (y). However, instead of filling each candidate track pair with a weight of 1, a weight of $w^{-1}(p_T^2)$ is applied to correct the deviation between the data and Monte-Carlo p_T^2 distributions. In this way K^{*0} candidates with large p_T^2 get high weights, while low-p_T candidates are filled with weights close to 1.

The result of the reweighting is seen both in the p_T^2 and y distributions on Monte-Carlo. Fig. 5.13 compares the p_T^2 distribution of the reweighted Monte-Carlo with the respective data distribution. By construction no systematic deviation between data and Monte-Carlo is seen any more. The influence of the reweighting on the rapidity distribution is shown in fig. 5.14. The unweighted Monte-Carlo distribution is systematically shifted with respect to data. After reweighting data and Monte-Carlo are in good agreement. This behavior is seen in the rapidity distributions of all materials.

In the next sections we will derive the acceptances for the differential distributions. In doing this we will exclusively use the reweighted Monte-Carlo samples. Before the final numbers are presented a short summary on the different contributions to the acceptance is given.

5.3.2 Acceptance definition and composition

Strictly speaking the term acceptance as it is used in this analysis states the probability to detect a $K^{*0} \to K^+\pi^-$ ($\bar{K}^{*0} \to K^-\pi^+$) decay within a certain kinematic region after having applied all selection cuts. To motivate the different contributions to the acceptance a we approximate it for the moment by the product of

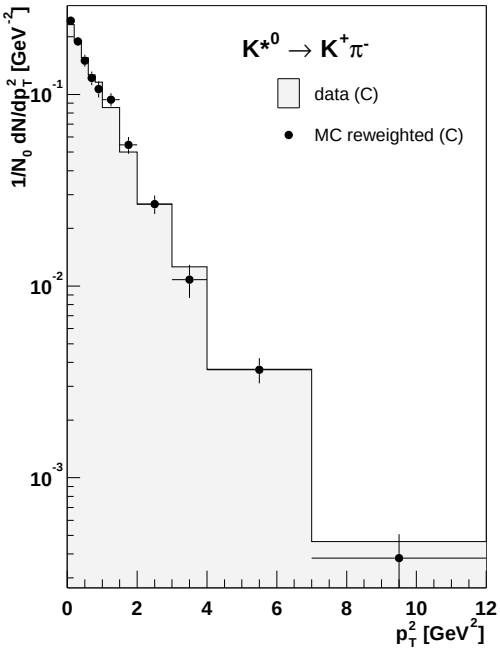

Figure 5.13: Uncorrected p_T^2 distributions for data and Monte-Carlo after reweighting. By construction, the Monte-Carlo reproduces the data. The distributions are normalized to the the same number of entries.

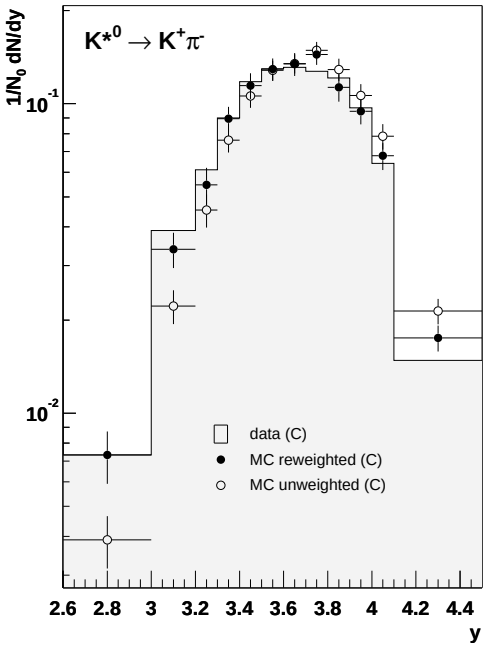

Figure 5.14: Uncorrected rapidity distributions for data and Monte-Carlo. The difference in shape due to the reweighting is nicely seen in the Monte-Carlo distributions. After the reweighting a good agreement between data and Monte-Carlo is observed.

various efficiencies, which can in principle be evaluated separately:

$$a \equiv a(p_T^2, y) \approx \epsilon_{geo} \cdot \epsilon_{reco} \cdot \epsilon_{cuts}. \tag{5.4}$$

The different efficiencies involved are:

- the geometric acceptance ϵ_{geo}, which is the probability that the decay products of the K^{*0} traverse the sensitive volume of the detector. The geometric acceptance is limited in the forward direction by the Inner Tracker, since tracks with a polar angle of about $\theta \leq 25\,\text{mrad}$ in the lab frame cannot be reconstructed. In the backward hemisphere the acceptance limit is given by the Outer Tracker to about $\theta \leq 250\,\text{mrad}$ in the horizontal and $\theta \leq 160\,\text{mrad}$ in the vertical direction.

- the reconstruction efficiency ϵ_{reco} reflecting the probability that both daughter tracks of the K^{*0} are fully reconstructed and combined into a common vertex in the target region. ϵ_{reco} is the product of the two track efficiencies ϵ_{track}^{K} and ϵ_{track}^{π} and the vertex efficiency $\epsilon_{vtx}^{K\pi}$:

$$\epsilon_{reco} = \epsilon_{track}^{K} \cdot \epsilon_{track}^{\pi} \cdot \epsilon_{vtx}^{K\pi}. \tag{5.5}$$

- the efficiency ϵ_{cuts} of the selection cuts introduced in section 4.2. This includes the kaon identification efficiency and the efficiencies of the track quality cuts.

The factorization ansatz (5.4) is however only a rough approximation of the acceptance, because some of the involved efficiencies are correlated with each other. To take those correlations into account the acceptance is not evaluated on the basis of the different efficiencies but is determined from the Monte-Carlo simulation by bin-wise comparing the number of reconstructed K^{*0} $n_{\text{reco}}^{K^{*0}}$ to the generated ones $n_{\text{gen}}^{K^{*0}}$. For the different p_T^2 and y bins we therefore obtain

$$a(p_T^2) = \frac{n_{reco}^{K^{*0}}(p_T^2)}{n_{gen}^{K^{*0}}(p_T^2)} \text{ and } a(y) = \frac{n_{reco}^{K^{*0}}(y)}{n_{gen}^{K^{*0}}(y)}, \tag{5.6}$$

respectively. The reconstructed K^{*0} from Monte-Carlo have passed the same reconstruction and analysis chain as the data. The kinematics of both the generated and reconstructed K^{*0} are restricted to the phase space accessible by the measurement (see table 5.1). In this way the acceptances $a(p_T^2)$ for the p_T^2 bins are averaged over the accessible y phase space. Similarly, the acceptances for the various rapidity bins, $a(y)$, are averaged over the accessible p_T^2 phase space. Given that the various efficiencies are reproduced by the simulation this method is the most reliable way of acceptance determination. While the number of generated K^{*0} within a certain kinematic bin is directly known from the Monte-Carlo simulation two different methods exist to extract the number of reconstructed K^{*0}. We will explain the advantages and drawbacks of both methods in the next section.

5.3.3 Method of acceptance determination

In the Monte-Carlo the number of reconstructed K^{*0} can principally be determined in two ways:

- Count the number of reconstructed K^{*0} in a certain kinematic bin by using the Monte-Carlo track matching method (cf. section 4.1.2).
- Fit for each kinematic bin the invariant mass distribution of the K^{*0} candidates as done for data (see section 5.1.2).

The first method has the advantage of being easily applicable. Since the reconstructed daughter tracks are known to originate from a generated K^{*0}, the acceptance determination is reduced to counting the fraction of the generated K^{*0} which have been reconstructed. The error on the acceptance is small because binomial statistics can be applied. However, in section 4.1.2 we have already noted that the efficiency of the matching procedure is only about 80 % and depends slightly on the kinematics. Hence, it is not suited for a precise acceptance calculation.

The second possibility of acceptance determination is not to use the Monte-Carlo truth information on the reconstruction level, but to evaluate the number of reconstructed K^{*0} by fitting invariant mass distributions for each bin, as it is done for data. The acceptance for each bin is afterwards obtained by comparing the K^{*0} signal yield to the number of generated K^{*0} using eq. (5.4).

The latter method does not depend on a proper matching between reconstructed tracks and generated particles. However, it has the drawback that the error on the acceptance is determined by the invariant mass fit, i.e. it is in general much bigger than the binomial error that is used in case of the Monte-Carlo track matching method. Nevertheless, we will use this method in the following, since it is the only one which is a priori unbiased. The method based on Monte-Carlo track matching will only be used to demonstrate the impact of the various analysis cuts on the acceptance.

5.3.4 Acceptances in p_T^2 and y

In this section the final acceptances of the differential distributions are presented. They are derived using the invariant mass fit method described in the last section. Possible systematic uncertainties arising from the acceptance determination are addressed in the following section.

Before presenting the final results we will, however, demonstrate the impact of the various analysis cuts on the acceptance. Fig. 5.15 shows the acceptance in p_T^2 as a function of the different cuts applied. The strongest impact comes from the kaon identification, imposing the 9.6 GeV momentum cut on the kaon daughter track of the K^{*0}. The same is true for the acceptance in rapidity, where the kaon identification strongly reduces the acceptance in the backward direction (see fig. 5.16). In forward direction the acceptance gets more and more limited by the missing Inner Tracker, as has been explained in section 5.1.1. Note that for both

figures we have used the Monte-Carlo track matching method, i.e. the absolute values of the acceptance are underestimated.

The final acceptances of the p_T^2 distributions are shown in fig. 5.17. For all target

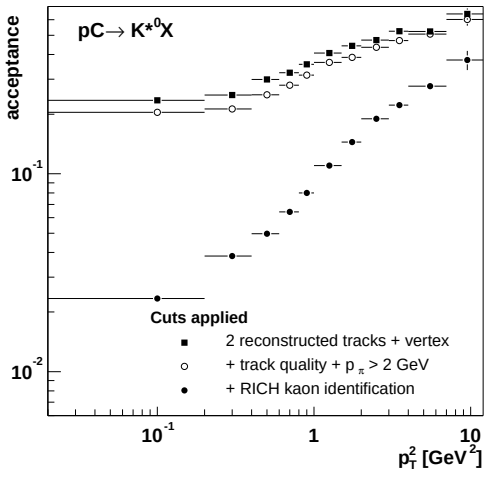

Figure 5.15: p_T^2 acceptance as a function of the different analysis cuts. Note that this plot was done using the Monte-Carlo track matching method.

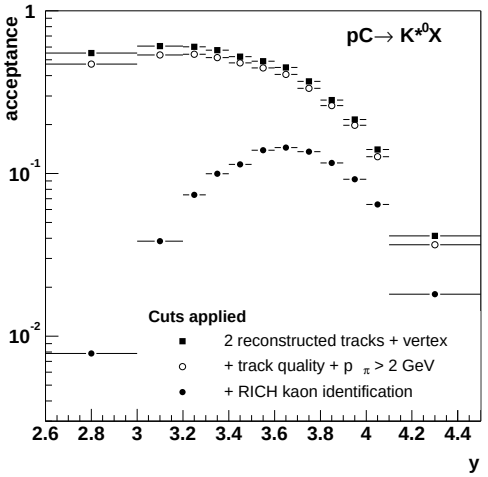

Figure 5.16: y acceptance as a function of the different analysis cuts. Again, this plot was made using the Monte-Carlo track matching method.

materials and both for $K^{*0} \to K^+\pi^-$ and $\bar{K}^{*0} \to K^-\pi^+$ they look similar, raising from about 3 % at low p_T^2 to about 30 % in the highest p_T^2 bin. The acceptances of the different target materials are compatible with each other, i.e. their ratios are compatible with being equal to one (see table 5.3). The same is true for the acceptance ratios between K^{*0} and $\bar{K}^{*0}$.

The error on the acceptances is significantly larger than the statistical error of the

	$K^{*0} \to K^+\pi^-$		$\bar{K}^{*0} \to K^-\pi^+$	
	ratio	χ^2/n.d.f.	ratio	χ^2/n.d.f.
C/Ti	0.97 ± 0.04	0.48	1.01 ± 0.05	0.54
C/W	1.10 ± 0.04	0.84	1.08 ± 0.05	1.21
Ti/W	1.10 ± 0.05	0.49	1.05 ± 0.06	0.86

Table 5.3: Acceptance ratios in p_T^2 for the different target materials, separately for $K^{*0} \to K^+\pi^-$ and $\bar{K}^{*0} \to K^-\pi^+$. The numbers are obtained by fitting a constant to the ratio. The χ^2/n.d.f. of each fit is given, too.

uncorrected data. This is due to the limited Monte-Carlo statistics, which even prevents a reliable acceptance determination for the the highest p_T^2 bin of the $pC \to \bar{K}^{*0}X$ acceptance. To reduce the impact of the acceptance error on the final p_T^2 distributions we parameterize the acceptance empirically by a second order

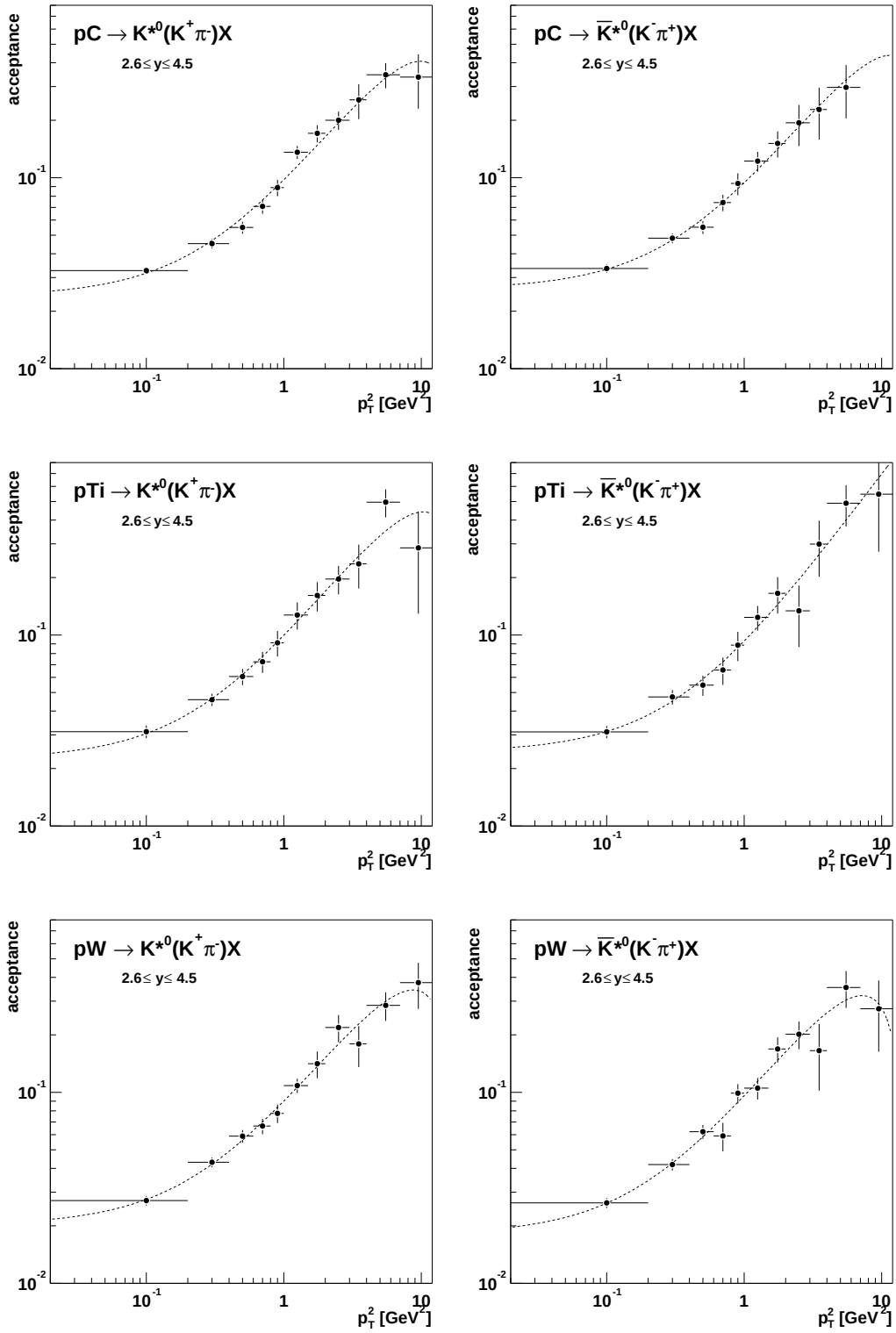

Figure 5.17: Acceptance as a function of p_T^2 after all cuts. The fit results of the parameterization (5.7) are shown as dashed lines.

polynomial:

$$a(p_T^2) = a_0 p_T^4 + a_1 p_T^2 + a_2, \tag{5.7}$$

with $a_0 \ldots a_2$ being free parameters. In fig. 5.17 the fits of the parameterization to the various acceptances are shown as dashed curves, the fit results being summarized in table 5.4. This parameterization will be used for the final acceptance correction. Additionally, the acceptance for $pC \to \bar{K}^{*0}X$ in the highest p_T^2 bin is extrapolated using the parameterization. Even if the systematic uncertainty on the extrapolation is presumably large, no further study of the systematic error has been done, since this bin does not significantly contribute to the total cross section measurement.

The final acceptances for the rapidity distributions are shown in fig. 5.18. Again

	$K^{*0} \to K^+\pi^-$			
	$a_0\,[10^{-3}\ \mathrm{GeV}^{-4}]$	$a_1\,[10^{-2}\ \mathrm{GeV}^{-2}]$	$a_2[10^{-2}]$	χ^2/n.d.f.
C	-3.94 ± 1.30	7.78 ± 0.52	2.39 ± 0.15	1.41
Ti	-3.95 ± 1.99	8.14 ± 0.85	2.24 ± 0.26	0.62
W	-4.27 ± 1.28	7.42 ± 0.56	2.01 ± 0.17	0.52
	$\bar{K}^{*0} \to K^-\pi^+$			
	$a_0\,[10^{-2}\ \mathrm{GeV}^{-4}]$	$a_1\,[10^{-2}\ \mathrm{GeV}^{-2}]$	$a_2[10^{-3}]$	χ^2/n.d.f.
C	-3.08 ± 3.50	7.12 ± 0.83	2.61 ± 0.22	0.47
Ti	-0.16 ± 2.97	6.90 ± 0.98	2.44 ± 0.68	0.58
W	-5.82 ± 1.50	8.40 ± 0.69	1.80 ± 0.19	0.82

Table 5.4: Results of the p_T^2 acceptance parameterizations using (5.7).

the limited Monte-Carlo statistics is responsible for the relatively large errors. In the most backward bin for $\bar{K}^{*0} \to K^-\pi^+$ on the carbon target there are not enough entries in the invariant mass distribution to reliably fit the signal and determine the acceptance. Therefore, the differential cross section measurement is limited to $3.0 \leq y \leq 4.5$ in this case. The ratios of the different acceptances are again flat within errors and compatible with being 1. Only the acceptance of the $\bar{K}^{*0} \to K^-\pi^+$ decay on the carbon target seems to be a little bit underestimated compared to the other results. From the point of the acceptance determination, however, no suspicious problems could be identified. Unlike the p_T^2 acceptances the y acceptances could not be commonly described by a simple parameterization.

In the next section we will study possible systematic impacts on the acceptance determination. We will investigate the impact of different background parameterizations on the acceptance and review the influence of the Monte-Carlo reweighting.

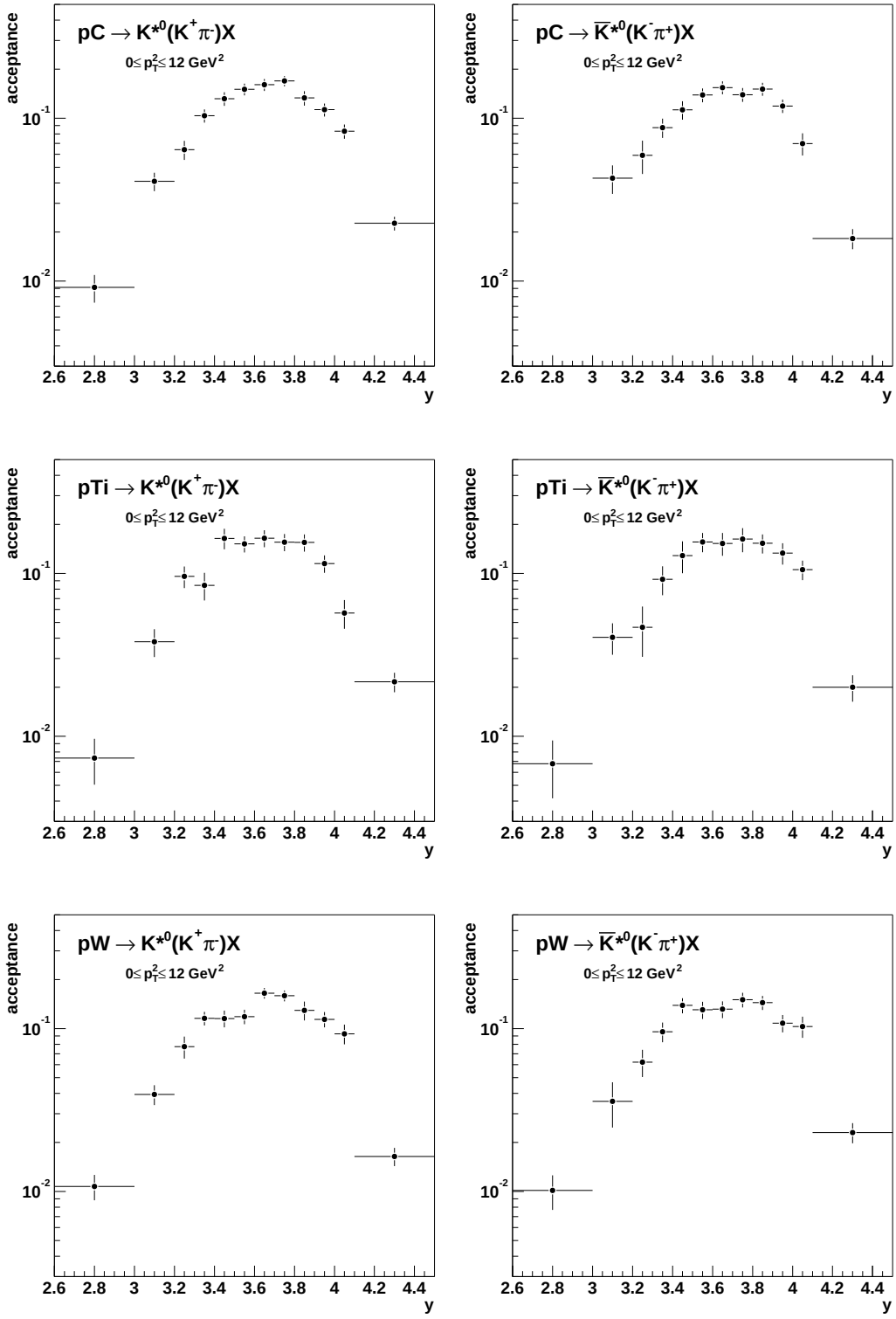

Figure 5.18: Acceptance in rapidity after all cuts. In the backward direction the kaon track identification limits the acceptance significantly. In the forward direction the unused Inner Tracker reduces the acceptance.

	$K^{*0} \to K^+\pi^-$		$\bar{K}^{*0} \to K^-\pi^+$	
	ratio	χ^2/n.d.f	ratio	χ^2/n.d.f
C/Ti	0.95 ± 0.05	1.03	0.89 ± 0.06	0.45
C/W	1.01 ± 0.04	0.85	0.93 ± 0.05	0.92
Ti/W	0.98 ± 0.05	1.71	1.02 ± 0.07	0.46

Table 5.5: Acceptance ratios in rapidity for the different target materials, separately for $K^{*0} \to K^+\pi^-$ and $\bar{K}^{*0} \to K^-\pi^+$.

5.3.5 Systematic studies

Since the acceptance is determined by fitting the invariant mass distributions for the various bins in p_T^2 and y, it might suffer from the same problems as the extraction of the uncorrected differential distributions. In section 5.2 we have seen that the background parameterization of the signal fit has a sizable impact on the yield of the signal.

The same study was performed on the Monte-Carlo fits used for the acceptance determination, and the signal yield obtained using the different background parameterizations was compared. Since the statistical error of the signal fits is substantially larger than for data, no effect on the signal yields is seen within errors. That means that no impact on the acceptance is expected. Indeed, fig. 5.19 demonstrates that the acceptances obtained with the two background parameterizations are the same within errors. Therefore, no additional systematic uncertainty is taken into account from this side.

The effect of Monte-Carlo reweighting on the acceptances in rapidity has already

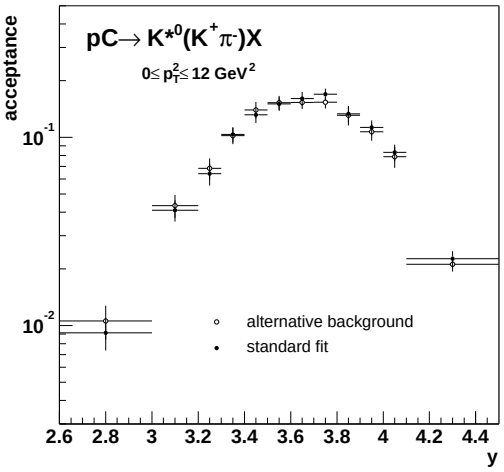

Figure 5.19: Comparison of the influence of different background parameterizations on the acceptance. Within the statistical errors no deviation is found.

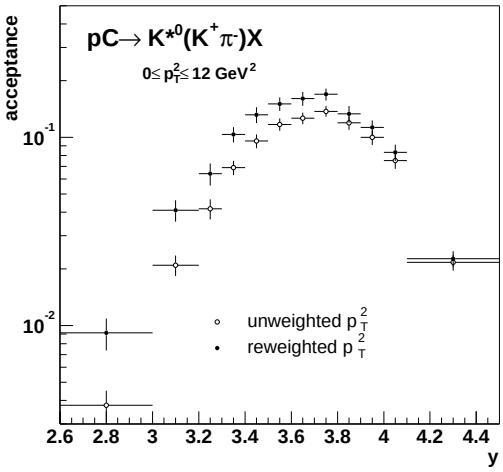

Figure 5.20: Impact of the Monte-Carlo reweighting on the acceptance in rapidity. In backward direction the acceptance gets more and more underestimated.

been discussed in section 5.3.1 and the impact of reweighting on the Monte-Carlo rapidity distribution has been demonstrated. To be complete, the impact of the reweighting on the rapidity acceptance is shown in fig. 5.20. Without a proper reweighting the acceptance in y is drastically underestimated in most of the bins. Only in the very forward direction a reasonable agreement is seen.

By looking again at fig. 5.10 on page 85 we see that this behavior is indeed expected. In the backward region only high-p_T K^{*0} are reconstructed. Since the unweighted Monte-Carlo underestimates the high-p_T tail of the K^{*0} distribution significantly, less K^{*0} are reconstructed in the backward rapidity bins. Hence, the acceptance drops. In the forward rapidity bins the low-p_T region of the phase space dominates. As in this regime the unweighted Monte-Carlo describes the data reasonably, the acceptances found with the unweighted and the reweighted Monte-Carlo coincide.

Our studies of possible impacts on the acceptance determination did not reveal any obvious problem. Within their errors all acceptances seem to be properly determined. Before we discuss the final cross section measurements we will perform, as a last step in the series of cross-checks between data and Monte-Carlo, a comparison of K^{*0} differential distributions as a function of the azimuthal angle ϕ.

5.4 Azimuthal distributions

In section 4.3 we have already demonstrated that concerning the azimuthal distributions of single tracks data and Monte-Carlo are in reasonable agreement (see fig. 4.13 on page 66). We will now show that this is also true for the azimuthal distribution of the K^{*0}. Such distributions are particularly suited for comparisons between data and Monte-Carlo. Since beam and target are unpolarized, the azimuthal angle does not contain any physics information, i.e. the particle production is isotropic in ϕ. Therefore, a comparison of reconstructed ϕ distributions on data and Monte-Carlo is independent of any particle production model and does only test the capabilities of the Monte-Carlo to simulate the detector performance.

Fig. 5.21 shows the resulting distributions in ϕ for all target materials, separately for $K^{*0} \to K^+\pi^-$ and $\bar{K}^{*0} \to K^-\pi^+$. Within the large statistical errors of the Monte-Carlo good agreement between the real data and the simulation is seen. The $K^{*0} \to K^+\pi^-$ decay is dominantly reconstructed in the $+x$ region of the detector, i.e. in the bending direction of positively charged tracks (see also the single track azimuthal distributions in fig. 4.13 on page 66). For the $\bar{K}^{*0}$ the acceptance is largest for the $-x$ direction. This effect is most probably due to so-called in-bending tracks: if e.g. a K^{*0} is produced to the $-x$-direction, most of its K^+ daughter particle are, too. By the magnetic field they are however bent to the $+x$-direction, such that the probability is high that they leave the Outer Tracker acceptance on the inner (the Inner Tracker) side. This results in the observed acceptance loss for the K^{*0} in the $-x$-direction (and for the $\bar{K}^{*0}$ in the $+x$-direction).

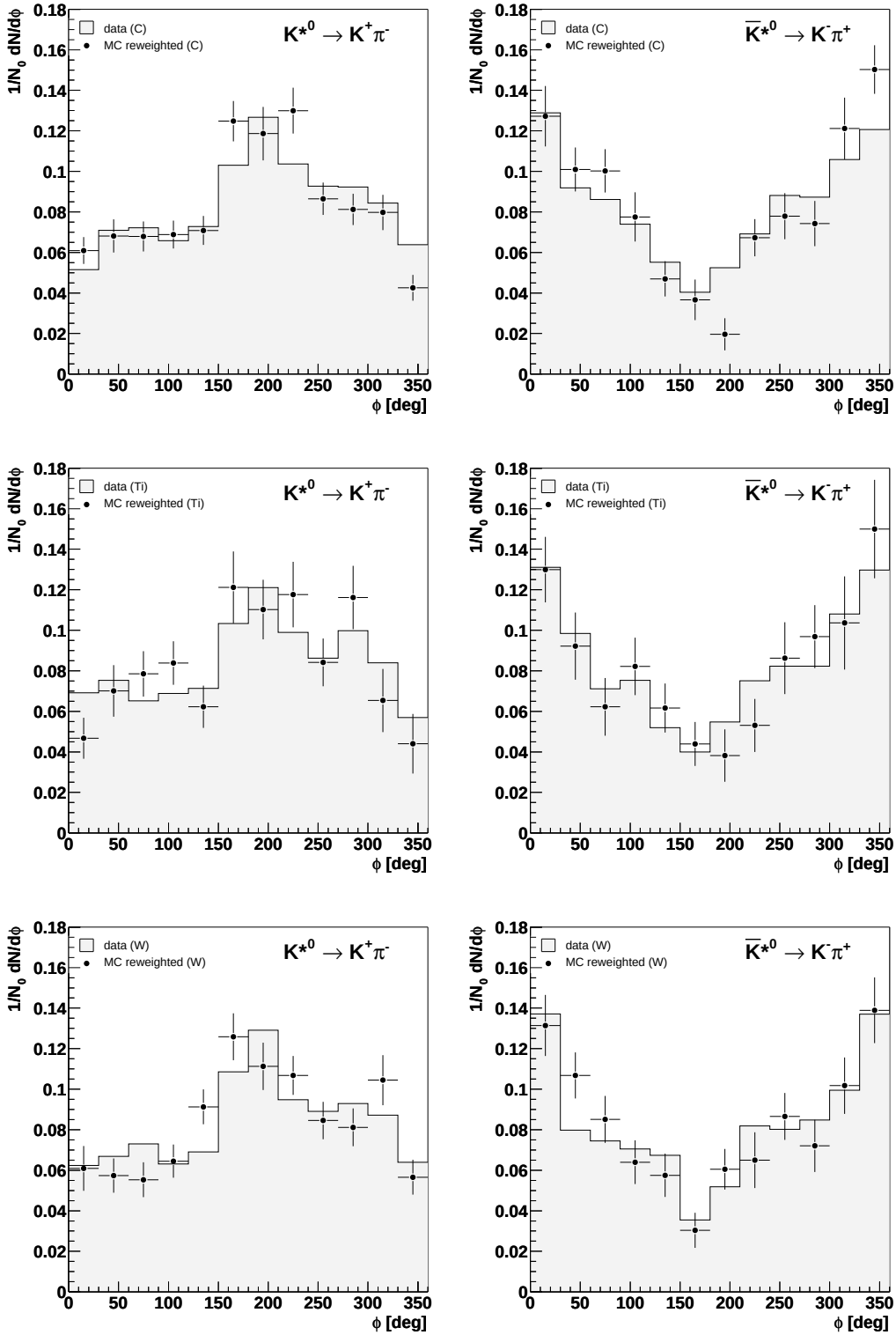

Figure 5.21: Comparison of reconstructed azimuthal distributions in data and Monte-Carlo in the accessible phase space. The distributions are normalized to the same number of entries.

5.5 Summary

The geometric acceptance of the HERA-B detector covers the mid-rapidity region. In our analysis of K^{*0} production the fact that the Inner Tracker has not been used limits the acceptance in the forward direction to $y \leq 4.5$. In the backward hemisphere, it is the kaon identification which imposes an acceptance boundary at $y \geq 2.6$. In transverse momentum a measurement is possible within $0 \leq p_T^2 \leq 12\,\mathrm{GeV}^2$, where the high-$p_T$ limit is given by the data statistics.

The accessible phase space region is subdivided into either 12 bins in rapidity or 11 bins in transverse momentum squared to obtain single-differential distributions. Using two different methods we have checked that the choice of the binning does not influence the shape of the distributions. Finally, we have obtained the uncorrected differential distributions dN/dy and dN/dp_T^2 by fits to the invariant mass distributions of the individual kinematic bins. We have studied in detail possible systematic impacts on the signal yield and found out that the proper parameterization of the combinatoric background under the signal peak plays an important role for a reliable signal extraction. Using two different parameterizations a systematic error on the signal yield was estimated, which dominates in many cases the statistical uncertainties of the mass fit.

The acceptance of the various bins of the differential distributions have been obtained in much the same way as the distributions themselves. For each bin fits to the invariant mass distributions of simulated and reconstructed K^{*0} decays have been performed. The acceptance is derived by comparing bin-wise the signal yield to the number of generated K^{*0} decays.

For both the transverse and the longitudinal distributions the acceptances obtained for the different target materials are compatible with each other. The same is true if one compares the acceptances of $K^{*0} \to K^+\pi^-$ and $\bar{K}^{*0} \to K^-\pi^+$. By looking in which way the different analysis cuts contribute to the total acceptance we have found that the kaon identification cut does not only restrict the acceptance in the backward hemisphere but also limits the overall acceptance significantly.

Due to the limited Monte-Carlo statistics the error on the acceptance is large in some bins, and large fluctuations of the acceptance are seen. To overcome this problem the acceptance in p_T^2 has been parameterized. For the correction of the differential distributions this parameterization will be used rather than the acceptances themselves.

In deriving the acceptances we have observed that the Monte-Carlo simulation does not describe the kinematic distributions of the K^{*0} properly. Since a good agreement is needed to evaluate the acceptances correctly, the Monte-Carlo p_T^2 distributions have been reweighted with respect to the p_T^2 distribution obtained from data. We have further shown that after the reweighting the K^{*0} rapidity distributions are in agreement for data and Monte-Carlo.

Finally, we have once again checked the reliability of the Monte-Carlo simulation by comparing azimuthal distributions of reconstructed K^{*0} and $\bar{K}^{*0}$. In doing so we have obtained a good agreement. Our next step will be the final evaluation of the differential and total K^{*0} and $\bar{K}^{*0}$ production cross sections.

Chapter 6

The K^{*0} production cross sections

The previous chapters have laid the foundations for the final results of the analysis. Now that the uncorrected differential distributions and the corresponding acceptances are available we will present the differential K^{*0} and $\bar{K}^{*0}$ production cross sections vs. rapidity and p_T^2. Afterwards, the total production cross sections are calculated by extrapolating the measured distributions to full phase space. Finally, we will investigate the atomic number dependence of the total cross section and the differential distributions as a function of the kinematic variables. Whenever possible we discuss our results in the context of other measurements and compare to Monte-Carlo predictions.

6.1 Inclusive cross section measurement

In this section we will present the K^{*0} and $\bar{K}^{*0}$ production cross sections both as a function of y and p_T^2 and integrated over the acceptance of the measurement. The rapidity distributions will be compared to predictions of the HERA-B Monte-Carlo generator. The p_T^2 spectra we will fit to the parameterizations introduced in section 1.3.3. The atomic number dependence of the cross sections is discussed separately in section 6.3.

6.1.1 Integration of the differential cross sections

The cross section $\sigma_{K^{*0}}^{pA}$ for K^{*0} production within the acceptance boundaries of the measurement can be obtained in two different ways, namely by integrating either the acceptance corrected differential distributions $d\sigma/dy$ over y or $d\sigma/dp_T^2$ over p_T^2. Formally, for the integration of $d\sigma/dy$,

$$\sigma_{K^{*0}}^{pA} = \int_{y_{min}}^{y_{max}} \frac{N_{K^{*0}}(y)|_{0\le p_T^2 \le 12\,\mathrm{GeV}^2}}{a(y)\cdot\Delta y\cdot\mathcal{L}_{ia}\cdot BR(K^{*0}\to K^+\pi^-)}\,dy, \tag{6.1}$$

with $N_{K^{*0}}(y)$ being the number of reconstructed K^{*0} in the considered y bin, Δy the bin width, and $a(y)$ the total acceptance in this bin. The integrated luminosity of the data sample is denoted as $\mathcal{L}_{ia}$, and $BR(K^{*0}\to K^+\pi^-)$ is the branching ratio

of the investigated decay. Table 6.1 summarizes these quantitites separately for each target material and documents the acceptance boundaries of the various measurements. Remind that due to lack of Monte-Carlo statistics the most backward bin in rapidity is missing for $pC \to \bar{K}^{*0}X$.

Correspondingly, the integration of the transverse momentum distribution yields

$$\sigma^{pA}_{K^{*0}} = \int_{p^2_{T,min}}^{p^2_{T,max}} \frac{N_{K^{*0}}(p^2_T)|_{2.6\le y\le 4.5}}{a(p^2_T)\cdot \Delta p^2_T \cdot \mathcal{L}_{ia} \cdot BR(K^{*0} \to K^+\pi^-)}\, dp^2_T. \tag{6.2}$$

Similar formulae are used to obtain the integrated cross sections for $\bar{K}^{*0}$ production.

All necessary ingredients to the cross section measurement have been derived in

	C		Ti	W
	K^{*0}	$\bar{K}^{*0}$	$K^{*0}/\bar{K}^{*0}$	$K^{*0}/\bar{K}^{*0}$
rapidity range	[2.6;4.5]	[3.0;4.5]	[2.6;4.5]	[2.6;4.5]
p^2_T range [GeV^2]	[0;12]	[0;12]	[0;12]	[0;12]
$\mathcal{L}_{ia}$ [μb^{-1}]	252.2 ± 8.8		33.7 ± 1.2	32.1 ± 1.1
BR [%]	66.601 ± 0.006			

Table 6.1: Phase space boundaries of the cross section measurements for the various target materials, integrated luminosities [aus04] of the three data sets, and the branching ratio [hag02] of the investigated decay mode.

the previous chapters. The number of reconstructed K^{*0} in the various bins of p^2_T and y have been evaluated and discussed in section 5.1.2, and the corresponding acceptances have been determined in section 5.3. All numbers including the statistical and systematic errors are summarized in appendix B.

The resulting K^{*0} and $\bar{K}^{*0}$ production cross sections $\sigma^{pA}_{K^{*0}}$ and $\sigma^{pA}_{\bar{K}^{*0}}$ within the kinematic limits of the measurement are listed in table 6.2, separately integrated using (6.1) and (6.2). In both ways the same result is obtained, as is expected if the extraction of the uncorrected distributions and the determination of the acceptances have been done correctly. The errors quoted in the table denote the statistical and systematic errors, respectively. For a discussion on the systematic errors, see section 6.1.2.

In table 6.2 we also compare the measured cross sections to the predictions of the HERA-B Monte-Carlo generator FRITIOF 7.02, which has been updated for the latest measurements of branching ratios of higher resonance decays. Since the Monte-Carlo does not predict cross sections but only production rates of particles, the respective K^{*0} production cross sections have been calculated by scaling the number of generated K^{*0} per event with the inelastic pA cross section σ^{pA}_{inel} of the target material (given in table 3.2). The results are in remarkable agreement with what is obtained from the measurements.

The ratio R between the K^{*0} and the $\bar{K}^{*0}$ production cross sections at mid-rapidity

	C	Ti	W
$\sigma^{pA}_{K^{*0}}$ [mb]		$pA \rightarrow K^{*0}X$	
$\int dy$	$15.6 \pm 0.1 \pm 1.5$	$55.1 \pm 0.8 \pm 6.1$	$176.3 \pm 1.7 \pm 15.9$
$\int dp_T^2$	$15.9 \pm 0.2 \pm 1.3$	$51.3 \pm 0.8 \pm 4.2$	$182.2 \pm 2.1 \pm 14.8$
MC	16.5	50.5	176.1
$\sigma^{pA}_{\bar{K}^{*0}}$ [mb]		$pA \rightarrow K^{*0}X$	
$\int dy$	$11.8 \pm 0.1 \pm 1.1$	$43.4 \pm 0.8 \pm 5.3$	$136.6 \pm 1.7 \pm 14.8$
$\int dp_T^2$	$13.5 \pm 0.1 \pm 1.1$	$43.7 \pm 0.8 \pm 3.6$	$145.1 \pm 1.7 \pm 12.0$
MC	13.9	42.1	143.4

Table 6.2: The K^{*0} and $\bar{K}^{*0}$ production cross sections within the kinematic boundaries of the measurement. Note that the cross section for $pA \rightarrow \bar{K}^{*0}X$ has been measured in $3.0 \leq y \leq 4.5$ only. The quoted errors denote the statistical and the systematic errors, respectively.

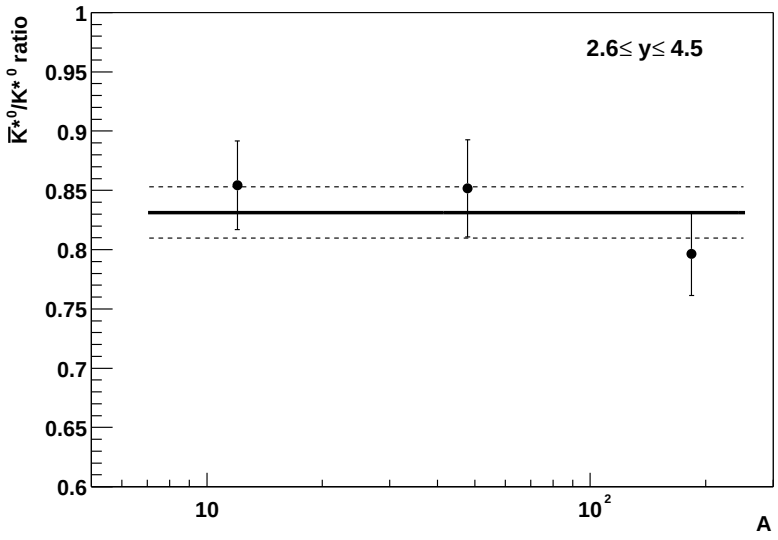

Figure 6.1: Ratio between the $\bar{K}^{*0}$ and K^{*0} production cross sections at mid-rapidity for the different target materials. The horizontal lines indicate the average and the RMS of the results.

is shown in fig. 6.1 as a function of the target material. Within the errors of the measurement the ratios are compatible with each other. For the cross section ratio averaged over all materials we obtain

$$R = \frac{\sigma^{pA}_{K^{*0}}}{\sigma^{pA}_{\bar{K}^{*0}}} = 0.83 \pm 0.02. \tag{6.3}$$

The fact that $R < 1$ has already been observed in pp collisions at smaller center-of-mass energies (see e.g. fig. 1.2 on page 12), where the same tendency is also seen for the production cross section ratios of K^{*+}/K^{*-}. An explanation might be that in pp and pA collisions the K^{*0} (K^{*+}) can be produced in association with a strange baryon (e.g. via $pp \to p\Sigma^+K^{*0}$ or $pp \to p\Lambda K^{*+}$), while for the $\bar{K}^{*0}$ this channel is suppressed.

Before we come to the presentation of the differential distributions and the total cross section extrapolation the various uncertainties contributing to the total systematic error of the cross sections are summarized.

6.1.2 Summary of systematic errors

To guarantee reliable results several checks on the data have been performed to estimate possible systematic uncertainties of the measurement. Within this analysis the following systematic errors have been determined:

- For each bin of the differential distributions the signal yield has been obtained by a fit of the respective invariant mass distribution. To estimate the systematic impact of the background description each fit has in addition been performed using an alternative background parameterization (see section 5.2). Conservatively, the difference in yield between both fits is taken as a systematic error σ_{bg} on the signal yield. Its contribution to the total systematics is about 2 %.

- The limited Monte-Carlo statistics imposes an uncertainty σ_{mc} of about 5 % on the acceptance determination. It is added to the total systematic error rather than to the statistical error of the measurement to keep the statistical error free of contributions which do not directly arise from the size of the data sample.

- The dependence of the cross section measurement on the analysis cuts was investigated in detail. Therefore, the cuts were varied within a large range of possible values. The largest deviation in cross section is found when the track quality cuts are completely omitted and instead a soft pion identification by the RICH is demanded. In this case a deviation of about 2 % is observed in the integrated cross sections.
  Since it was for technical reasons not possible to release the kaon identification cut, the uncertainty of its efficiency was estimated in the following way: by using the Monte-Carlo simulation the momentum distribution of kaons from reconstructed K^{*0} has first been corrected for the efficiency found in

the Monte-Carlo (cf. fig. 4.7 on page 61). Afterwards the result has been convoluted with the kaon identification efficiency obtained from data. The difference of about 6.5 % is taken as a systematic error on the kaon identification. In total, the contribution of the analysis cuts to the total systematic error is about $\sigma_{cuts} = 7\,\%$.

- The systematic uncertainty of the luminosity determination has been taken from [aus04]. On average a systematic error of $\sigma_{lumi} = 3.5\,\%$ has been found.
- An additional error σ_{br} is applied due to the uncertainty of the branching ratio of the K^{*0} decay [hag02]. However, this error does contribute less than 0.1 % to the total systematics.

Finally, the total systematic error is obtained by quadratically summing the different contributions:

$$\sigma_{tot}^{sys} = \sqrt{\sigma_{bg}^2 + \sigma_{mc}^2 + \sigma_{cuts}^2 + \sigma_{lumi}^2 + \sigma_{br}^2}. \tag{6.4}$$

It exceeds by far the statistical error of the cross section measurements.

6.1.3 Differential cross sections

Fig. 6.2 shows the K^{*0} and $\bar{K}^{*0}$ inclusive differential production cross sections as a function of rapidity for all target materials. The cross sections are reasonably flat in rapidity, as expected from fragmentation models (see section 2.1.4). Furthermore, the Monte-Carlo predictions indicated by the dashed lines describe the measurements not only in shape, but also with respect to the absolute cross sections.

The differential cross sections $d\sigma/dp_T^2$ at mid-rapidity are presented in fig. 6.3 as a function of p_T^2. Towards high-p_T a significant flattening of the distributions is observed. This behavior is nicely described by fits to the power-law parameterization discussed in section 1.3.3,

$$\frac{d\sigma}{dp_T^2} = C\left[1 + \left(\frac{p_T^2}{p_0^2}\right)^{-\beta}\right], \tag{6.5}$$

which have been superimposed in fig. 6.3. The fit results including the $\langle p_T \rangle$ of the distributions are summarized in table 6.3.

Statistically, the mean transverse momenta of our measurements are compatible with each other, $\langle p_T \rangle \approx 0.7\,\mathrm{GeV}$. We see, however, evidence of a systematic dependence of $\langle p_T \rangle$ on the target material, since it increases with the atomic mass number. This is a first hint that the A-dependence of the cross section depends on p_T. We will further investigate this observation in section 6.3.

To compare our results with other measurements, we have additionally fit the p_T^2 differential cross sections of K^{*0} and $\bar{K}^{*0}$ production in $\pi^- Si$ collisions [faw90], shown in fig. 1.3 on page 13. The results of the fits can be found in table 6.3.

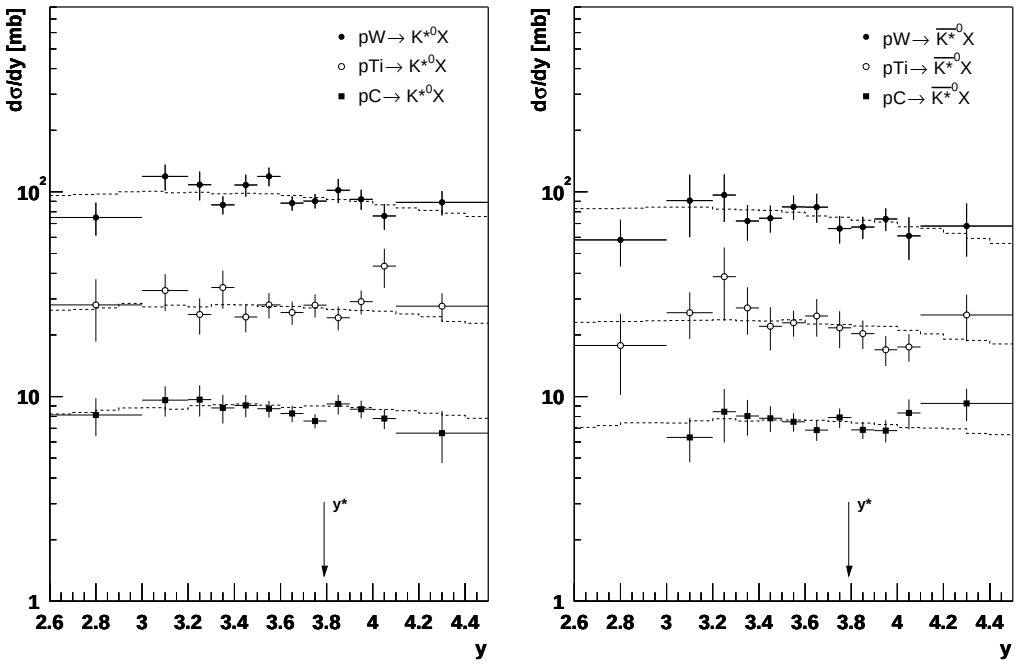

Figure 6.2: Inclusive differential cross sections $^{d\sigma}/_{dy}$ for K^{*0} and $\bar{K}^{*0}$ production at mid-rapidity. The dashed lines indicate the Monte-Carlo predictions.

	β	p_0^2 [GeV^2]	$\langle p_T \rangle$ [GeV]	χ^2/n.d.f.
		$pA \to K^{*0}X$		
C	4.99 ± 0.20	1.95 ± 0.16	0.69 ± 0.04	1.92
Ti	4.71 ± 0.22	1.85 ± 0.19	0.70 ± 0.04	1.44
W	4.48 ± 0.21	1.87 ± 0.20	0.73 ± 0.05	2.20
π^-Si	*6.27 ± 0.48*	*1.96 ± 0.21*	*0.58 ± 0.04*	*1.59*
		$pA \to \bar{K}^{*0}X$		
C	5.49 ± 0.27	2.11 ± 0.20	0.66 ± 0.04	1.38
Ti	5.88 ± 0.40	2.41 ± 0.30	0.68 ± 0.05	0.69
W	4.33 ± 0.21	1.57 ± 0.18	0.69 ± 0.05	2.39
π^-Si	*5.20 ± 0.36*	*1.37 ± 0.15*	*0.56 ± 0.04*	*1.65*

Table 6.3: Results of the power-law fits to the full p_T^2 region. At the bottom the results of our fits to the data of π^-Si collisions at $\sqrt{s}$ = 19 GeV [faw90] are shown.

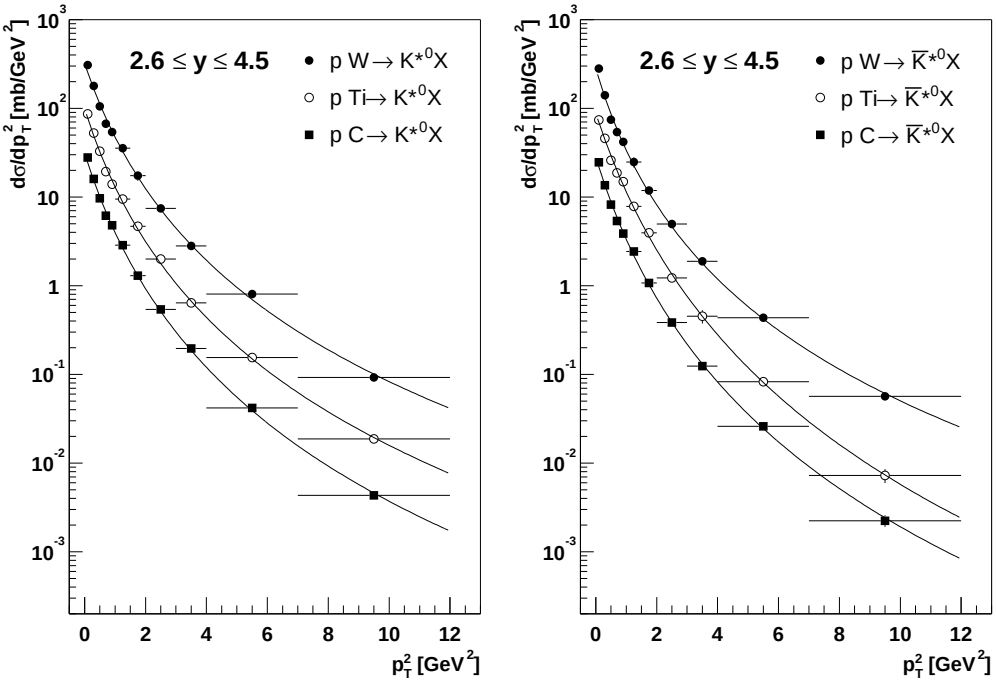

Figure 6.3: Transverse differential cross sections $d\sigma/dp_T^2$ for K^{*0} and $\bar{K}^{*0}$ production at mid-rapidity. The cross sections are evaluated for $2.6 \leq y \leq 4.5$. Fits to the parameterization (6.5) are superimposed.

In the direct comparison of $\langle p_T \rangle$ we notice that the values obtained from the measurements of [faw90] are significantly smaller. Such a behavior is expected as an effect of the smaller center-of-mass energy and has been observed e.g. in J/ψ production, too [buc01]. Note that even if we compare different projectiles we expect a similar production mechanism at mid-rapidity.

For the K^{*0} production at low p_T we expect an exponential behavior of the differential cross section, as predicted by models describing soft hadronic interactions [hag65]. To study the shape of the p_T^2 distributions in this regime we have fit them to the exponential ansatz (1.7) introduced in section 1.3.3:

$$\frac{d\sigma}{dp_T^2} = B\, e^{-bp_T^2}. \tag{6.6}$$

The fit was performed in the region $0 \leq p_T^2 \leq 1\,\mathrm{GeV}^2$, where only a marginal flattening of the distributions is expected [gei90]. Indeed the χ^2/n.d.f. of the fits becomes significantly worse if we include bins of higher p_T^2. The fit results

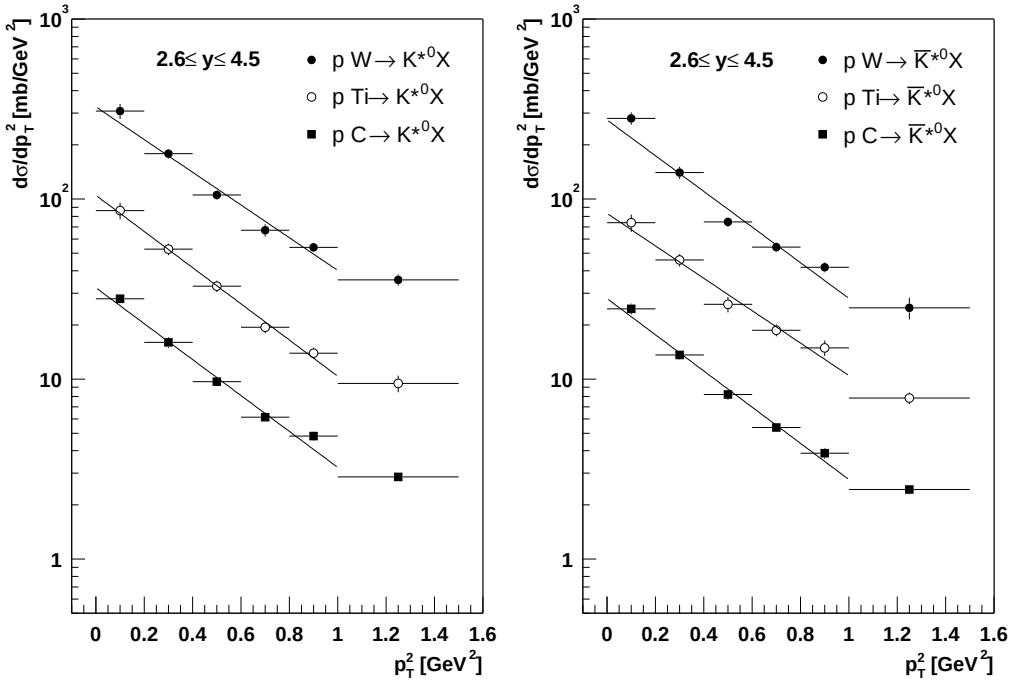

Figure 6.4: Exponential fits to the low-p_T^2 region of the cross section measurements. The onset of flattening beyond $p_T^2 = 1\,\mathrm{GeV}^2$ is clearly seen.

for the six differential cross sections are shown in fig. 6.4. The corresponding values are summarized in table 6.4, where we have again included the results of our fits to the data of [faw90]. All distributions are reasonably described by the parameterization. In case of the tungsten data, however, the fit underestimates the lowest p_T^2 bin. Compared to the power-law fit results the $\langle p_T \rangle$ of the exponential

	b [GeV^{-2}]	$\langle p_T \rangle$ [GeV]	χ^2/n.d.f.
		$pA \to K^{*0}X$	
C	2.30 ± 0.11	0.58 ± 0.03	3.71
Ti	2.31 ± 0.14	0.58 ± 0.03	0.60
W	2.09 ± 0.12	0.61 ± 0.03	3.25
π^-Si	*2.58 ± 0.05*	*0.55 ± 0.01*	*2.80*
		$pA \to \bar{K}^{*0}X$	
C	2.31 ± 0.12	0.58 ± 0.03	1.94
Ti	2.07 ± 0.17	0.62 ± 0.05	1.63
W	2.28 ± 0.14	0.59 ± 0.04	7.54
π^-Si	*2.94 ± 0.08*	*0.52 ± 0.01*	*3.86*

Table 6.4: Results of the exponential fits to the low-p_T region. At the end of each section, our fit results to the π^-Si data of [faw90] are shown.

parameterization is generally smaller, because this ansatz does not take into account the flattening of the distributions at high-p_T. As in the case of the power-law fit, the numbers are larger compared to what is obtained from fits to the data of [faw90].

6.2 Total cross section extrapolation

In section 6.1.1 we have determined the K^{*0} and $\bar{K}^{*0}$ production cross sections within the acceptance of the HERA-B detector. They have been evaluated in two different ways, namely by integrating the differential distributions $d\sigma/dy$ and $d\sigma/dp_T^2$. In both ways we have obtained comparable results within the errors of the measurements.

In order to allow a comparison of the cross sections with other measurements they have to be extrapolated to the full phase space. In transverse momentum no extrapolation is necessary, since the total cross section is dominated by the low-p_T region. The last bin in p_T^2, $7\,\text{GeV}^2 \le p_T^2 \le 12\,\text{GeV}^2$, does only contribute about 0.1 % to the total cross section, which means that contributions beyond $p_T^2 = 12\,\text{GeV}^2$ can be safely neglected.

In the longitudinal phase space, however, the measurement is limited to mid-rapidity, i.e. an extrapolation is needed. In doing so we will rely on the Monte-Carlo simulation, since there are no experimental data available for K^{*0} production at the HERA-B center-of-mass energy. Of course this approach depends on the kinematic model used by the generator. Systematic uncertainties arising from the model dependence are hard to estimate unless other generators using different model ansatzes are at hand. In principle, the HIJING [wan91] generator would be suited for such a systematic study but its adaption to the HERA-B kinematics was out of the scope of this thesis. Therefore, no further systematic error on the phase space extrapolation is applied. Note, however, that within the ac-

ceptance of our measurement the differential cross sections and the Monte-Carlo predictions have been shown to be in in good agreement (see fig. 6.2), so that a Monte-Carlo based extrapolation is justified.

By using the Monte-Carlo simulation we find that the phase space coverage of our measurement is about 45 % for K^{*0} production (in $2.6 \leq y \leq 4.5$) and about 48 % for $\bar{K}^{*0}$ production. Due to the missing most-backward bin a value of 38 % is obtained for $\sigma^{pC}_{\bar{K}^{*0}}$. The exact numbers are documented in table 6.5.

The cross section extrapolation is schematically illustrated in fig. 6.5, shown ex-

	phase space coverage [%]	
	$pA \rightarrow K^{*0}X$	$pA \rightarrow \bar{K}^{*0}X$
C	44.7	48.2 (38.1)
Ti	44.6	48.8
W	44.5	48.3

Table 6.5: Phase space coverage of the K^{*0} and $\bar{K}^{*0}$production cross section measurements. The numbers are evaluated on the Monte-Carlo generator level for an acceptance of $2.6 \leq y \leq 4.5$. In case of $d\sigma/dy$ for $pC \rightarrow \bar{K}^{*0}X$ the acceptance is $3.0 \leq y \leq 4.5$ only, which is reflected in a smaller phase space coverage (given in brackets).

emplary for $pC \rightarrow K^{*0}X$. The data points indicate the measured differential production cross section, while the histogram represents the K^{*0} rapidity dis-

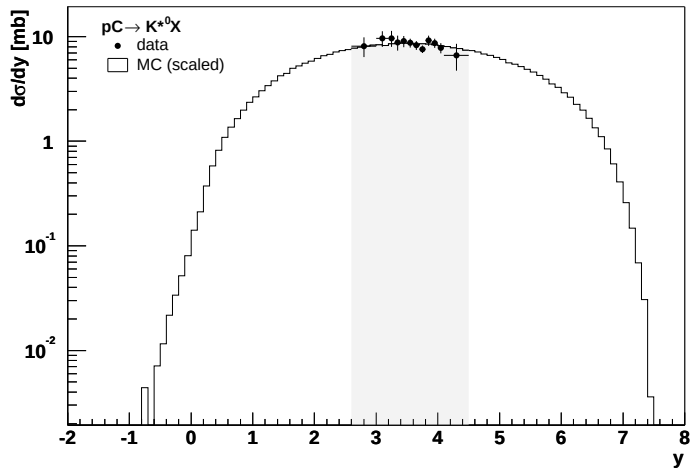

Figure 6.5: Illustration of the full phase space extrapolation of the K^{*0} production cross section. For the differential distribution shown the the experimental data cover 45 % of the total phase space.

tribution predicted by the Monte-Carlo generator. Looking at the phase space boundaries we note that in backward direction the rapidity exceeds $y = 0$ towards negative values. This can be understood as an effect of the presence of nuclear matter. Due to the nuclear binding forces and the Fermi motion of the

nucleons inside the nucleus the center-of-mass energy calculated between the beam projectile and a target nucleon at rest is not a fixed number. As a result a small fraction of particles obtains negative rapidities in the lab frame.

By correcting the production cross sections evaluated in section 6.1.1 for the finite phase space coverage of the measurement we obtain the total production cross sections $\sigma^{pA}_{K^{*0},tot}$ and $\sigma^{pA}_{\bar{K}^{*0},tot}$ summarized in table 6.6. Since we have found the integrated cross sections $\sigma^{pA}_{K^{*0}}$ and $\sigma^{pA}_{\bar{K}^{*0}}$, obtained by integrating either $d\sigma/dy$ or $d\sigma/dP_T^2$, to be in good agreement, we have taken their average in all cases.

If we compare the total production cross sections to the inelastic pA cross sections

C	Ti	W
$\sigma_{tot}(pA \to K^{*0}X)$ [mb]		
35.1 ± 0.3 ± 3.1	119.3 ± 1.8 ± 11.5	402.8 ± 4.0 ± 34.5
$\sigma_{tot}(pA \to \bar{K}^{*0}X)$ [mb]		
29.5 ± 0.2 ± 2.6	89.3 ± 1.6 ± 9.1	291.6 ± 3.5 ± 27.7

Table 6.6: Extrapolated total cross sections for K^{*0} and $\bar{K}^{*0}$ production in pA collisions at $\sqrt{s} = 41.6\,\text{GeV}$. The errors denote the statistical and systematic errors, respectively.

presented in table 3.2 on page 47, we see that both the K^{*0} and the $\bar{K}^{*0}$ production cross sections show a stronger increase with the atomic mass number than the total inelastic cross section. In case of the carbon target about 15 % (12 %) of all inelastic interactions contain a K^{*0} ($\bar{K}^{*0}$). For the tungsten target the ratios increase to 24 % and 18 %, respectively. The detailed analysis of atomic number dependencies is the subject of the following section.

6.3 Atomic mass number dependence

In the context of the Glauber model (cf. section 2.2) we have presented several predictions for the dependence of production cross sections on the atomic mass number of the target material, using the parameterization

$$\sigma^{pA} = \sigma^{pN} \cdot A^{\alpha}, \tag{6.7}$$

where α is a function of p_T^2 and y. In this section we will study these predictions on the differential and total K^{*0} and $\bar{K}^{*0}$ production cross sections.

6.3.1 Production cross sections

Before we investigate the A-dependence of the differential distributions we will determine the value of α for the integrated production cross sections. For the total cross sections this will additionally provide us with an estimation of the K^{*0} and $\bar{K}^{*0}$ production cross sections in proton-nucleon collisions at $\sqrt{s} = 41.6\,\text{GeV}$, which we will compare to other measurements in pp collisions.

Fig. 6.6 shows the integrated K^{*0} and K^{*0} production cross sections in $2.6 \leq y \leq 4.5$

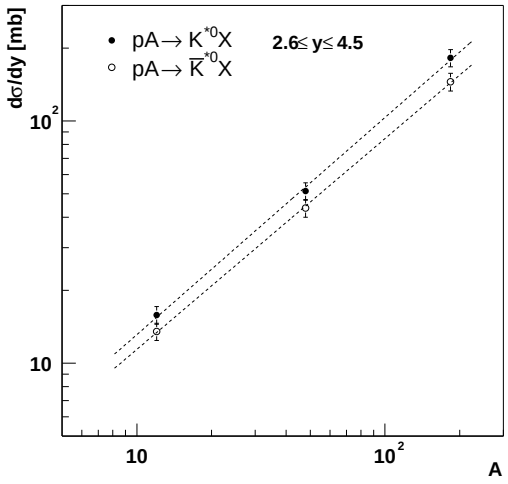

Figure 6.6: Atomic number dependence of the production cross sections in $2.6 \leq y \leq 4.5$. The parameterization by (6.7) is shown separately for K^{*0} and $\bar{K}^{*0}$.

plotted as a function of the atomic mass number of the respective target materials used. Separately for K^{*0} and $\bar{K}^{*0}$ the data are fit to the power-law ansatz (6.7). The results for α and the production cross sections in proton-nucleus collisions, $\sigma^{pN}_{K^{*0}}$ and $\sigma^{pN}_{\bar{K}^{*0}}$, are summarized in table 6.7. Comparing α to the result obtained for the inelastic cross section (see section 3.6 on page 45) we see that both the K^{*0} and $\bar{K}^{*0}$ production cross sections show a stronger A-dependence than the inelastic cross section. While the latter roughly scales with the surface of the nucleus, the K^{*0} production cross sections show a tendency towards scaling with the volume of the nucleus. With α being about 0.88 there is, however, still some nuclear shadowing seen. In the next section we will investigate in which way the shadowing depends on the kinematic variables p_T^2 and y.

The results of A^α-fits of the total production cross sections for the K^{*0} and the $\bar{K}^{*0}$

Δy	α	σ^{pN} [mb]	σ^{pN}_{tot} [mb]	χ^2/n.d.f.
		$pA \to K^{*0}X$		
[2.6; 4.5]	0.90 ± 0.04	1.67 ± 0.30		0.37
total	0.89 ± 0.05		3.79 ± 0.71	0.01
		$pA \to \bar{K}^{*0}X$		
[2.6; 4.5]	0.87 ± 0.04	1.54 ± 0.27		0.08
total	0.84 ± 0.05		3.61 ± 0.70	0.19

Table 6.7: Atomic number dependence of the K^{*0} and $\bar{K}^{*0}$ production cross sections at mid-rapidity and of the total production cross sections. The values are the results of fits of the cross sections to the parameterization (6.7).

yield another set of α values which are compatible with the results obtained at mid-rapidity (see table 6.7). Additionally, they provide an estimate of the total production cross sections $\sigma^{pN}_{K^{*0},tot}$ and $\sigma^{pN}_{\bar{K}^{*0},tot}$ in proton-nucleon interactions.

Fig. 6.7 shows a comparison of the estimated total production cross sections $\sigma^{pN}_{K^{*0},tot}$

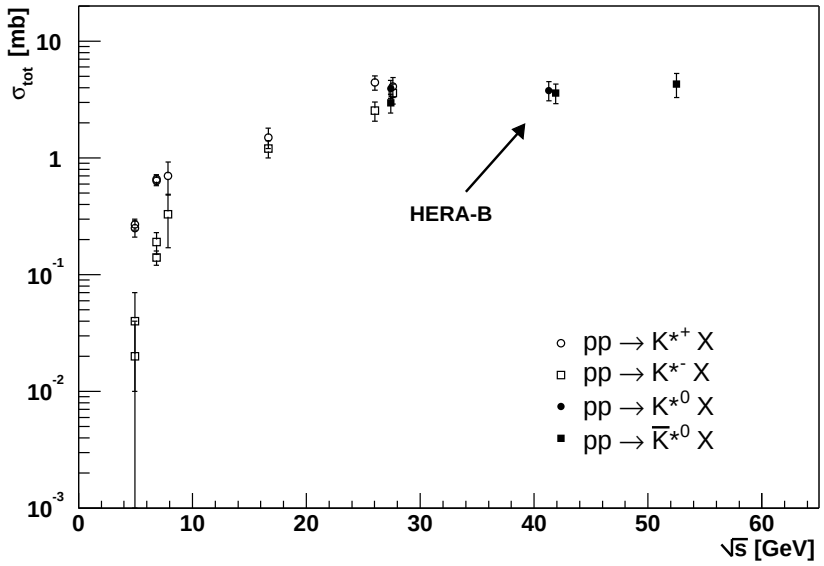

Figure 6.7: Comparison of K^* production cross sections at various center-of-mass energies [blo74, boc79, kic79, dri81, bri82, azi86, bog88, agu91]. The results of this analysis have been slightly displaced from each other for better visibility.

and $\sigma^{pN}_{\bar{K}^{*0},tot}$ with the results of measurements in proton-proton interactions (see also section 1.3.2). Our results are in perfect agreement with previous measurements at $\sqrt{s} = 27\,\text{GeV}$ and $\sqrt{s} = 52.5\,\text{GeV}$. From this we conclude that the extrapolation of the cross sections to $A = 1$ by means of the parameterization (6.7) is a reasonable ansatz.

6.3.2 Differential cross sections

This analysis is the first one which investigates the atomic number dependence of K^{*0} and $\bar{K}^{*0}$ production as a function of the kinematic variables. Fig. 6.8 presents the dependence of the parameter α on the transverse momentum squared, the values being extracted from fits of the differential p_T^2 distributions to (6.7). For both K^{*0} and $\bar{K}^{*0}$ α does clearly increase with p_T^2. Above $p_T^2 = 4\,\text{GeV}^2$ α exceeds one. Even within the large errors of the measurement we see a clear Cronin effect in K^{*0} and $\bar{K}^{*0}$ production. The effect is not reflected by the Monte-Carlo generator FRITIOF, which predicts $\alpha(p_T) \approx$ const., as is indicated in fig. 6.8.

Compared to its first observation in kaon and pion production (cf. fig. 2.6 on page 23) the size of the Cronin effect for K^{*0} and $\bar{K}^{*0}$ production is of the same order, and in both cases the onset of the effect is seen at $p_T \approx 2\,\text{GeV}$. Unfortunately, nothing can be said about a possibly different A-dependence of particle and anti-particle cross sections as observed in [cro77] for kaon production above $p_T = 4\,\text{GeV}$.

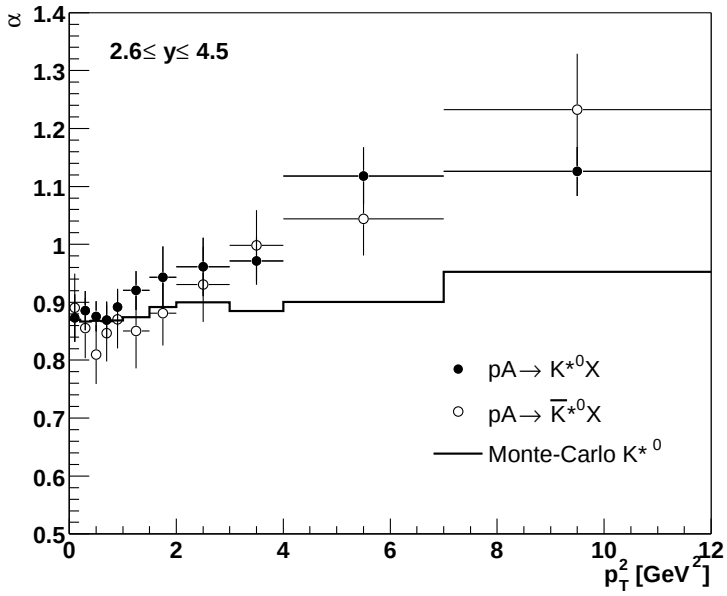

Figure 6.8: Atomic number dependence of the differential production cross sections as a function of p_T^2.

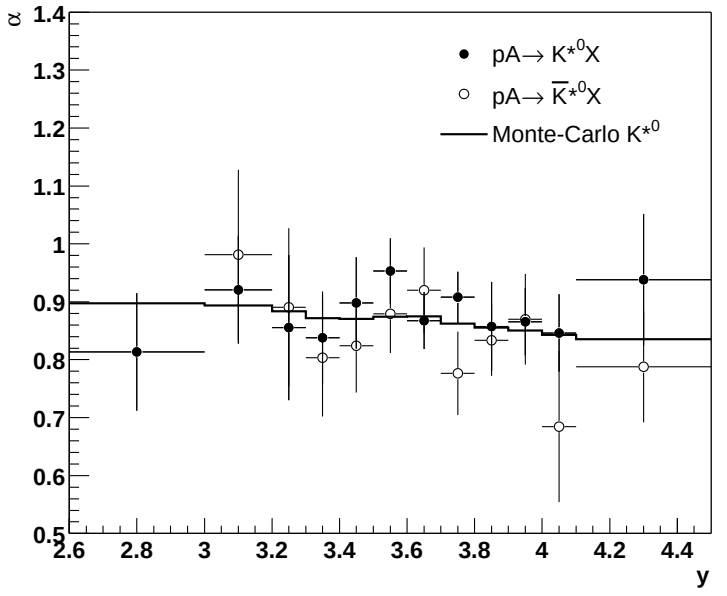

Figure 6.9: Atomic number dependence of the differential production cross sections as a function of rapidity.

What concerns the dependence of α on the rapidity the data are in good agreement with the Monte-Carlo expectations (shown in fig. 6.9). As predicted within the framework of the Glauber model, $\alpha(y) \approx$ const. at mid-rapidity.

The values on α obtained from the various fits performed on the differential cross sections in p_T^2 and y are summarized in appendix B.

Chapter 7

Summary and outlook

We have presented a comprehensive analysis of K^{*0} and $\bar{K}^{*0}$ vector meson production in proton-nucleus collisions. The measurement has been performed with the HERA-B detector operated at the HERA proton storage ring, where the protons have been brought to collision with fixed nuclear targets of C, Ti, and W at a center-of-mass energy of $\sqrt{s} = 41.6\,\mathrm{GeV}$.

The measurement has been carried out at mid-rapidity in the range of $2.6 \leq y \leq 4.5$ ($-1.2 \leq y^* \leq 0.7$ in the center-of-mass system). In transverse momentum a range of $0 \leq p_T^2 \leq 12\,\mathrm{GeV}^2$ has been investigated. We have presented the differential and total cross sections for K^{*0} and $\bar{K}^{*0}$ production and studied their dependence on the atomic mass number A of the target material. The results have been compared to existing measurements and to the predictions of the Monte-Carlo generator FRITIOF.

The K^{*0} and $\bar{K}^{*0}$ have been reconstructed focusing on their decay into charged $K\pi$ pairs, where the signal yield is obtained by fits to the $K\pi$ invariant mass distribution. In total 900.000 $K^{*0} \to K^+\pi^-$ and $\bar{K}^{*0} \to K^-\pi^+$ decays have been reconstructed from about 130 million of inelastic events analyzed. Since the measurement suffers from high combinatoric background, a detailed study of the impact of the background parameterization on the signal yield has been performed. In many kinematic bins it has been found to be the dominating systematic uncertainty of the measurement.

In studying the transverse differential distributions of K^{*0} and $\bar{K}^{*0}$ production we have found that the Monte-Carlo simulation drastically underestimates the data in the region of high transverse momenta. To allow a correct acceptance calculation the Monte-Carlo distributions have been reweighted as to fit the data. We have shown that in doing so an observed shift in the rapidity distributions between Monte-Carlo and data is corrected, too.

We have motivated that strange resonance production is an important tool to probe the existence of the quark-gluon plasma in relativistic heavy-ion collisions. Due to their short life times these resonances are in particular useful to estimate the critical energy density of the plasma and to understand the processes which play a role in its cool-down phase. In order to interpret the effects seen in AA collisions data on strange resonance production in pA collisions are needed as

a normalization. This does not only concern absolute production cross section measurements but especially the atomic number dependence of the cross sections as a function of the kinematic variables y and p_T^2. This analysis is the first presenting such a detailed study on the K^{*0} and $\bar{K}^{*0}$ resonances.

The measured differential cross sections of K^{*0} and $\bar{K}^{*0}$ production have been compared to the predictions of the Monte-Carlo generator FRITIOF. Excellent agreement has been found both for the absolute cross sections and for the shape of the differential distributions as a function of rapidity.

The differential distributions in p_T^2 have been fit by two different phenomenological ansatzes. A power-law parameterization which is derived from predictions in the framework of hard parton-parton scattering fits the data in the full kinematic range. In comparing the mean p_T of the fits we find similar results for K^{*0} and $\bar{K}^{*0}$ production.

The total production cross sections $\sigma^{pA}_{K^{*0},tot}$ have been derived by extrapolating the differential cross sections to full phase space using the Monte-Carlo simulation. By fitting them to $\sigma^{pA}_{K^{*0},tot} = \sigma^{pN}_{K^{*0},tot} A^{\alpha}$ we have obtained estimates for the respective proton-nucleon cross sections which perfectly fit the data from previous measurements of K^* production in pp collisions. Within the acceptance of our measurement the parameter α has been measured as being $\alpha(K^{*0}) = 0.90 \pm 0.04$ and $\alpha(\bar{K}^{*0}) = 0.87 \pm 0.04$ for the K^{*0} and the $\bar{K}^{*0}$, respectively.

In our analysis of the atomic mass number dependence of the cross sections we have also investigated the dependence of α on the kinematics. As a function of rapidity $\alpha(y)$ is flat for both K^{*0} and $\bar{K}^{*0}$, as is expected from model calculations within the framework of the Glauber model. As a function of transverse momentum, however, $\alpha(p_T^2)$ increases strongly with p_T^2. For $p_T^2 > 4\,\mathrm{GeV}^2$ $\alpha > 1$ is seen both for K^{*0} and $\bar{K}^{*0}$, i.e. for the first time the Cronin effect is observed in K^{*0} resonance production. The size of the effect is comparable to what has originally been observed in charged kaon production. The Monte-Carlo generator FRITIOF is not able to describe the effect but predicts a flat $\alpha(p_T^2)$.

All measurements are dominated by systematic uncertainties. For the integrated differential cross sections the systematic error is of the order of 8-11 %, the largest uncertainty being on the kaon identification efficiency. Additionally, substantial uncertainties arise from the limited Monte-Carlo statistics and the luminosity determination.

If a proper description of the combinatorial background by event mixing techniques could be achieved, many additional studies on K^{*0} production will be possible, as e.g. the investigation of systematic shifts in the resonance mass peak position or deviations of the signal form from the Breit-Wigner shape due to rescattering of the K^{*0} daughter particles in nuclear matter. A comparison of these effects with the results obtained in heavy-ion collisions will further help to understand the properties of the quark-gluon plasma.

This work has been supported by the Bundesministerium für Bildung und Forschung, FRG, under contract number 05HB1PEA/7.

Appendix A

Redesign of the HERA-B Target Control System

This appendix deals with the redesign of the HERA-B Target Control System TaCoS. The requirements on the system are shortly introduced, before the considerations which led to the redesign of the software are discussed. After an overview of the system's implementation the changes with respect to former versions are documented.

A.1 Motivation

The basic requirements on the HERA-B target have already been introduced in section 3.3.1. The decision to build a wire target which surrounds the proton beam in two stations of four wires each is a consequence of these requirements. The wire target solution itself imposes, however, additional demands on the system which concern mainly the wire steering:

- The interaction rate must be kept constant.
- In case of multi-wire operation the interaction rate should be equally shared among the operated wires.
- A safe wire insertion and retraction procedure is needed.
- A protection against unintentionally high rates must be provided.
- In case of a system failure the operated wires must be automatically retracted from the beam.

The Target Control System (TaCoS) [iss01] integrates all parts of the target operation into a common framework. It provides a steering algorithm which keeps the interaction rate constant and equalizes the interaction rate among the operated wires, an easy to handle and safe wire insertion and retraction procedure, and several safety protocols for emergency handling. Furthermore, it measures the interaction rate and the rate produced on the individual wires and cares about the logging of all target related values to database. Finally, it distributes wire

positions and interaction rate to the HERA-B trigger system and provides an easy to use graphical user interface and status display.

Even if the rate stabilization and equalization is the most prominent task of TaCoS, the safety features of the system are most important to guarantee a smooth operation. Its redesign became necessary mainly due to the fact that from time to time instabilities in the system were observed resulting mostly in unpredictable wire movements. Additionally, the system was not completely faultless with respect to mis-operation by unexperienced users.

In this overview we will restrict ourselves to changes in the steering code of the Target Control System. Many other small changes have been performed which we do not have the space to discuss in detail:

- The data taking and database logging has been restructured. To save disk space different levels of logging have been introduced, reducing during non-operation the amount of data written to database.
- An interlink to the HERA-B trigger system has been created to provide the trigger in real time with target related quantities such as the current interaction rate and the wire positions.
- The graphical user interface has been extended to provide not only absolute wire positions but also the distance of the wires to the beam core (in units of beam-σ). Additionally, several new buttons have been introduced to allow a more convenient insertion and retraction of several wires at the same time.

A.2 TaCoS overview and structure

In this section we will give a brief overview of the Target Control System. For a more in-depth introduction the reader is kindly referred to [iss01]. For an introduction to the target mechanics see [fun03]. A detailed description of the interaction rate measurement can be found in [spr00].

The target control system is physically divided into three levels. A programmable hardware controller drives the stepping motors of the individual targets. The information on which target to move is provided by the process target, running on a PowerPC processor under the real time operating system LynxOS. Interactions by the user are usually realized via the graphical user interface TCC (Target Control Center), running on a Linux PC in the HERA-B control room. The graphical user interface is connected to the target process via ethernet, the connection between the target process and the controller is realized by a serial link.

The physical separation of the three components already ensures a high level of safety. In case the user interface is not working the target process keeps the system operational. In case target fails or its connection to the hardware controller is interrupted, the controller automatically retracts all targets to their end-switches. Since the controller is connected to emergency power, this is even possible in case of a global electricity cut-off.

In the following we will briefly summarize the duties and features of the three components.

A.2.1 Graphical user interface

The graphical user interface TCC (see fig. A.1) provides a high-level communication between the target system and its users. It displays all important quantities of the target operation like the interaction rate, the operated wires, and the background rates as a function of time for the last 30 minutes. The user is able to select and deselect wires, to choose the desired interaction rate, and to adjust steering parameters like emergency thresholds. The user commands are sent to the steering program target which then takes appropriate measures. For the safety concept of the system it is important that the user is only able to express his final goal (e.g. "put another wire to the beam") rather than the way this goal is achieved (i.e. "possibly retract other wires first, find the beam with the newly selected wire, put all wires to the beam again"). This task is handled by the steering program.

A.2.2 Steering program

The program target plays a decisive role in the Target Control System. It is the actual heart of the system, taking decisions regarding the steering of the targets and translates them into proper commands executable by the hardware controller. During normal operation a steering automatics keeps the interaction rate constant and distributes the rate equally among the operated wires. In case of unintentionally high rates proper emergency actions are taken.

target is responsible for collecting and logging the data needed for a stable target operation. This includes the readout of hodoscope and charge integrator rates for the determination of the interaction rate and the individual wire rates, and the readout of the hardware controller to obtain the current wire positions and the status of the endswitches. Furthermore, it evaluates user commands coming from the graphical user interface, and takes appropriate actions.

A.2.3 Hardware controller

The hardware controller is directly connected to the stepping motors of the targets. Being the last part of the electronics chain of the Target Control System, it operates completely independent of the other components. The controller is fully programmable and able to run complex commands. When it is e.g. asked by target to move a wire a certain distance, it is able to fulfil this task without further intervention of target. A program running on the hardware controller permanently checks that the connection to target is still alive. This so-called watchdog completely retracts all targets from the beam if it is not able to communicate with target for more than 1.5 s.

Beneath the serial connection to target the controller comprises eight hardware inputs. One of the controller inputs is connected to the so-called emergency-out

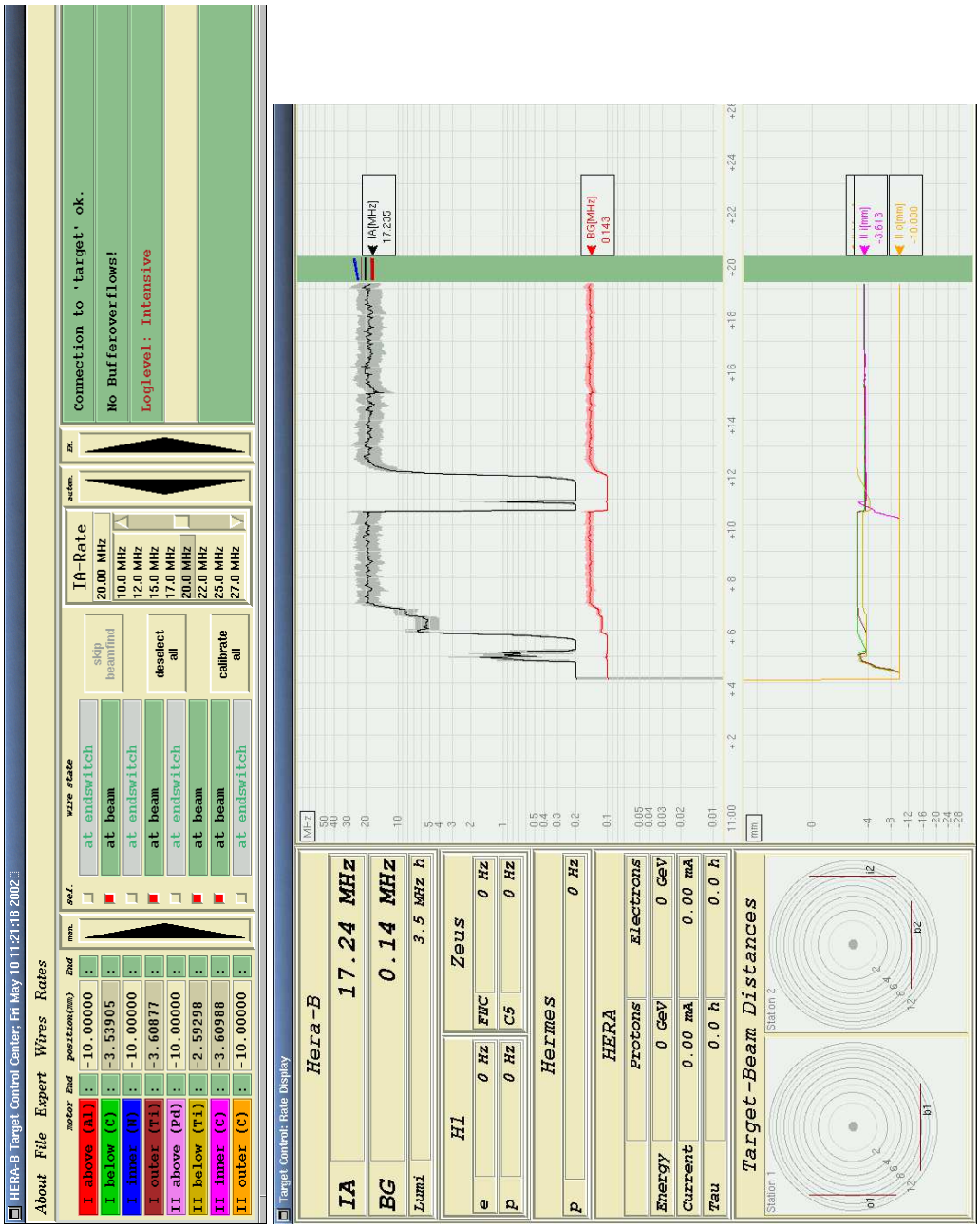

Figure A.1: The Target Control Center (TCC). The user controls are placed on the top window. In the middle part of the upper window the individual targets are selected and the desired interaction rate is chosen. In our example, four targets are at the beam, the desired interaction rate is 20 MHz. The bottom part of TCC displays on the left side the current interaction and background rates (also those of the other HERA experiments). On the bottom-left the distances of the wires to the beam center (in units of beam-σ) are shown. The big display on the right side of the window shows the chronologic development of the rates and wire positions for the last 30 minutes.

button located in the HERA-B control room. If this button is pressed, a program running on the controller automatically retracts all targets from the beam. The other controller inputs are connected to the inner and outer end-switches of the target mechanics[1].

While the graphical user interface has no direct influence on the safety of the target operation, a proper functioning of the hardware controller and the steering program are essential. While the hardware controller and its programs have proven to operate reliably, the steering program showed from time to time problems in wire handling. Most of these problems could be attributed to a constantly evolving steering code. At some point a new implementation of this sensitive part of the program became necessary.

A.3 Redesign of the state machine

The steering program is the most complicated among all components of the Target Control System. The reason for this is its quite complex scope of duties which is not only the steering of the targets but also data taking of target related quantities and their logging to database. Despite of its complexity the program must provide a fast and flexible reaction on its input parameters, especially in emergency situations if e.g. the interaction rate is unintentionally large.

To provide the maximum possible availability target is subdivided into several self-sufficient modules, as is shown in fig. A.2. Virtually each module is managed by its own thread[2]. The only pool for an exchange of information between the modules is a common data buffer. Short accesses to read information from or write data to the buffer are handled by means of so-called mutexes[3]. The data buffer is organized as a ring buffer, i.e. it is rotated, keeping data history of up to 3 minutes. Since data logging is not a time-critical task, only data from the end of the buffer are written to disk (cf. fig. A.2). In this way the time-consuming logging is decoupled from the more time-critical parts of the program.

The heart of the new implementation of target is the state machine. It provides safe transitions of the system from one stable state into another stable state. State transitions are mostly requested by the user via the graphical user interface. If e.g. the user selects a certain wire, the state machine initiates a state transition for this wire, in this case from st_at_endswitch or st_at_inpos to st_at_beam (for the complete list of states, see table A.1). Based on information about the states of the other wires the state machine decides which intermediate steps (so-called transitional states) must be taken to safely arrive at the requested stable state. The full procedure is completely transparent to the user who simply has to wait until the stable state is reached. After each state machine turn, the automatics module is called which keeps the interaction rate constant using all wires which

[1] the end-switches are implemented to mechanically constrain the path length of the individual targets. Additionally, the outer end-switches define the parking position of each target (see [fun03]).

[2] a thread is an individual process running within the context of a program.

[3] a mutex is a method provided by the operating system to allow a process to exclusively access a certain resource.

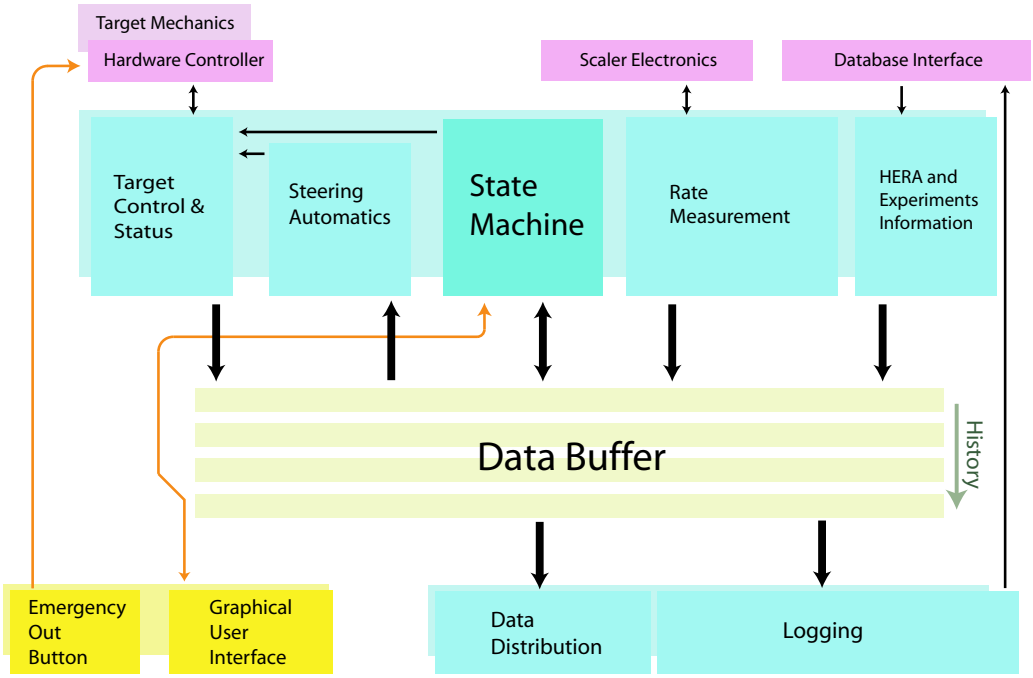

Figure A.2: Simplified sketch of the steering program target. The different modules (in blue) read (write) information from (to) a common data buffer. User interfaces are drawn in yellow.

are in the state st_at_beam.

Preceding versions of target did also use a state machine. The differences to the current version are, however, substantial:

- State machine and automatics were strongly coupled and implemented in a single, rather long routine. In the current implementation, both state machine and automatics are encapsulated into separate modules and called one after the other.
- Old versions of the state machine performed state-wise transitions of (groups of) wires. The new state machine handles transitions separately for each wire, which provides a rather transparent code which is easily extendable.
- There was no distinction between stable and transitional states. Furthermore, some transitional states were used for more than one task (the state moving a wire to its ini-position e.g. did not distinguish between wires coming from the outer end-switch moving towards the beam and wires coming from the beam which are retracted). In the current implementation of the state machine each transitional state has exactly one succeeding state only.

To disentangle the state machine from the automatics module, large parts of the software have been rewritten. In doing so its basic functionality has been preserved, i.e. the behavior of the old setup is emulated by the new state machine.

This was an important prerequisite to make an instant data taking with the new setup possible.

Under the surface, however, the code has been substantially changed. As a result a code has been developed, which is slim and easy to maintain. Furthermore, it is essentially free of bugs simply because it is easy to read.

The new version of the Target Control System went online after the HERA upgrade and has been stably operated ever since, the data of the December 2002 running used in this analysis also having been taken with this setup.

state (stable)	duty	
st_at_endswitch	Wire is at endswitch.	
st_at_inipos	Wire is at ini-position.	
st_at_beam	Wire is at beam and controlled by the automatics module.	
st_at_fixed	Wire is fixed and can be moved manually. It is not controlled by the automatics module.	
state (transitional)	**duty**	**transition to**
st_emergency	Rate emergency. Wire is retracted by 20 μm	st_emergency_wait
st_oaemergency	OverAll-Emergency. Wire is retracted by 200 μm.	st_oaemergency_wait
st_rlemergency	RateLoss-Emergency. Wire is de-selected.	st_mop_prepare
st_oaemergency_wait	Wait 5 turns and recover the pre-emergency state. For wires in beam find, change to st_all_to_beam.	pre-emergency state
st_emergency_wait	Wait 5 turns and recover pre-emergency state.	pre-emergency state
st_mop_prepare	Wait until the wire stopped moving.	st_mopping
st_mopping	Move wire to end-switch.	st_at_endswitch
st_iniposing	Move wire to ini-position.	st_iniposing_stopped
st_iniposing_stopped	Wait until wire is at ini-position.	st_at_inipos
st_all_to_beam	Move all newly selected wire to the beam until the interaction rate is above the beam-found threshold.	st_all_touched_prepare
st_all_touched_prepare	Measure the interaction rate after the beam has been touched.	st_all_touched
st_all_touched	A single wire is in st_single_to_beam. Wait until it found the beam.	st_single_to_beam
st_single_to_beam	Move the wire to the beam until the interaction rate exceeds twice the rate measured in st_all_touched_prepare.	st_single_touched
st_single_touched	Resume beam-finding for all wires in st_all_touched.	st_wait
st_wait_prepare	Retract the wire by 1 mm to allow the other wires in st_all_touched to continue beam-find.	st_wait
st_wait	Wait for all other wires to finish single beam find.	st_at_beam

Table A.1: Summary table of all states used in the current implementation of the target state machine. A series of state transitions always ends in a stable state.

Appendix B

Summary of cross sections

$pC \rightarrow K^{*0}X$			
Δp_T^2 [GeV^2]	$d\sigma/dp_T^2$ [mb/GeV^2]	$N_{K^{*0}}$	acc. [%]
0.0-0.2	27.9 ± 1.7	29699 ± 862 ± 686	3.26 ± 0.13
0.2-0.4	16.0 ± 1.1	25170 ± 839 ± 1288	4.52 ± 0.26
0.4-0.6	9.7 ± 0.4	20107 ± 614 ± 424	5.49 ± 0.39
0.6-0.8	6.1 ± 0.3	15768 ± 594 ± 32	7.08 ± 0.59
0.8-1.0	4.8 ± 0.3	14677 ± 531 ± 689	8.88 ± 0.88
1.0-1.5	2.9 ± 0.1	27632 ± 667 ± 1223	13.60 ± 1.06
1.5-2.0	1.3 ± 0.1	16184 ± 512 ± 1204	17.07 ± 1.75
2.0-3.0	0.54 ± 0.05	17545 ± 501 ± 1490	20.00 ± 2.19
3.0-4.0	0.20 ± 0.01	8145 ± 313 ± 446	25.56 ± 5.30
4.0-7.0	0.042 ± 0.005	7002 ± 263 ± 712	34.63 ± 5.19
7.0-12.0	0.0043 ± 0.0004	1478 ± 110 ± 57	33.62 ± 10.64
$pC \rightarrow \bar{K}^{*0}X$			
Δp_T^2 [GeV^2]	$d\sigma/dp_T^2$ [mb/GeV^2]	$N_{\bar{K}^{*0}}$	acc. [%]
0.0 0.2	24.6 ± 1.7	27416 ± 664 ± 76	3.35 ± 0.18
0.2 0.4	13.6 ± 0.8	21618 ± 624 ± 293	4.82 ± 0.28
0.4 0.6	8.2 ± 0.5	16783 ± 575 ± 666	5.50 ± 0.43
0.6 0.8	5.4 ± 0.3	13446 ± 520 ± 367	7.42 ± 0.73
0.8 1.0	3.9 ± 0.3	11431 ± 469 ± 573	9.33 ± 1.22
1.0 1.5	2.4 ± 0.1	22562 ± 611 ± 1067	12.22 ± 1.45
1.5 2.0	1.08 ± 0.07	12791 ± 460 ± 675	15.14 ± 2.36
2.0 3.0	0.39 ± 0.03	11979 ± 441 ± 771	19.38 ± 4.73
3.0 4.0	0.12 ± 0.01	4943 ± 268 ± 339	22.74 ± 6.92
4.0 7.0	0.026 ± 0.002	4241 ± 228 ± 269	29.68 ± 9.24
7.0 12.0	0.0022 ± 0.0003	800 ± 111 ± 42	-

Table B.1: Inclusive differential cross sections of K^{*0} production in proton-nucleus collisions at mid-rapidity. The numbers are given in the accessible rapidity range $2.6 \leq y \leq 4.5$. For the cross sections the total error is given. For the signal yields the first number represents the statististical error and the second number is the systematic error σ_{bg}.

$pTi \rightarrow K^{*0}X$			
Δp_T^2 [GeV^2]	$d\sigma/dp_T^2$ [mb/GeV^2]	$N_{K^{*0}}$	acc. [%]
0.0-0.2	86.3 ± 9.0	11837 ± 510 ± 475	3.12 ± 0.24
0.2-0.4	52.6 ± 3.9	10995 ± 495 ± 90	4.59 ± 0.34
0.4-0.6	32.8 ± 2.3	9165 ± 425 ± 300	6.06 ± 0.59
0.6-0.8	19.4 ± 1.4	6748 ± 393 ± 160	7.25 ± 0.91
0.8-1.0	13.9 ± 1.0	5784 ± 358 ± 143	9.11 ± 1.38
1.0-1.5	9.5 ± 1.0	12533 ± 480 ± 1195	12.74 ± 2.064
1.5-2.0	4.7 ± 0.3	8009 ± 409 ± 286	16.11 ± 2.80
2.0-3.0	2.00 ± 0.17	9041 ± 362 ± 669	19.67 ± 3.35
3.0-4.0	0.641 ± 0.044	3730 ± 233 ± 93	23.61 ± 6.09
4.0-7.0	0.155 ± 0.012	3672 ± 199 ± 204	49.62 ± 8.30
7.0-12.0	0.019 ± 0.002	923 ± 84 ± 10	28.62 ± 15.70
$pTi \rightarrow \bar{K}^{*0}X$			
Δp_T^2 [GeV^2]	$d\sigma/dp_T^2$ [mb/GeV^2]	$N_{\bar{K}^{*0}}$	acc. [%]
0.0-0.2	73.8 ± 8.0	10374 ± 511 ± 442	3.11 ± 0.23
0.2-0.4	45.9 ± 4.0	9282 ± 435 ± 193	4.74 ± 0.40
0.4-0.6	26.0 ± 3.0	6882 ± 406 ± 425	5.46 ± 0.66
0.6-0.8	18.7 ± 1.4	6093 ± 373 ± 139	6.56 ± 1.07
0.8-1.0	14.9 ± 1.4	5782 ± 450 ± 276	8.84 ± 1.55
1.0-1.5	7.9 ± 0.6	9731 ± 462 ± 487	12.37 ± 1.82
1.5-2.0	3.94 ± 0.36	6397 ± 345 ± 461	16.53 ± 3.58
2.0-3.0	1.22 ± 0.12	5386 ± 330 ± 419	13.41 ± 4.76
3.0-4.0	0.45 ± 0.08	2688 ± 204 ± 413	29.93 ± 9.72
4.0-7.0	0.083 ± 0.009	2225 ± 176 ± 154	48.95 ± 11.98
7.0-12.0	0.007 ± 0.001	544 ± 94 ± 22	54.62 ± 27.29

Table B.2: Inclusive differential cross sections of K^{*0} production in proton-titanium collisions at mid-rapidity. The numbers are given in the accessible rapidity range $2.6 \leq y \leq 4.5$. For the cross sections the total error is given. For the signal yields the first number represents the statististical error and the second number is the systematic error σ_{bg}.

$pW \rightarrow K^{*0}X$			
Δp_T^2 [GeV^2]	$d\sigma/dp_T^2$ [mb/GeV^2]	$N_{K^{*0}}$	acc. [%]
0.0-0.2	308.0 ± 28.8	36285 ± 1388 ± 2059	2.71 ± 0.16
0.2-0.4	179.0 ± 10.7	32124 ± 1172 ± 730	4.31 ± 0.25
0.4-0.6	105.5 ± 5.9	25367 ± 1165 ± 12	5.90 ± 0.45
0.6-0.8	67.2 ± 5.2	20127 ± 788 ± 1257	6.66 ± 0.62
0.8-1.0	54.0 ± 2.8	19286 ± 795 ± 429	7.76 ± 0.86
1.0-1.5	35.6 ± 2.6	40479 ± 1075 ± 2671	10.86 ± 0.93
1.5-2.0	17.4 ± 2.2	25475 ± 739 ± 3095	14.11 ± 2.25
2.0-3.0	7.44 ± 0.76	28515 ± 730 ± 2800	21.83 ± 3.53
3.0-4.0	2.82 ± 0.21	13737 ± 475 ± 900	17.91 ± 4.35
4.0-7.0	0.803 ± 0.050	15451 ± 428 ± 843	28.52 ± 4.86
7.0-12.0	0.093 ± 0.007	3382 ± 178 ± 167	37.48 ± 10.15
$pW \rightarrow \bar{K}^{*0}X$			
Δp_T^2 [GeV^2]	$d\sigma/dp_T^2$ [mb/GeV^2]	$N_{\bar{K}^{*0}}$	acc. [%]
0.0-0.2	280.8 ± 22.0	31610 ± 910 ± 570	2.64 ± 0.16
0.2-0.4	140.4 ± 10.8	25623 ± 895 ± 1334	4.19 ± 0.28
0.4-0.6	74.7 ± 4.6	18698 ± 804 ± 536	6.23 ± 0.52
0.6-0.8	54.0 ± 3.3	17090 ± 708 ± 651	5.92 ± 1.01
0.8-1.0	41.8 ± 2.6	15889 ± 793 ± 512	9.90 ± 1.15
1.0-1.5	24.9 ± 3.4	30292 ± 854 ± 4054	10.53 ± 1.35
1.5-2.0	11.8 ± 1.1	18623 ± 668 ± 1585	16.85 ± 2.55
2.0-3.0	5.0 ± 0.5	20389 ± 655 ± 1894	20.16 ± 3.32
3.0-4.0	1.9 ± 0.2	9712 ± 416 ± 696	16.52 ± 6.30
4.0-7.0	0.44 ± 0.03	8509 ± 367 ± 376	35.40 ± 7.73
7.0-12.0	0.057 ± 0.005	1759 ± 153 ± 48	27.43 ± 11.10

Table B.3: Inclusive differential cross sections of K^{*0} production in proton-tungsten collisions at mid-rapidity. The numbers are given in the accessible rapidity range $2.6 \leq y \leq 4.5$. For the cross sections the total error is given. For the signal yields the first number represents the statistical error and the second number is the systematic error σ_{bg}.

$pC \to K^{*0}X$			
Δy	$d\sigma/dy$ [mb]	$N_{K^{*0}}$	acc. [%]
2.6-3.0	8.12 ± 1.72	4981 ± 281 ± 334	0.91 ± 0.18
3.0-3.2	9.61 ± 1.62	13230 ± 534 ± 1295	4.10 ± 0.54
3.2-3.3	9.66 ± 1.68	10392 ± 415 ± 1051	6.40 ± 0.87
3.3-3.4	8.79 ± 1.41	15283 ± 504 ± 1938	10.35 ± 0.96
3.4-3.5	9.05 ± 1.12	20019 ± 550 ± 1488	13.17 ± 1.26
3.5-3.6	8.71 ± 0.82	22022 ± 596 ± 777	15.05 ± 1.25
3.6-3.7	8.26 ± 0.78	22255 ± 599 ± 644	16.05 ± 1.37
3.7-3.8	7.60 ± 0.60	21607 ± 588 ± 352	16.93 ± 1.24
3.8-3.9	9.19 ± 1.01	20548 ± 693 ± 539	13.31 ± 1.35
3.9-4.0	8.68 ± 0.86	16455 ± 498 ± 348	11.28 ± 1.03
4.0-4.1	7.80 ± 0.87	10885 ± 424 ± 340	8.31 ± 0.83
4.1-4.5	6.62 ± 1.89	10067 ± 432 ± 2667	2.26 ± 0.22
$pC \to \bar{K}^{*0}X$			
Δy	$d\sigma/dy$ [mb]	$N_{\bar{K}^{*0}}$	acc. [%]
2.6-3.0	–	2261 ± 192 ± 80	-
3.0-3.2	6.31 ± 1.55	9078 ± 500 ± 1188	4.28 ± 0.86
3.2-3.3	8.43 ± 2.46	8367 ± 379 ± 1455	5.91 ± 1.36
3.3-3.4	8.04 ± 1.60	11829 ± 459 ± 1664	8.76 ± 1.19
3.4-3.5	7.83 ± 1.14	14795 ± 520 ± 779	11.25 ± 1.47
3.5-3.6	7.52 ± 0.78	17547 ± 559 ± 221	13.89 ± 1.35
3.6-3.7	6.87 ± 0.79	17790 ± 572 ± 1136	15.43 ± 1.40
3.7-3.8	7.89 ± 0.86	18491 ± 577 ± 671	13.95 ± 1.37
3.8-3.9	6.87 ± 0.66	17425 ± 560 ± 65	15.11 ± 1.37
3.9-4.0	6.82 ± 0.85	13605 ± 478 ± 991	11.88 ± 1.12
4.0-4.1	8.31 ± 1.39	9739 ± 595 ± 125	6.98 ± 1.08
4.1-4.5	9.26 ± 1.67	11362 ± 558 ± 1148	1.83 ± 0.26

Table B.4: Inclusive differential cross sections of K^{*0} production in proton-carbon collisions. For the cross sections the total error is given. For the signal yields the first number represents the statistical error and the second number is the systematic error σ_{bg}.

$pTi \rightarrow K^{*0}X$			
Δy	$d\sigma/dy$ [mb]	$N_{K^{*0}}$	acc. [%]
2.6-3.0	28.0 ± 9.5	1849 ± 164 ± 158	0.73 ± 0.23
3.0-3.2	32.9 ± 6.7	5632 ± 310 ± 173	3.80 ± 0.74
3.2-3.3	25.2 ± 5.1	5414 ± 308 ± 649	9.58 ± 1.45
3.3-3.4	34.1 ± 7.2	6468 ± 355 ± 426	8.45 ± 1.62
3.4-3.5	24.5 ± 3.9	9033 ± 397 ± 508	16.42 ± 2.35
3.5-3.6	28.1 ± 4.0	9567 ± 422 ± 699	15.17 ± 1.74
3.6-3.7	25.8 ± 3.3	9510 ± 429 ± 210	16.42 ± 1.96
3.7-3.8	27.9 ± 3.6	9771 ± 430 ± 133	15.56 ± 1.88
3.8-3.9	24.3 ± 3.2	8449 ± 394 ± 229	15.49 ± 1.87
3.9-4.0	29.1 ± 3.9	7509 ± 360 ± 186	11.49 ± 1.40
4.0-4.1	43.3 ± 9.4	5569 ± 387 ± 227	5.72 ± 1.15
4.1-4.5	27.6 ± 4.3	5364 ± 381 ± 53	2.16 ± 0.30
$pTi \rightarrow \bar{K}^{*0}X$			
Δy	$d\sigma/dy$ [mb]	$N_{\bar{K}^{*0}}$	acc. [%]
2.6-3.0	17.8 ± 7.5	1083 ± 150 ± 120	0.68 ± 0.26
3.0-3.2	25.7 ± 6.6	4681 ± 338 ± 541	4.05 ± 0.88
3.2-3.3	38.5 ± 15.0	4037 ± 274 ± 714	4.66 ± 1.59
3.3-3.4	27.1 ± 7.1	5604 ± 332 ± 865	9.2 − ±1.85
3.4-3.5	22.1 ± 5.3	6386 ± 379 ± 438	12.88 ± 2.84
3.5-3.6	23.0 ± 3.3	8041 ± 408 ± 73	15.59 ± 2.11
3.6-3.7	24.8 ± 5.2	8504 ± 538 ± 998	15.27 ± 2.44
3.7-3.8	21.7 ± 4.4	7904 ± 501 ± 766	16.23 ± 2.74
3.8-3.9	20.3 ± 3.2	6976 ± 384 ± 432	15.30 ± 2.07
3.9-4.0	16.9 ± 2.8	5069 ± 335 ± 184	13.34 ± 2.00
4.0-4.1	17.5 ± 2.7	4140 ± 283 ± 88	10.54 ± 1.44
4.1-4.5	25.1 ± 6.5	4506 ± 372 ± 717	2.00 ± 0.37

Table B.5: Inclusive differential cross sections of K^{*0} production in proton-titanium collisions. For the cross sections the total error is given. For the signal yields the first number represents the statistical error and the second number is the systematic error σ_{bg}.

$pW \to K^{*0}X$			
Δy	$d\sigma/dy$ [mb]	$N_{K^{*0}}$	acc. [%]
2.6-3.0	74.9 ± 13.8	6877 ± 342 ± 5	1.07 ± 0.19
3.0-3.2	118.9 ± 17.2	20042 ± 697 ± 2183	3.94 ± 0.55
3.2-3.3	108.4 ± 17.4	17968 ± 791 ± 2969	7.75 ± 1.20
3.3-3.4	86.3 ± 8.8	21357 ± 757 ± 2581	11.56 ± 1.10
3.4-3.5	108.1 ± 13.2	26675 ± 781 ± 1740	11.53 ± 1.36
3.5-3.6	118.9 ± 12.5	30142 ± 824 ± 359	11.84 ± 1.20
3.6-3.7	88.1 ± 7.0	31096 ± 826 ± 969	16.50 ± 1.24
3.7-3.8	90.3 ± 7.3	30765 ± 819 ± 808	15.92 ± 1.22
3.8-3.9	102.0 ± 13.8	28216 ± 792 ± 1257	12.93 ± 1.71
3.9-4.0	92.0 ± 10.4	22449 ± 789 ± 913	11.40 ± 1.23
4.0-4.1	76.2 ± 10.9	15150 ± 563 ± 954	9.29 ± 1.29
4.1-4.5	88.9 ± 12.2	12482 ± 577 ± 1662	1.64 ± 0.21
$pW \to \bar{K}^{*0}X$			
Δy	$d\sigma/dy$ [mb]	$N_{\bar{K}^{*0}}$	acc. [%]
2.6-3.0	58.2 ± 15.00	5051 ± 425 ± 175	1.01 ± 0.24
3.0-3.2	90.7 ± 30.7	13895 ± 783 ± 1690	3.58 ± 1.11
3.2-3.3	96.5 ± 25.1	12855 ± 555 ± 2218	6.23 ± 1.19
3.3-3.4	72.0 ± 14.2	14749 ± 657 ± 1964	9.57 ± 1.33
3.4-3.5	74.4 ± 11.2	22133 ± 983 ± 2137	13.90 ± 1.47
3.5-3.6	84.4 ± 11.6	23557 ± 782 ± 1332	13.04 ± 1.57
3.6-3.7	84.3 ± 13.6	23722 ± 783 ± 2479	13.15 ± 1.55
3.7-3.8	66.2 ± 10.2	21289 ± 761 ± 2294	15.03 ± 1.55
3.8-3.9	67.3 ± 8.4	20817 ± 711 ± 1440	14.45 ± 1.42
3.9-4.0	73.7 ± 9.6	17040 ± 635 ± 27	10.80 ± 1.32
4.0-4.1	60.9 ± 14.4	13428 ± 780 ± 2324	10.40 ± 1.53
4.1-4.5	68.1 ± 19.7	13422 ± 497 ± 3362	2.30 ± 0.32

Table B.6: Inclusive differential cross sections of K^{*0} production in proton-tungsten collisions. For the cross sections the total error is given. For the signal yields the first number represents the statistical error and the second number is the systematic error σ_{bg}.

$pA \to K^{*0}X$			
Δp_T^2 [GeV^2]	α	$d\sigma/dp_T^2$ [mb/GeV^2/nucl.]	χ^2/n.d.f.
0.0-0.2	0.87 ± 0.04	3.15 ± 0.46	0.58
0.2-0.4	0.89 ± 0.03	1.75 ± 0.25	0.13
0.4-0.6	0.88 ± 0.03	1.10 ± 0.11	0.02
0.6-0.8	0.87 ± 0.03	0.70 ± 0.08	0.56
0.8-1.0	0.89 ± 0.03	0.50 ± 0.07	4.14
1.0-1.5	0.92 ± 0.03	0.29 ± 0.04	0.54
1.5-2.0	0.94 ± 0.05	0.124 ± 0.025	0.13
2.0-3.0	0.96 ± 0.05	0.049 ± 0.010	0.03
3.0-4.0	0.97 ± 0.04	0.017 ± 0.003	3.90
4.0-7.0	1.12 ± 0.05	0.0023 ± 0.0005	3.48
7.0-12.0	1.13 ± 0.04	0.00026 ± 0.00004	0.71
$pA \to \bar{K}^{*0}X$			
Δp_T^2 [GeV^2]	α	$d\sigma/dp_T^2$ [mb/GeV^2/nucl.]	χ^2/n.d.f.
0.0-0.2	0.89 ± 0.04	2.62 ± 0.41	1.35
0.2-0.4	0.86 ± 0.03	1.63 ± 0.21	0.11
0.4-0.6	0.81 ± 0.03	1.10 ± 0.14	0.11
0.6-0.8	0.85 ± 0.03	0.66 ± 0.08	0.75
0.8-1.0	0.87 ± 0.03	0.46 ± 0.06	1.57
1.0-1.5	0.85 ± 0.05	0.29 ± 0.05	0.01
1.5-2.0	0.88 ± 0.04	0.122 ± 0.018	0.55
2.0-3.0	0.93 ± 0.05	0.037 ± 0.007	1.49
3.0-4.0	1.00 ± 0.05	0.010 ± 0.002	0.22
4.0-7.0	1.05 ± 0.04	0.0017 ± 0.0003	6.04
7.0-12.0	1.24 ± 0.08	0.00008 ± 0.00003	6.59

Table B.7: Atomic number dependence of the differential production cross sections as a function of p_T^2.

$pA \to K^{*0}X$			
Δy	α	$d\sigma/dy$ [mb/nucl.]	χ^2/n.d.f.
2.6-3.0	0.81 ± 0.10	1.09 ± 0.46	0.09
3.0-3.2	0.92 ± 0.08	0.96 ± 0.33	0.04
3.2-3.3	0.89 ± 0.10	0.96 ± 0.39	1.47
3.3-3.4	0.83 ± 0.07	1.16 ± 0.35	0.64
3.4-3.5	0.91 ± 0.07	0.87 ± 0.25	2.34
3.5-3.6	0.95 ± 0.05	0.79 ± 0.17	1.03
3.6-3.7	0.87 ± 0.05	0.94 ± 0.18	0.19
3.7-3.8	0.91 ± 0.04	0.80 ± 0.13	0.11
3.8-3.9	0.86 ± 0.07	1.00 ± 0.28	2.65
3.9-4.0	0.87 ± 0.05	1.01 ± 0.22	0.01
4.0-4.1	0.84 ± 0.06	0.99 ± 0.24	3.70
4.1-4.5	0.93 ± 0.10	0.71 ± 0.31	0.26
$pA \to \bar{K}^{*0}X$			
Δy	α	$d\sigma/dy$ [mb/nucl.]	χ^2/n.d.f.
2.6-3.0	-	-	-
3.0-3.2	0.98 ± 0.15	0.56 ± 0.31	0.03
3.2-3.3	0.89 ± 0.14	0.96 ± 0.55	0.35
3.3-3.4	0.80 ± 0.10	1.12 ± 0.45	0.12
3.4-3.5	0.82 ± 0.08	0.99 ± 0.31	0.17
3.5-3.6	0.88 ± 0.07	0.83 ± 0.20	0.44
3.6-3.7	0.92 ± 0.07	0.70 ± 0.18	0.01
3.7-3.8	0.78 ± 0.07	1.14 ± 0.29	0.09
3.8-3.9	0.83 ± 0.06	0.85 ± 0.19	0.18
3.9-4.0	0.87 ± 0.08	0.72 ± 0.21	2.84
4.0-4.1	0.68 ± 0.13	1.39 ± 0.66	1.54
4.1-4.5	0.73 ± 0.12	1.50 ± 0.66	0.01

Table B.8: Atomic number dependence of the differential production cross sections as a function of rapidity.

Appendix C

List of used runs

run	target	ia rate	date	start + end time	no. of events	$\mathcal{L}_{ia}$ [mb^{-1}]	$\mathcal{L}_{rnd}$ [mb^{-1}]
20653	b1	1.36	2002/12/09	06:46 - 07:22	1732592	7971.2	84.6
20663	b1	0.55	2002/12/12	09:35 - 11:07	4003997	17065.4	68.3
20668	b1	0.56	2002/12/12	12:02 - 13:00	2288926	9695.1	46.4
20669	b1	0.57	2002/12/12	13:09 - 13:22	418950	1788.7	7.5
20670	b1	0.68	2002/12/12	13:31 - 14:21	2580816	11264.2	43.2
20671	i1	0.93	2002/12/12	14:27 - 15:21	2625666	1577.1	6.2
20675	i1	1.28	2002/12/12	22:18 - 00:45	7730931	4763.0	23.8
20676	b1	0.82	2002/12/13	00:54 - 01:08	675437	2973.9	15.1
20677	b1	0.90	2002/12/13	01:17 - 02:38	4568646	20366.5	101.3
20678	b1	0.88	2002/12/13	02:46 - 04:16	5121506	22801.7	113.1
20679	i1	1.27	2002/12/13	04:21 - 06:59	8675028	5358.3	24.2
20680	i1	1.32	2002/12/13	07:07 - 07:32	1374786	847.7	3.9
20682	b2	0.96	2002/12/13	07:50 - 09:31	5497520	8926.2	40.4
20693	b2	0.98	2002/12/15	03:27 - 03:44	573379	905.8	7.2
20695	b2	0.99	2002/12/15	03:55 - 05:30	4722483	7566.3	48.8
20705	b1	0.79	2002/12/15	12:17 - 12:54	1213497	5741.4	26.3
20706	b1	0.78	2002/12/15	13:03 - 13:05	36267	164.8	1.2
20723	b1	0.92	2002/12/17	10:55 - 11:54	2845949	12655.6	81.8
20724	b1	0.96	2002/12/17	12:16 - 12:29	247948	1223.3	10.3
20725	b1	0.96	2002/12/17	12:53 - 14:31	3147911	13742.4	131.0
20728	b1	0.78	2002/12/17	17:03 - 17:19	451704	1885.5	21.7
20734	b1	0.78	2002/12/17	17:33 - 19:57	7433569	32527.7	175.2
20735	i1	0.80	2002/12/18	06:49 - 07:29	1043289	604.0	3.4
20738	i1	1.27	2002/12/18	08:30 - 09:11	2080780	1280.5	6.6
20739	i1	1.20	2002/12/18	09:53 - 12:11	7003330	4271.8	24.0
20740	b1	0.74	2002/12/18	12:23 - 13:59	3786598	16460.5	86.0
20742	b1	0.73	2002/12/18	14:35 - 15:31	2714468	11797.8	61.7
20743	b1	0.75	2002/12/18	15:49 - 17:00	3641525	15852.9	86.6
20744	i1	1.18	2002/12/18	17:08 - 17:23	362345	218.3	1.4
20746	i1	1.23	2002/12/18	17:33 - 19:12	5002784	3054.1	16.7
20747	i1	1.26	2002/12/19	00:17 - 02:20	6219769	3834.0	17.7
20749	i1	1.24	2002/12/19	02:51 - 04:06	3897458	2391.0	12.2
20764	i1	0.86	2002/12/20	06:24 - 07:59	4183931	2460.3	12.7
20766	i1	0.98	2002/12/20	08:51 - 09:50	2309124	1393.0	9.1
20767	i1	1.16	2002/12/20	09:57 - 10:02	136246	81.4	0.7
20768	b1	0.89	2002/12/21	02:04 - 03:07	2435408	10663.7	79.0
20769	b1	0.89	2002/12/21	03:23 - 03:51	236485	1039.1	7.2
20770	b1	0.89	2002/12/21	03:58 - 06:31	7865311	34472.1	253.0
20771	b2	1.09	2002/12/21	08:25 - 08:25	2707408	4417.8	24.2
20772	b2	1.09	2002/12/21	08:37 - 09:13	1677012	2718.4	16.9
20773	b2	1.10	2002/12/21	09:33 - 11:22	5654007	9201.0	54.6

Bibliography

[abt97] I. Abt *et al.* (The H1 collaboration), Nucl. Instr. Meth. **A 386** (1997) 310.

[abt02] I. Abt *et al.*, Phys. Lett. **B 561** (2002) 61.

[abt03] I. Abt *et al.*, Eur. Phys. J. **C 26** (2003) 345.

[abt03$^+$] I. Abt *et al.*, Eur. Phys. J. **C 29** (2003), 181.

[abt04] I. Abt *et al.*, *Luminosity measurement in HERA-B*, to be published in Nucl. Instr. Meth.

[agu91] M. Aguilar-Benitez *et al.*, Z. Phys. **C 50** (1991) 405.

[ale99] T. Alexopoulus *et al.*, Phys. Rev. Lett. **82** (1999) 41.

[alp73] B. Alper *et al.*, Phys. Lett. **B 44** (1973) 521.

[alt77] G. Altarelli and G. Parisi, Nucl. Phys. **B 126** (1977) 298.

[are01] A. Arefiev *et al.*, IEEE Trans. Nucl. Sci. **48** (2001) 1059.

[ari04] I. Ariño *et al.*, Nucl. Instr. Meth. **A 516** (2004) 445.

[art74] X. Artru, G. Menessier, Nucl. Phys. **B 70** (1974) 93.

[aus04] V. Aushev *et al.*, *The HERA-B Luminosity Page*, http://www-hera-b.desy.de/subgroup/detector/target/Luminosity.html

[azi86] T. Aziz *et al.*, Z. Phys. **C 30** (1986) 381.

[bab98] The BaBar collaboration, *The BaBar Physics Book*, SLAC-R-504.

[bag02] Y. Bagaturia *et al.*, Nucl. Instr. Meth. **A 490** (2002) 223.

[ban73] M. Banner *et al.*, Phys. Lett. **B 44** (1973) 537.

[bas02] J. Bastos, J. Carvalho, and M. Schmelling, *A statistical method for monitoring the luminosity of HERA-B data*, HERA-B internal note 02-039 (2002).

[bel93] A. Belogianni *et al.*, Z. Phys. **C 59** (1993) 35.

[bel94] The Belle Collaboration, *Technical Design Report*, KEK-Report 94-2.

[ber71] S.M. Berman, J.D. Bjorken, and J.B. Kugut, Phys. Rev. **D4** (1971) 3388.

[bia82] A. Bialas, Proc. Mult. Part. Dyn., Volendam (1982) 328.

[bjo69] J.D. Bjorken and E.A. Paschos, Phys. Rev. Lett. **185** (1969) 1975.

[bjo69$^+$] J.D. Bjorken, Phys. Rev. **179** (1969) 1547.

[ble02] M. Bleicher and J. Aichelin, Phys. Lett. **B 530** (2002) 81.

[blo74] V. Blobel *et al.*, Phys. Lett. **B 48** (1974) 73.

[boc79] K. Bockmann *et al.* Nucl. Phys. **B 166** (1979) 284.

[bog88] M.Y. Bogolyubsky *et al.*, IFVE-89-5 (1988).

[bon98] R. Bonciani *et al.*, Nucl. Phys. **B 529** (1998) 424.

[bön02] Marc-Oliver Bönig, *Bau und Inbetriebnahme von Szintillationszählern zur Luminositätsbestimmung am HERA-B Experiment*, diploma thesis, Dortmund (2002).

[brä01] M. Bräuer, *Alignment des HERA-B Vertexdetektors*, PhD thesis, Heidelberg (2001).

[bre89] A. Breakstone *et al.*, Z. Phys. **C 43** (1989) 185.

[bri82] D. Brick *et al.*, Phys. Rev. **D 25** (1982) 2248.

[bru02] M. Bruinsma, *J/ψ in pA - Performance of the First Level Trigger of HERA-B and Nuclear Effects in J/ψ Production*, PhD thesis, University of Utrecht (2002).

[buc01] M.W. Buchler, *Measurement of J/ψ differential cross sections in 920 GeV/c proton-nucleus collisions using the muon channel*, PhD thesis, Detroit (2001).

[büs73] F.W. Büsser *et al.*, Phys. Lett. **B 46** (1973) 471.

[cap91] A. Capella, Nucl. Phys. **A 525** (1991), 133c.

[car03] J. Carvalho, Nucl. Phys. **A 725** (2003) 269.

[cel78] W. Celmaster *et al.*, Phys. Rev. **D 17** (1978) 876.

[con02] P. Conde Muiño, *Measurement of the ratio between the D^+ and the D^0 production cross section using an impact parameter method*, PhD thesis, Santiago de Compostela (2002).

[con03] P. Conde Muiño, *DQ tests and new results*, Minimum Bias Analysis Meeting, Hamburg (2003/07/15).

[cro75] J.W. Cronin *et al.*, Phys. Rev. **D 11** (1975) 3105.

[cro77] J.W. Cronin *et al.*, Phys. Rev. Lett. **38** (1977) 670.

[dam03] M. Dam *et al.*, *The Second Level Trigger Algorithm*, HERA-B internal note 03-021 (2003).

[dri81] D. Drijard *et al.*, Z. Phys. **C 9** (1981) 293.

[dür95] M. Düren, *The HERMES experiment: From the Design to the First Results*, DESY HERMES **95-02**, 1995.

[ego04] V. Egorytchev *et al.*, *Analysis note for* $D^0 \to \mu^+\mu^-$ *study*, HERA-B internal note 04-001 (2004).

[fac04] P. Faccini, *Resonance Production – Recent Results*, Proceedings of Quark Matter 2004, to be published in J. Phys. **G** (2004).

[faw90] H. Fawcett *et al.*, Z. Phys. **C 46** (1990) 513.

[fun03] M. Funcke, *Strahlphysikalische Aspekte des Targetbetriebs bei HERA-B*, PhD thesis, Dortmund (2003).

[gea94] *GEANT Detector Description and Simulation Tool*, CERN Program Library Long Writeup W5013, CERN (1993).

[gei90] W.M. Geist *et al.*, Phys. Rep. **197** (1990) 263.

[gel64] M. Gell-Mann, Phys. Lett. **8** (1964) 214.

[gle00] T. Glebe, *Vt++ Version 1.0*, HERA-B internal note 00-175 (2000).

[göt82] R. Göttgens *et al.*, Z. Phys. **C 12** (1982), 323.

[gra78] P. Granet *et al.*, Nucl. Phys. **B 140** (1978) 389.

[hag65] R. Hagedorn, Suppl. Nuov. Cim. **3** (1965) 147.

[hag02] K. Hagiwara *et al.*, Phys. Rev. **D 66** 010001 (2002).

[her00] The HERA-B collaboration, *HERA-B physics in 2001/2002*, Letter to the DESY directorate (2000).

[her01] J.M. Hernandez, Proc. CHEP '01 (2001) 545.

[hoh01] M. Hohlmann, Nucl. Instr. Meth. **A 461** (2001) 21.

[hul02] W. Hulsbergen, *A Study of Track Reconstruction and Massive Dielectron Production in HERA-B*, PhD thesis, Amsterdam (2002).

[hwa04] R.C. Hwa and C.B. Yang, nucl-th/0403001.

[iss01] S. İşsever, *Entwicklung des Target-Steuersystems für das HERA-B-Experiment und Untersuchung der Eigenschaften des Targetbetriebs am HERA-Speicherring*, PhD thesis, Dortmund (2001).

[jan77] G. Jancso *et al.*, Nucl. Phys. **B 124** (1977) 1.

[jan95] D.M. Jansen *et al.*, Phys. Rev. Lett. **74** (1995) 3118.

[jac64] J.D. Jackson *et al.*, Nuov. Cim. **34** (1964) 1644.

[kic79] H. Kichimi *et al.*, Lett. Nuov. Cim. **24** (1979) 129.

[kid01] N. Kidonakis *et al.*, Phys. Rev. **D 64** (2001) 114001.

[kni00] C. Knierim (C. van Eldik), *Messung und Analyse von Ratenfluktuationen am HERA-B-Target*, diploma thesis, Dortmund (2000).

[knö03] K. T. Knöpfle *et al.*, Nucl. Instr. Meth. **A 501** (2003) 39.

[knö04] K. T. Knöpfle *et al.*, submitted to J. Phys. G: Nucl. Phys. - Proc. Quark Matter 2004.

[koc86] P. Koch *et al.*, Phys. Rep. **142** (1986) 169.

[kop02] B.Z. Kopeliovich *et al.*, Phys. Rev. Lett. **88** (2002) 232303.

[krz78] A. Krzywicki, Proc. Ecole d'ete de physique des particules **23** (1978).

[lin92] A. Lindner, *Messung der* $K^*(892)$*-,* $\rho^0(770)$*-,* $\omega(783)$*- und* $f_0(975)$*-Produktion in Ereignissen der* e^+e^-*-Annihilation bei Energien im Bereich der* Υ*-Resonanzen*, PhD thesis, Dortmund (1992).

[loh94] T. Lohse *et. al.*, *HERA-B: An Experiment to Study CP Violation in the B System Using an Internal Target at the HERA Proton Ring (Proposal)*, DESY PRC **94-02** (1994).

[loh95] T. Lohse, *Vertex Reconstruction and Fitting*, HERA-B internal note 95-013 (1995).

[mar02] C. Markert *et al.*, Proc. PASI, Campos do Jordao (2002) 533.

[med03] M. Medinnis, *Reprocessing Tests*, http://www-hera-b.desy.de/general/minutes/herab/weekly/reprodif.html

[nör03] M. Nörenberg, *Tracking Efficiency of the HERA-B First Level Trigger in the Single Lepton Mode*, PhD thesis, Hamburg (2003).

[pan68] W.K.H. Panofsky, Proc. 14th Int. Conf. High Energy Physics, Wien (1968) 23.

[pes01] R. Pestotnik, *Identification of Pion, Kaons, and Protons in the HERA-B Spectrometer*, PhD thesis, Ljubljana (2001).

[pi92] H. Pi, Comp. Phys. Comm. **71** (1992) 173.

[ple02] M.A. Pleier, *Measurement of the* $\Lambda/\bar{\Lambda}$ *hyperon polarization in proton nucleus collisions at 920 GeV proton beam energy*, PhD thesis, Heidelberg (2002).

[raf82] J. Rafelski and B. Mueller, Phys. Rev. Lett. **48** (1982) 1066.

[sat00] H. Satz, Rep. Prog. Phys. **63** (2000) 1511.

[sch01] B. Schwenninger, *Das Myon-Pretrigger-System für das HERA-B Experiment*, PhD thesis, Dortmund (2001).

[sjö94] T. Sjöstrand, Comp. Phys. Comm. **82** (1994) 74.

[som03] A. Somov, private communication (2003).

[spr00] S. Spratte, *Bestimmung der Wechselwirkungsrate des HERA-B Targets und Untersuchung des Coasting Beam am HERA Protonen-Ring*, PhD thesis, Dortmund (2000).

[sta04] M. Starič, private communication (2004).

[sym04] M. Symalla, *Produktion von ϕ-Mesonen in inelastischen Proton-Kern-Wechselwirkungen bei 41.6 GeV Schwerpunktsenergie*, PhD thesis, Dortmund (2004).

[vas99] Y. Vassiliev *et al.*, *Multi-Target Operation at the HERA-B Experiment*, STORI99 conference proceedings (1999) 512.

[vos94] G.A. Voss and B.H. Wiik, Ann. Rev. Nucl. Part. Sci. **44** (1994) 413.

[wal02] R. Waldi, *Flavour Oscillation and CP Violation of B mesons*, in: M. Beyer (Ed.), *CP Violation in Particle, Nuclear and Astrophysics*, Lecture Notes in Physics, Springer (2002).

[wan91] X.N. Wang and M. Gyulassy, Phys. Rev. **D 44** (1991) 3501.

[win75] F.C. Winkelmann *et al.*, Phys. Lett. **56 B** (1975) 101.

[zav03] M. Zavertiaev, *Data Quality Monitoring*, Minimum Bias Analysis Meeting, Hamburg (2003/03/13).

[zeu93] The ZEUS collaboration, *The ZEUS detector, Status Report*, DESY-PRC 93-05 (1993).

[zie98] M. Ziegler, *Untersuchung von Detektortypen für das innere Spurkammersystem des HERA-B Experiments*, Diploma thesis, Heidelberg (1998).

[zoc00] A. Zoccoli, Nucl. Instr. Meth. **A 446** (2000) 246.

[zwe64] G. Zweig, CERN reports **TH-401**, **TH-402** (1964).

Danke!

21.30 Uhr am Dienstag vor Ostern. Es ist vollbracht. Nichts geht mehr.

Es ist leer im Vogel an der Ecke Eulenstraße/Große Brunnenstraße. In einer halben Stunde erst kommen die Kollegen. Genug Zeit, um ein paar Worte des Dankes zu Papier zu bringen. Knut steht hinterm Tresen. Wie jeden Dienstag. Unaufgefordert bringt er die lang ersehnte revitalisierende Hopfenkaltschale. Hefeweizen, dunkel. Danke, Knut.

Marc-Olli und Olaf sitzen schon am Tisch, wohl um dem feierlichen Akt beizuwohnen. Woher sie es wussten? Ich denke, der Chef hat nicht dicht gehalten. Danke, Chef.

Wann die Tradition der dienstäglichen Treffen im "Wohnzimmer" ihren Anfang nahm, weiß keiner der Beteiligten der ersten Stunde mehr genau. Aber anfangs waren ja auch nur zwei Personen beteiligt. Und denen fiel das Vergessen noch nie schwer. Die zwei: Mitch und ich. Mitch mit der Elvis-Tolle. Das waren noch Zeiten.

22.00 Uhr. Knut bringt gerade mein zweites Weizen, da kommt Mitch zur Tür herein. In all den Jahren, die wir zusammen in einem gemeinsamen Büro unser Dasein fristen, haben wir uns gut gehalten. Ich habe mittlerweile erste graue Haare, und Mitchs Elvis-Tolle ist kleiner geworden.

Mit Mitch habe ich schon viel Spaß gehabt. Ein schnelles Bier im Lütt Döns am Feierabend. Mitbürger im REAL beobachten. Studien der Kryptoanalyse. Das tägliche Hoffen auf Probleme beim Debian-Upgrade. Reste von dem üblen Whiskylikör, den wir eines späten Abends auf seinem Balkon geleert haben, stehen übrigens immer noch bei mir herum. Und bald schon stehen wieder zahllose Abende an der Elbe vor der Tür.

Der Sommer ist eine brotlose Zeit für Knut, weil seine Stammkundschaft am Elbstrand grillt. Würstchen statt Tortellini. Astra statt Franziskaner. Eine Truppe von tollen Leuten, in der die Dortmunder immer vorne dabei sind. Andrea, Christoph und Olaf, Marc-Olli und Mitch, manchmal auch HC, Ana oder der Commander. Martin und Mino nicht zu vergessen. Und demnächst auch Jesko, Jörg, Andreas, Klaus, Stefan und Dirk? Und wenn wir nicht grillen, dann nur, weil Vatertag ist. Oder weil wir unser Bier zusammen mit Matthias im Labor von Dr. Honigtau-Bunsenbrenner in Dortmund trinken, weil mal wieder ein Doktorwagen ansteht.

Über die Jahre habe ich schon zahlreiche Weizen im Vogel getrunken. Aber kaum jemals so entspannt wie heute. Dass diese Arbeit nun in einer lesbaren Form vorliegt, ist in erster Linie meinen Korrekturlesern zu verdanken, die sich bereitwillig und selbstlos in halbfertige Kapitel vertieft und das Unterste zu oberst gekehrt haben: Martins große "No!", mit denen er absolut unverständliche Passagen der Arbeit kommentierte, werden mir in ständiger Erinnerung bleiben. Achim blieb in den letzten Tagen oftmals länger als ich im Büro, um zahllose Seiten der Arbeit mit seiner Handschrift zu verzieren. Schliesslich HC, der mit großem persönlichen Engagement trotz des beständigen Termindrucks dem Text die Ecken und Kanten nahm.

Christoph und EMBL-Oli sind eingetroffen. Knut hat eine neue Aushilfe. Sie weiß noch nicht, wer welches Bier trinkt. Wir wetten schon mal, welchen Studiengang sie belegt. Illustration, sagt Knut. Wir haben alle falsch gelegen.

Dass ich überhaupt im Vogel sitze, verdanke ich in wesentlichen Teilen meinem Chef, Prof. Dietrich Wegener, den es, trotz vieler Androhungen, noch immer nicht ins "Wohnzimmer" verschlagen hat. Für die Möglichkeit, am spannenden Hamburger Leben teilhaben zu können, bedanke ich mich herzlich. Die Arbeit hier vor Ort hat mich viele wertvolle Erfahrungen sammeln lassen. Unter anderem die, dass es von immensem Vorteil ist vor Ort zu sein.
Prof. Michael Schmelling danke ich für die spontane Bereitschaft, das Zweitgutachten dieser Arbeit zu über- und die lange Reise von Heidelberg nach Dortmund auf sich zu nehmen.

Meinen Familien im fernen Hagen und in Erlangen danke ich für die rückhaltlose Unterstützung in den letzten Jahren. Die Tage mit Euch (häufig verbunden mit geradezu unanständiger Gewichtszunahme!) gehören immer wieder zu den schönsten des Jahres.

Ein weiteres großes Dankeschön gilt Ette, eM, Mr. Danili und dem Man von Q-art. In den letzten Monaten war es nicht immer leicht, alle Termine unter einen Hut zu bringen. Eure Flexibilität hat mir sehr geholfen.

All denjenigen, die ich nicht erwähnt habe, sei ein Bier für meine Vergeßlichkeit versprochen. Euch allen danke ich für die gute Zusammenarbeit während der letzten Jahre.

Mein allerletzter und größter Dank gilt Maria, für die Höhen und Tiefen, die wir gemeinsam erlebt haben, für Deine Geduld und Dein Lachen. Wir sollten heiraten!